THE CONTROL OF SOLIDIFICATION IN METAL CLADDING

A

THESIS

presented

for the Degree of

DOCTOR OF PHILOSOPHY

IN THE

UNIVERSITY OF LONDON

BY

MARTIN GORDON BROOKS

---o---

John Percy Research Group in
Process Metallurgy,
Department of Metallurgy,
The Royal School of Mines,
Imperial College,
LONDON, S.W.7.

A B S T R A C T

Composites of eutectic cast iron bonded to stainless steel, and eutectic tin lead bonded to lead were produced by the controlled solidification of liquid eutectic alloy.

Most of the experiments involved the immersion of a rotating cylindrical probe into the liquid metal. If the superheat was sufficient the initial chill layer remelted, exposing the probe surface, and after an interval for dissolution internal cooling air could be applied to cause further solidification.

A theoretical model, considering the solidification of a unique melting point alloy against a solid cooled at the remote surface, was used to investigate heat transfer during the preliminary stages of the bonding. The flow of heat at both the solid-liquid and dissimilar solid interfaces was described for a wide range of different parameters. The model predicted temperatures and solid thickness at different times, simulating growth and melt back of the chill layer in contact with the solid metal. The agreement with values measured experimentally was particularly good for the non ferrous system and reasonable for most of the high temperature work.

Comparisons are made with published work on concentric rotating cylinders. This included heat and mass transfer from the cylinders into aqueous and gaseous fluids. Of particular interest is work on mass transfer with metallic fluids, mostly dissolution of the inner rotating cylinder. Some liquid metal heat transfer with axial flow in the annular space is included. The advantage of concentric rotating cylinders for heat and mass transfer investigations is mentioned.

- - - - -

LIST OF CONTENTS

		Page No.
1.	INTRODUCTION	13
2.	A LITERATURE SURVEY	15
2.1	Industrial Clad Materials.	15
2.2	Solidification.	15
2.3	Cylindrical Solidification.	17
2.4	Physical Data.	17
2.4.1	Lead-Tin Alloy.	17
2.4.2	Ferrous.	20
2.5	Thermal Analysis.	20
2.6	Rotating Cylinders.	21
2.6.1	Fluid Flow.	21
2.6.2	Heat Transfer.	23
2.6.3	Mass Transfer.	23
2.7	Liquid Metal Heat Transfer.	25
2.8	Diffusion at an Interface.	26
3.	THEORETICAL MODEL.	28
3.1	Introduction.	28
3.2	Solid Metal Layer.	28
3.3	Mould or Probe Wall.	30
3.3.1	Semi Infinite Mode.	32
3.3.2	Finite Mode.	35
3.4	The Liquid Metal.	37
3.4.1	The Addition of Heat by Furnace Power.	38
3.5	Presolidification.	39
3.6	Computation.	40
4.	APPARATUS	44
4.1	The Double Sided Clad Ingot.	44
4.2	The Liquid Metal Furnaces.	44
4.2.1	Ferrous.	44
4.2.2	Tin-Lead	47
4.3	The Cylindrical Probes.	47

CONTENTS - contd./ Page No.

4.3.1	Stainless.	47
4.3.2	Lead	47
4.4	Rotation of the Cylinders	51
4.5	Ancillary Equipment.	56
5.	EXPERIMENTAL TECHNIQUE	59
5.1	Double Sided Ingot Cladding.	59
5.2	Ferrous Experiments.	59
5.2.1	Experimental Sequence.	59
5.2.2	Thermal Analysis.	61
5.2.3	Control of Temperature and Composition.	62
5.2.3.1	Eutectic Cast Iron.	62
5.2.3.2	3% Cast Iron.	63
5.2.3.3	1.4% Steel.	63
5.2.4	Experimental Measurement.	63
5.2.5	Preparation of Microstructures.	64
5.3	Lead Experiments.	65
5.3.1	Experimental Sequence.	65
5.3.2	Thermal Analysis	65
5.3.3	Experimental Measurement.	65
5.3.4	Preparation of Microstructures.	67
6.	R E S U L T S	68
6.1	Introduction to Presentation of Results.	68
6.2	Double Sided Ingot Cladding.	69
6.3	Immersion of Static Stainless Probes into Ferrous Alloys.	69
6.3.1	Chill Layer Growth, eutectic Cast Iron.	69
6.3.2	Chill Layer Growth and Melt Back.	69
6.3.2.1	Eutectic Cast Iron 50° Superheat.	76
6.3.2.2	Eutectic Cast Iron 90° Superheat.	76
6.3.2.3	3% Cast Iron.	82
6.3.2.4	1.4% Cast Iron.	82
6.3.3	Bonding Experiments.	86
6.3.3.1	Eutectic Cast Iron.	86
6.3.3.2	3% Cast Iron.	88

CONTENTS - contd./

		Page No.
6.4	Immersion of Rotating Probes into Lead Alloys.	88
6.4.1	Chill Layer Growth.	88
6.4.1.1	Lead Insert.	88
6.4.1.2	Stainless Probe.	95
6.4.2	Chill Layer Growth and Melt Back.	95
6.4.2.1	Lead Insert, 20° Superheat 68 r.p.m.	95
6.4.2.2	Lead Insert, 20° Superheat, 200 "	100
6.4.2.3	Lead Insert, 30° Superheat, 68 "	107
6.4.2.4	Stainless Probe.	107
6.4.3	Bonding Experiments Lead Insert.	107
6.5	Immersion of Rotating Stainless Probes into Ferrous Alloys.	113
6.5.1	Chill Layer Growth.	113
6.5.2	Chill Layer Growth and Melt Back.	113
6.5.2.1	Eutectic Cast Iron.	113
6.5.2.2	1.4% Steel.	119
6.5.3	Bonding Experiments.	119
6.5.3.1	Eutectic Cast Iron.	119
6.5.3.2	1.4% Steel.	119
7.	DISCUSSION	127
7.1	Introduction.	127
7.2	Double Sided Ingot Cladding.	127
7.3	Cylindrical Probe Experiments.	128
7.3.1	Chill Layer Growth.	128
7.3.2	Chill Layer Melt Back.	130
7.3.2.1	No Rotation.	130
7.3.2.2	With Rotation.	131
7.3.2.3	Liquid Metal Heat Transfer.	133
7.3.3	Dissolution or Melting of Substrate Surfaces.	138
7.3.4	Growth of Bonded Layers.	139
7.3.4.1	Eutectic Cast Iron.	141
7.3.4.2	Eutectic Tin-Lead.	143
7.4	The Structure of the Bonded Layers.	144
7.4.1	Ferrous.	144
7.4.2	Tin-Lead	146
7.5	Accuracy of Comparison between Theory & Experiment.	146

CONTENTS - contd./

		Page No.
7.5.1	Ferrous Heat Losses.	146
7.5.1.1	Conduction in the Stainless Probe.	147
7.5.1.2	From Melting Furnace.	147
7.5.2	Lead Heat Losses.	149
7.5.2.1	Conduction in the Probe.	150
7.5.2.2	From Melting Furnace.	150
7.5.3	The Accuracy of the Theory.	150
7.6	Errors of Measurement.	151
7.6.1	Temperature.	151
7.6.2	Rotation Speed.	152
7.6.3	Thickness.	152
7.6.4	Time.	153
8.	CONCLUSIONS.	155
9	FUTURE WORK	156

APPENDICES

1.	An attempt at measuring heat transfer coefficients directly.	158
2.	The effect of air cooling in the stainless steel probe.	160
3.	Correction for probe residence time with liquid metal displacement.	163
4.	Analysis of Materials used.	164
5.	Prevention of catastrophic melting during melt. back.	165
6.	Lead polishing.	167
7.	An empirical estimation of Nusselt numbers.	168
8.	Data used in computation.	171
	NOMENCLATURE.	173
	REFERENCES	177
	ACKNOWLEDGEMENTS	181

LIST OF FIGURES

		Page No.
1.	Temperature Vs Time : immersion of solid cylinders in molten cast iron.	18
2.	Chill layer thickness Vs Time.	19
3.	Diagram of Taylor Vortices in a fluid filling the annular space between rotating cylinders.	22
4.	Heat growth during growth of the chill layer.	29
5.	Heat transfer in Mould or Probe wall.	31
6.	Simplified Algorithm for computer programme.	42
7.	Dimensionless results Vs Dimensionless time for specimen computation.	43
8.	Preheat Furnace for Double-sided cladding of steel ingot.	45
9.	Diagram of Ferrous Melting Furnace.	46
10.	Diagram of Tin-Lead Melting Furnace.	48
11.	Section of Stainless steel probe.	49
12.	Equipment for Spot-welding thermocouples inside stainless steel probes.	50
13.	Plan view of cast lead insert, showing the four recesses which exactly matched the cage.	52
14.	Stainless steel cage without lead insert.	53
15.	Section of lead probe assembly.	54
16.	Section of rotating probe support with sliprings.	55
17.	A stainless steel probe suspended from the gantry over the ferrous furnace.	57
18.	Diagram of cooling air supply system.	58
19.	Arrangement of 'splash' tubes inside moulds.	60
20.	Undercooling during thermal analysis of eutectic tin-lead.	66

contd./

List of Figures - contd./ Page No.

21.	Bond strength shear test and results.	71
22.	Chromium and Nickel diffusion for two stainless clad steel specimens.	72
23.	Chromium and nickel diffusion for stainless clad specimen with nickel plating.	73
24.	Chill layer thickness Vs exposure time. Eutectic iron, zero superheat, stainless probe.	74
25.	Inside wall temperatures Vs Exposure time. Eutectic cast iron zero superheat, stainless probe.	75
26.	Chill layer thickness Vs exposure time. Eutectic cast iron 50°C superheat, stainless probe.	78
27.	Inside wall temperatures Vs exposure time. Eutectic cast iron, 50°C superheat, stainless probe.	79
28.	Chill layer thickness Vs exposure time - Eutectic cast iron, 90°C superheat, stainless probe.	81
29.	Inside wall temperature Vs Exposure time. Eutectic cast iron, 90°C superheat, stainless probe.	83
30.	A diagramatic section of eutectic cast iron shell.	84
31.	Temperatures Vs. time for eutectic cast iron bonding experiment.	89
32.	Microstructure of eutectic cast iron bonded to stainless steel without rotation.	90
33.	Chromium and Nickel diffusion for stainless clad cast iron, no probe rotation.	92
34.	Temperature Vs exposure time during attempted bonding of 3% cast iron.	94
35.	Chill layer thickness Vs exposure time. Eutectic Sn-Pb, zero superheat, Pb insert, 68 r.p.m.	96
36.	Inside and outside wall temperatures Vs, exposure time, Eutectic Sn-Pb, zero superheat, Pb insert 68 r.p.m.	97
37.	Chill layer thickness Vs exposure time. Eutectic Sn-Pb, zero superheat, stainless probe.	98

contd./

List of Figures - contd./ Page No.

38.	Chill layer thickness Vs exposure time - Eutectic Sn-Pb, 20°C superheat, Pb insert.	101
39.	Chill layer thickness Vs Exposure time - Eutectic Sn-Pb, 20°C superheat, Pb insert.	102
40.	Wall temperatures Vs exposure time. Eutectic Sn-Pb, 20°C superheat, Pb insert.	103
41.	Temperatures Vs exposure time, Eutectic Sn-Pb, 20°C superheat, Pb insert.	104
42.	Surface dissolution of two lead inserts.	106
43.	Chill layer Vs Exposure time. Eutectic Sn-Pb, 30°C superheat stainless probe.	109
44.	Temperatures Vs Exposure Time. Eutectic Sn-Pb on Pb insert bonding experiment, No. 1, Table 12.	111
45.	Temperature Vs Exposure Time. Eutectic Sn-Pb on Pb insert, bonding experiment No. 6, Table 12.	112
46.	Lead and tin diffusion for Eutectic Pb-Sn clad Pb.	114
47.	Chill layer thickness Vs exposure time. Eutectic cast iron, zero superheat, stainless probe rotating at 200 r.p.m.	115
48.	Inside wall temperatures Vs exposure time. Eutectic cast iron, zero superheat, stainless probe rotating at 200 r.p.m.	116
49.	Chill thickness Vs Exposure time. Eutectic cast iron, 90°C superheat stainless probe, rotating at 200 r.p.m.	117
50.	Temperature Vs time. Eutectic cast iron, 90°C superheat. Stainless probe rotating at 200 r.p.m.	118
51.	Stainless steel probes after immersion in 1.4% steel at about 90°C superheat.	121
52.	Chromium and nickel diffusion for stainless clad cast iron stainless probe rotating at 200 r.p.m.	122
53.	Microstructure of Eutectic cast iron bonded to stainless steel with rotation 200 r.p.m.	123

contd./

List of Figures - contd./

		Page No.
54.	Microstructure of 1.4% steel partially bonded to stainless steel.	125
55.	Theoretical time to melt back Vs Liquid heat transfer coefficients.	135
56.	Theoretical time to melt back Vs liquid heat transfer coefficients.	136
57.	General curve for rotating cylinder mass transfer.	140
58.	Maximum Eutectic arrest temperature Vs cooling rate.	142
59.	Chromium and nickel diffusion. Ni plated stainless roll bonded, after Bastien.	145
60.	Diagrams showing the progress of melt back.	148
61.	Air cooling inside Probe divided into two control volumes.	161
62.	Four modes of fluid flow for a rotating cylinder with cross flow.	169

LIST OF TABLES

		Page Nos.
1.	Bond Areas - Double sided ingot cladding.	70
2.	Experimental Conditions and Average thicknesses Eutectic cast iron - 50° superheat.	77
3.	Experimental conditions and average thicknesses Eutectic Cast Iron 90° superheat.	80
4.	Experimental conditions and qualitative results. 3% cast iron.	85
5.	Experimental conditions and qualitative results 1.4% steel.	87
6.	Experimental conditions for eutectic cast iron bonding experiments.	91
7.	Qualitative analysis of different phases in a specimen bonded without rotation.	93
8.	Experimental conditions for 3% cast iron bonding experiment.	91
9.	Thickness results qualitative Sn-Pb at 20°C superheat on Pb insert 68 r.p.m. zero power.	99
10.	Thickness results Qualitative.	99
11.	Thickness results for Sn-Pb Eutectic on Pb insert 20°C superheat 200 r.p.m. zero power.	105
12.	Thickness results for Sn-Pb Eutectic on Pb insert 30°C superheat with 68 r.p.m. zero power.	105
13.	Experimental conditions that just produce melt back Sn-Pb-Pb.	108
14.	Experimental conditions for bonding experiments Sn-Pb Eutectic onto Pb inserts - 68 r.p.m. zero power.	110
15.	Experimental conditions and qualitative results 1.4% steel at 200 r.p.m.	120
16.	Experimental conditions for bonding experiments Eutectic cast iron 200 r.p.m.	124

contd./

List of Tables - contd./

		Page No.
17.	Experimental Conditions for bonding experiments 1.4% steel.	124
18.	Experimental melt back conditions and liquid metal heat transfer coefficients.	137

INTRODUCTION

A composite formed by bonding two metal layers can have distinct advantages over either metal separately since the composite can combine the properties of the two metals. Cladding processes that have been used to produce such composites include casting, roll bonding, strip welding and more recently explosive welding. Each of these commercial processes involves intricate procedures to achieve an acceptable product.

The formation of a good bond requires the two dissimilar metals to be brought into intimate surface contact, by removal of barriers such as oxide or absorbed gas layers.

The rolling and explosive welding methods break up oxide films by causing the metals at the interface to move relative to one another. The other processes remove the oxide layer by melting and allow the solid metal surface to be wetted by a liquid metal which subsequently solidifies.

The present investigation originally aimed to establish conditions under which a bond could be formed between solid stainless steel and mild steel solidified onto it from a mild steel melt. Initially attempts were made to produce a double sided clad ingot by pouring mild steel between two solid stainless steel plates. This work showed that accurate control was required over heat transfer conditions during bonding and experiments were undertaken to investigate these conditions more thoroughly. A hollow stainless steel probe was lowered into a series of molten iron carbon alloys of decreasing carbon content, and the growth and subsequent melt back of the chill layer was studied. In subsequent experiments, bonded layers of the iron carbon alloy were solidified to the stainless steel by passing cooling air through the centre of the probes, after the chill layer had been melted away.

The problem has also been approached from a theoretical point of view by extending the integral profile method to predict the rate at which metal will solidify against a finite wall, cooled on the side remote from the liquid metal.

The theoretical results have been used to analyse the heat transfer processes that occur during the growth of the chill layer and its subsequent melt back.

- - - - - -

2. A LITERATURE REVIEW

2.1 Industrial Clad Materials

Increasingly dissimilar materials are being brought together to solve material problems in all aspects of manufacturing. One of the earliest uses of such material composites was a metal bonded to plastic in the bakelite light switch, but the present list of materials includes plastic coated steel sheet, fibre reinforced materials, duplex tubes and clad sheets.

Sheppard and Brooks[1] have reviewed the major processes that have been used to produce stainless clad steels; the casting processes are becoming less popular in favour of automatic welding and explosive cladding, prompting recent investigations of the mechanism of explosive cladding.[2, 3]

Often thin clad sheets can be more expensive than the equivalent stainless steel sheet but are still used because of the special properties given by the base steel.

The work presented here highlights the difficulty of casting processes and proceeds to explain some of the problems.

2.2 Mathematical Prediction of Solidification Rates

Solidification hascome under increasing theoretical scrutiny in recent years, particularly since powerful computers have become readily available for extensive repetitive calculations.

The technological drive associated with the exploration of space has in addition encouraged a considerable amount of work on ablation of heat shields, a process that has many mathematical similarities with melting and solidification. A few sources cover most of the literature, as each has covered a specific area. Adams[4] includes the classic error function solution of Neumann and goes on to develop from this a set of series solutions for constant surface temperatures. Solidification of a cylinder of liquid metal

at zero superheat is also considered by Adams but this solution is algebraically unweildy. Superheat is dismissed briefly but the effect of a thermal contact resistance between the metal and an infinite mould is considered. Estimated values of the total heat transfer coefficient at this interface, for steel ingots are -- 1000 - 4500 $W/m^2\ ^oC$ (200 - 800 $BTU/ft^2\ ^oF$). He says that if transfer of heat was by radiation alone the value would be about 570 $W/m^2\ ^oC$ (100 $BTU/ft^2\ ^oF$). Adams also considers the solidification of alloys in terms of a latent heat approximated by two different specific heats, but does not compare his results with experiment.

Malhotra[5] has investigated alloy solidification in more detail and he developed a theoretical model in an attempt to describe this.

Cho and Sunderland[6] have applied the heat balance integral technique to heat flow in the liquid but use error functions to describe the temperature distribution in the solid phase, with constant surface temperature as a boundary condition.

In his most recent paper Hills[7] has concisely described a general integral profile solution for pure metal solidification and his method was the basis for the theory developed here. His solution assumes the metal to be either pure or a skin forming alloy. Both the tin-lead eutectic and the iron-carbon eutectic solidify without a flat solid-liquid interface. With tin-lead eutectic the formation of the lamellae causes the interface to be wavy and the interface appears to be flat only on a macro scale. Hogan[8] has observed this eutectic to be 'complex regular'. Chadwick[9] has discussed the solidification of iron carbon eutectic alloys saying that quenching experiments show the graphite sheets grow into the liquid ahead of the austenite. Thickening of these flakes occurs by the diffusion of carbon through the solid austenite. It is likely that these microstructural disturbances do not affect the growth of the solid viewed on a macro-scale.

2.3 Cylindrical Solidification

Glinkov et al[10] have considered the immersion of solid steel cylinders into molten iron 4.1% carbon alloy. They were interested in the delay that occurred before the steel began to dissolve in the melt. Theoretically they made many simplifications such as ignoring the curvature of the chill cast iron layer, assuming it to be in perfect thermal contact with the steel cylinder, and assuming a unique melting point. They expressed the heat flow from the liquid in terms of a heat transfer coefficient and the melt temperature, adjusting this experimentally by bubbling nitrogen into the melt at different flow rates. Whilst they measured centre line temperatures of the cylinders and obtained good agreement for short times, they did not measure the chill layer thickness to compare with predictions. Their results are shown in figs. (1) (2), the solid lines representing the predictions and the points, measured temperatures. Liquid heat transfer coefficients ranged from 4000 - 7000 $W/m^2\,^{o}C$.

2.4 Physical Data

2.4.1 Tin-Lead Alloys

The property values used in the theoretical computation in this work are those of Malhotra[5]. His values for liquid densities differ only slightly (1% for liquid eutectic at 183°C) from those of Thresh, Crawley and White[11], who have completely described liquid densities in the tin-lead system.

The viscosity of liquid lead in alloys is given by Thresh and Crawley[12] in terms of Andrade's equation.

Instead of calculation actual measurement of the latent heat of the alloys could be made by Yamaguchi and Healy's[13] technique. Regrettably they experimented only with lead and Pb 2.5% Sn but they showed good agreement with published values for lead, and with their calculated values of apparent specific heat for the alloy.

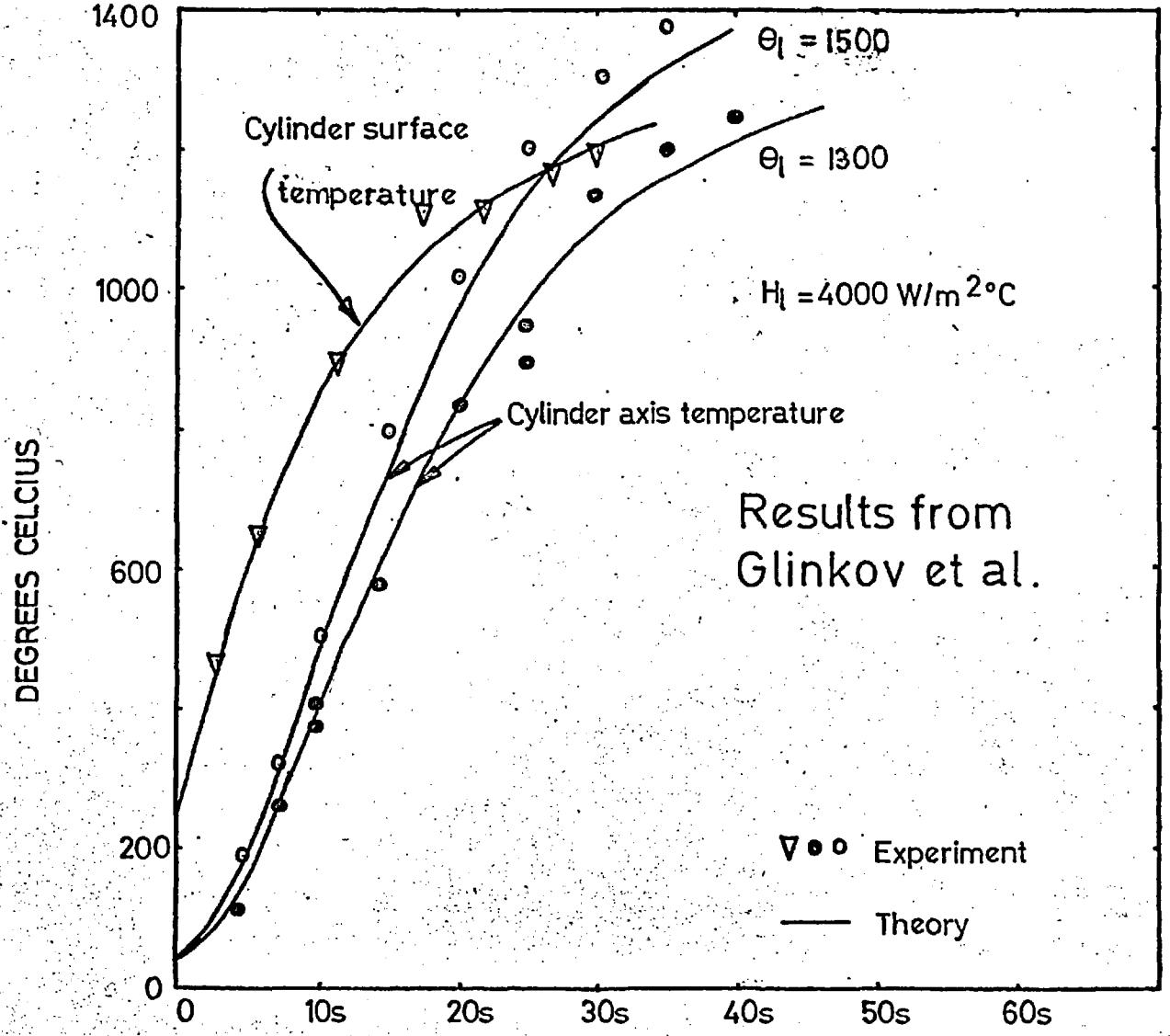
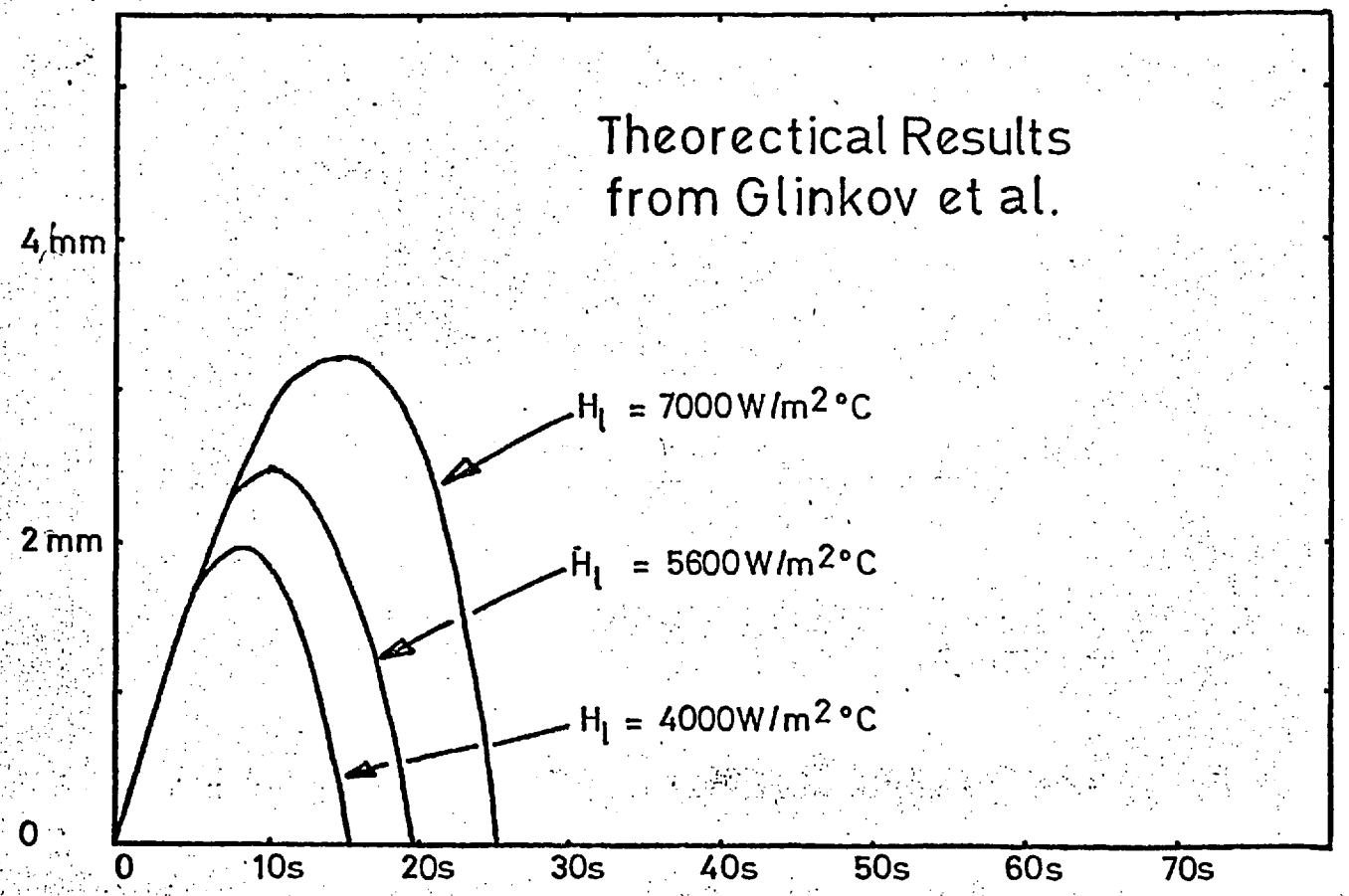


Fig. 1

Temperatures vs. Time. Immersion of solid cylinders in molten cast iron.



Chill Layer Thickness vs. Time

Fig. 2

2.4.2 Ferrous Alloys

There is little physical data available that applies directly to cast iron excepting a few values from Angus[14] and Hillert[15]. Consequently most of the physical values used here were obtained by extrapolation of suitable iron, or iron carbon data[16, 17, 18, 19] to the eutectic cast iron temperature.

The value for the liquid density of cast iron was set above that for solid iron, obtained by interpolation, since solid grey cast iron floats in liquid cast iron. The data for stainless steel was extrapolated from values in ref.[20], it differed only marginally from cast iron as both metals are austenitic at the temperatures considered. The specific heat for stainless steel was the mean from 20° - $1135^{\circ}C$ whilst that for the iron was the value at the experimental temperature.

The latent heat was estimated from three independent calculations for liquid iron transforming to austenite, ignoring the δ ferrite phase change. The value used was selected by comparing the results of these calculations with values used for steel by Pashkis[21], Sargent[22], and Hills[7]. There is insufficient information concerning heats of solutions, carbon, silicon etc. in iron, and their interaction for a fundamental calculation, of the latent heat.

The thermal conductivity of liquid iron has not been measured but the estimate of Richardson[23] was used.

2.5 Thermal Analysis

During 1962 thermal analysis of irons and later, in 1966, of steels became established as a routine technique for carbon analyses.

Kelzer[24] discusses the analysis of steels and presents a table listing liquidus temperatures against carbon percentage, including the correction needed for silicon content. The sample used was .8 kg. Krause[25] details the test used for grey irons, determining carbon equivalent for hypoeutectic irons using a .7 kg sample and Chromel-

Alumel thermocouples. Pontone[26] has extended the technique for hypereutectic irons using a .3 kg sample and Platinum-Rhodium thermocouples. Results for eutectic irons can be obtained by interpolating between these two.

2.6 Rotating Cylinders

2.6.1 Fluid Flow

A considerable amount of work has been done on fluid flow between rotating cylinders, but a large proportion considers either a narrow gap or non metallic fluids. Most of the fundamental work has been reviewed by Dorfman[27] in his section on rotating cylinders.

Originally G. I. Taylor[28] investigated the change of flow behaviour in the gap. He noticed that vortex type instabilities occur for incompressible viscous flow when the outer cylinder was at rest. The instability is formed by regular vortices rotating in opposite senses, completely filling the annular space (fig. 3). He predicted the onset of this instability for a small gap in terms of

$$\frac{R_m^{1/2}\, b^{3/2}\, \omega_1}{\nu}$$

now known as the Taylor number. *

The instabilities started when the Taylor number was greater than 43 when the gap ratio is small.

Kaye and Elgar[29] superimposed axial air flow on air moving between two rotating cylinders. They used a hot wire anemometer, as well as flow visualization techniques and measured the conditions of four modes of flow in terms of the Reynold number and a modified Taylor number,

* This is the original form used by G. I. Taylor. Later definitions differ.

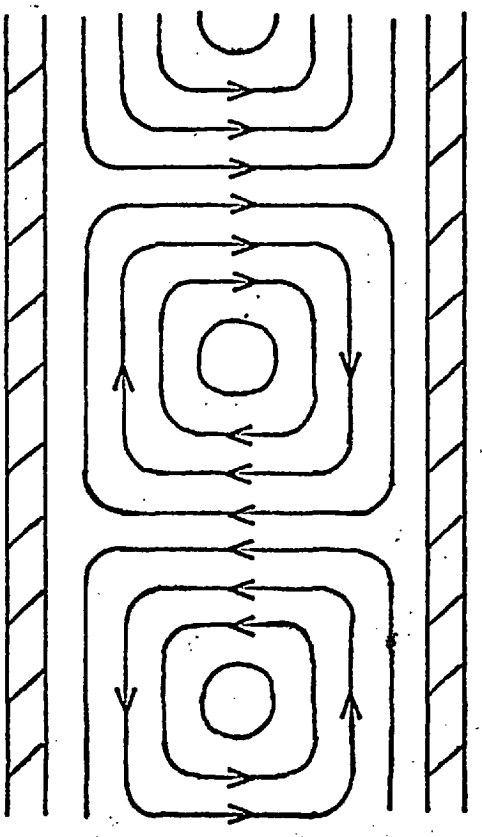


Diagram of Taylor Vortices

in a fluid filling the annular space

between rotating cylinders.

Fig. 3

With no axial flow their results suggest a second transition into turbulance at high Ta($\sim 10^3$), see fig. (62).

Bjorklund and Kays[30] also suggest the existence of a second transition, probably associated with distorted vortices. More recently Sparrow, Munro and Jonsson[31] have carried out an extensive peturbation analysis for the wide gap problem illustrating the limitations of the analysis of Taylor[28] and Meskyn[32]. They produced critical Taylor numbers for laminar instability covering a wide range of rotational speed with different geometries. This allows complete prediction of the laminar-vortex transition for rotating cylinders.

2.6.2 Heat Transfer

The cooling of rotating parts in electric motors has prompted work on heat transfer from rotating cylinders to air. At low speeds natural convection dominates but at higher speeds Etmund[33] and then Dropkin and Carmi[34] showed $Nu \propto Re^{.7}$ for an unbounded cylinder. Anderson and Saunders[35] suggested $Nu \propto Re^{2/3}$ from their work on concentric cylinders and a narrower air gap during conditions where rotation dominates and above the critical Taylor number.

Bjorklund and Kays[36] also found $Nu \propto Re^{2/3}$ for a single cylinder rotating in still air when rotation dominates. In a later paper[30] they carried out concentric cylinder work over a limited range of Taylor numbers (Ta20 - 2000) and geometry (really the small gap problem) and showed $Nu \propto Ta^{1/2}$ above the critical Taylor number. This value of a half for the cylinder rotation speed power dependence is contrary to the most reliable work which suggests .7 power dependence.

2.6.3 Mass Transfer

Rotating cylinders appear to have an attraction similar to rotating discs as a method of conducting mass transfer investigations. It is possible to distinguish between transport and interface control by inspecting the power dependence of rotation speed upon mass transfer coefficients.

There is also the advantage that in the laminar region concentration depends only upon radial distance. Uncertain hydro-dynamic conditions are a feature of much of this mass transfer work. King[37] dissolved rotating zinc cylinders in aqueous acid using baffles, and found a linear dependence of dissolution rate with rotational speed (and hence Re and Ta). Makrides and Hackerman[38] dissolved mild steel but the inner cylinder was not concentric and a linear dependence was found. However, they suggested that surface roughening caused this effect. Ward and Taylor[39] immersed a small copper cylinder in a lead-bismuth alloy, but here the outer case was not a complete cylinder so that again an approximately linear power dependence existed. Jackson and Grace[40] placed a rotating zinc cylinder in bismuth allowing it to dissolve completely at constant revs, and so the Reynolds number decreased to zero during each experiment. They presented the dissolution dependence as nearly linear.

The fractional power of .7 was found by a series of more reliable and detailed work. The system of Roald and Beck[41], magnesium dissolving in acid, showed a power dependence of .71. Eisenberg, Tobias and Wilke[42] whose work has become the standard reference, also presented a .7 power for rotational speed. They dissolved solid organic acids in different glycerol solutions and carried out electrolytic redox reactions. Their analysis showed that the rotor diameter was the correct characteristic dimension to use for Reynolds number. Finally both the mass transfer for their five different systems and the friction coefficients from Theodorson and Regier[43] were to depend upon surface velocity to the power .7.

Sherwood and Ryan[44] confirmed the data of Eisenberg for a benzoic acid-aqueous caustic system and investigated heat, mass and momentum transfer data from five different sources. Their remarkable correlation shows all the data is close to a .7 power dependence on Reynolds number. Sri Krishna et al[45] have shown dissolution of aluminium cylinders in liquid bismuth agrees with Eisenberg's results of .7 power dependence upon rotation speed.

Olssen, Koump and Perzak[46] dissolved rotating carbon cylinders in liquid iron-carbon alloys. Again the .7 power dependence on surface velocity was found and carbon diffusion was correctly deduced to be the rate controlling step. Schenck, Gerber and Steinmetz[47] have carried out similar work but it is less reliable. Their limited data shows a .5 power dependence and their incorrect conclusion is that all previous work is in error because of surface erosion. They show their mass transfer coefficients depend upon the anthracite used in construction of the carbon cylinders. Consequently there must be an element of surface control, which reduced the power dependence. They only considered a narrow range of Reynolds number and were probably experimenting in the duplex control region.

Two other papers are interesting; Pehlke, Goodall and Dunlap[48] dissolved steel cylinders in molten pig iron at undefined rotation speeds. The rate varied with stirring and was again shown to be dependent upon carbon diffusion within the liquid. Lommel and Chalmers[49] looked at lead cylinders dissolving in lead tin alloys and discovered that as dissolution was independent of rotation speed the surface reaction was the controlling step.

2.7 Liquid Metal Heat Transfer

Coombes, Gibbon and Probert[50] in their excellent review of liquid metal heat transfer point out the particular differences of metallic as compared to non-metallic fluids. As a direct consequence of low Prandtl numbers (generally $\sim .05$) the major contribution to thermal resistance in liquid metal heat transfer is not in the thin layer adjacent to the wall. Consequently the heat transfer is sensitive to thermal boundary conditions, the concept of hydraulic diameters is not valid and surface roughness is relatively unimportant.

McAdams[51] gives two theoretical expressions for heat transfer in an annulus based on the Martinelli anology. More recently Dwyer and Tu[52] have calculated unilateral heat transfer for liquid metals in annuli, using current

velocity profile data and the usual assumptions of constant heat flux, fully established turbulent flow, and constant physical properties. Their results are represented by a semi-empirical equation - $Nu = \alpha + \beta (\bar{\psi} Pe)^{\gamma}$ with the equivalent annular diameter as the characteristic length. The three constants depend only upon the radius ratio, different expressions being given for inner or outer wall heat transfer. In the absence of direct evidence to the contrary $\bar{\psi}$ is frequently taken as 1.0, however this paper also presents equations for the estimation of $\bar{\psi}$. They demonstrate good agreement with other equations and with experimental results in annuli.

In a later paper Dwyer[53] says that eddy currents in the lower end of turbulent flow may be such that molecular conduction dominates heat transfer. Under these conditions the Nusselt number is given by $Nu = 4.98 + .662/\eta$ for the inner annular wall. Eddy transport begins to exert an effect in annuli at $Pe \sim 300$ ($Re \simeq 30{,}000$ for $Pr = .01$) The constants α, β, γ in the above equation were modified slightly for a more accurate result.

2.8 Diffusion at an Interface

Bastien[54] has presented diffusion profiles for Chromium, Nickel, Iron, Carbon across the interface of stainless clad steel manufactured by roll bonding. He also pointed out that martensite will form at the interface.

Drewett[55] has reviewed the formation of diffusion coatings on ferrous metals with a general theoretical background. Vanhorn[56] and Kirkaldy[57] have also discussed phase boundary motion during diffusion of binary system metallic coatings.

Castleman[58] considered diffusion bonding analytically and described diffusion between two metals with complete solubility, partial solubility, and for growth of an intermediate phase. Of necessity he assumed diffusion to be independent of composition, that there was no volume change, that the metals were infinitely thick, that

a uniform constant temperature was maintained and that any interface reactions were not rate controlling. He also used some artificial boundary conditions. These assumptions restrict the range of practical situations to which his analysis can be applied.

3. THE THEORETICAL MODEL

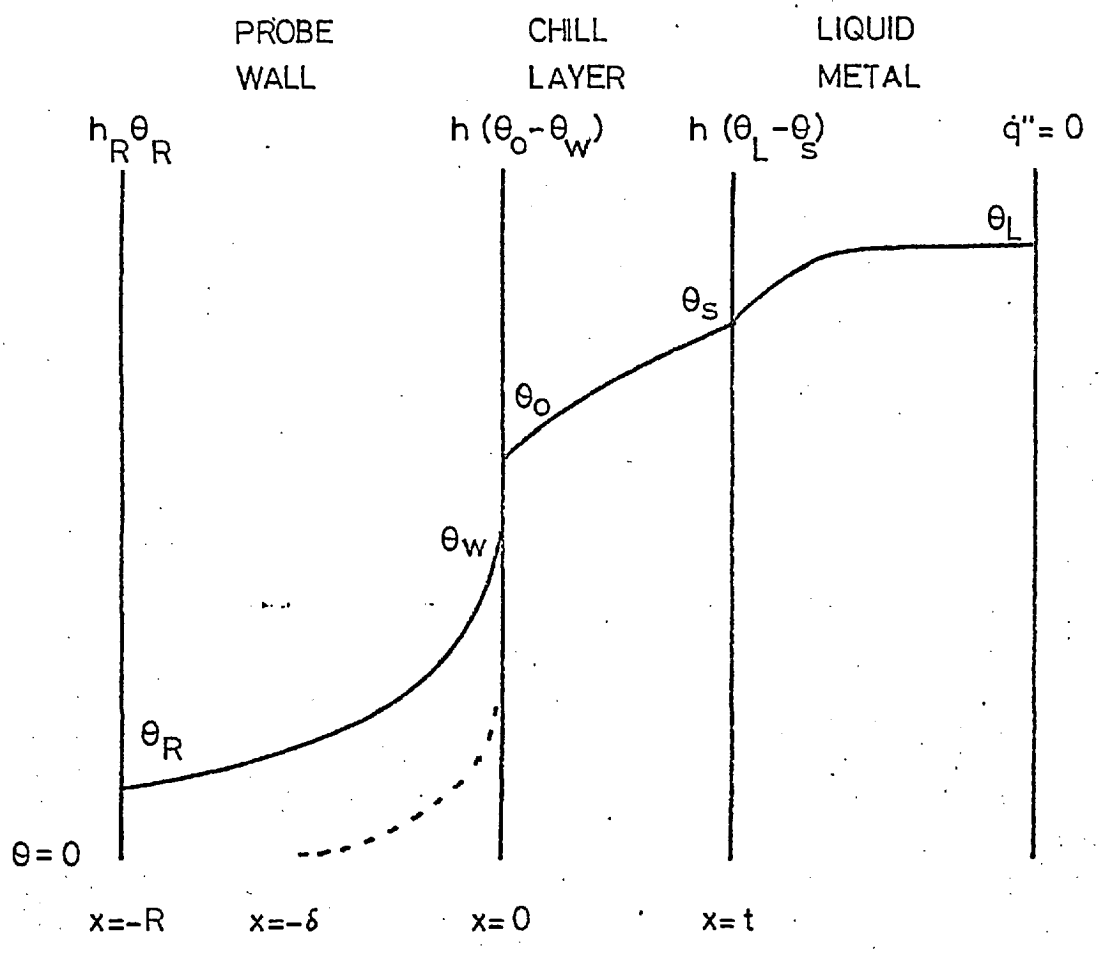
3.1 Introduction

The theory can conveniently be divided into three regions, a complete solution of course requiring them to be considered together. The interfaces of the solidification front and the outer probe surface are suitable boundaries between the liquid, the solid, and the probe or mould wall, fig. (4). The computer solution of the theoretical equations describes the solidification and subsequent melt-back of a liquid metal in imperfect contact with a cold mould wall, cooled at the remote surface.

3.2 Solid Metal Layer

Hills (ref. 7) has developed a generalised integral profile method for predicting solidification rates of pure metals, under certain unidirectional heat flow conditions. He considered a plane interface between solid and liquid metal during solidification and integrated the unsteady state heat conduction equation as applied to the solid metal layer. An approximation to the integral of the heat content of this layer was made by assuming the temperature profile to be a quadratic polynomial. This leads directly to a differential equation for thickness in terms of the surface temperature differential. A further equation linking these two differentials was generated so they may be solved simultaneously. These were expressed in dimensionless terms as -

$$\frac{d\tau^*}{d\zeta} = \frac{2\Lambda}{\Gamma + \sqrt{\Gamma^2 + 4\Lambda\beta}} \qquad \ldots\ldots\ldots (1)$$



- - - - - - Temperature Profile during semi-infinite mode.

Heat Transfer during Growth of the Chill Layer.

Fig. 4

$$\frac{d\theta^*}{d\xi} = - \frac{H^* \left[\frac{dt^*}{d\xi}\right]^2 + q_t^* \left[\frac{dt^*}{d\xi}\right] + t^* f'_\xi}{1 + t^* f'_\theta} \qquad \ldots\ldots (2)$$

where

$$\Omega = H^* t^* (4 + t^* f'_\theta) \qquad \ldots\ldots (3)$$

$$\Gamma = (6H^* + 4(1 - \theta_o^*) - 2t^* q_o^*)(1 + t^* f'_\theta) + q_\tau^* t^* (4 + t^* f'_\theta) \qquad \ldots\ldots (4)$$

$$\Lambda = 6(q_o^* - q_t^*)(1 + t^* f'_\theta) - 3t^{*2} f'_\xi \qquad \ldots\ldots (5)$$

The notation is as used by Hills and given also in (P .173).

f'_θ and f'_ξ are determined from the heat flux into the mould wall.

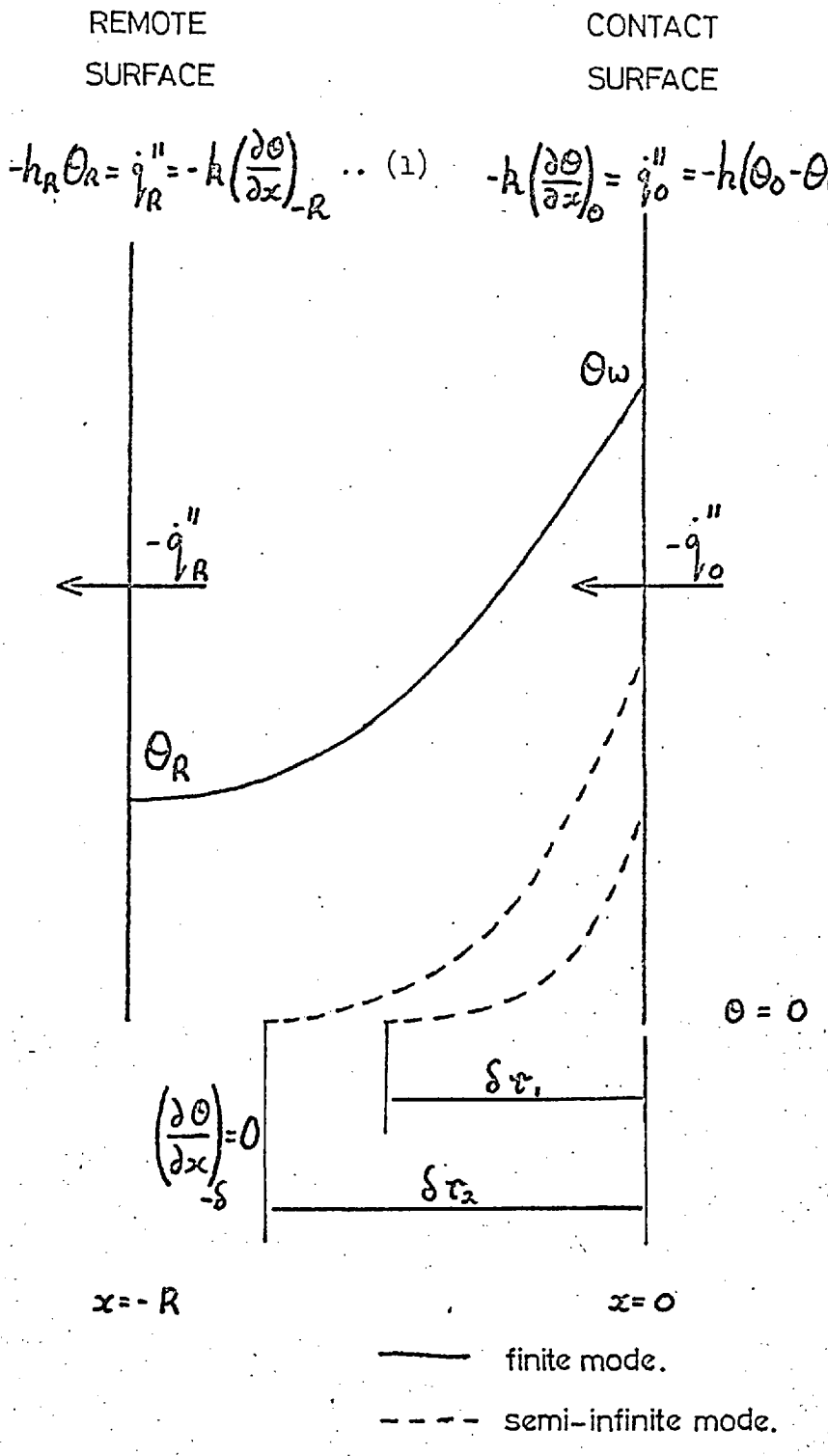
$$q_o^* = f(\theta^*, \xi)$$

$$\frac{dq^*}{d\xi} = \frac{\partial f}{\partial \theta} \cdot \frac{d\theta^*}{d\xi} + \frac{\partial f}{\partial \xi} = f'_\theta \frac{d\theta^*}{d\xi} + f'_\xi \qquad \ldots\ldots (6)$$

The two differential equations can adequately describe the growth of the solid metal layer (when $\dot{q}''_o > \dot{q}''_\tau$) and the remelting of this layer (when $\dot{q}''_t > \dot{q}''_o$).

3.3 The mould or probe wall.

Fig. (5) illustrates the heat transfer process that occurs in the mould during the growth of the chill layer. This layer does not contact the mould wall perfectly so that heat transfer across the interface can be described in terms



Heat Transfer in Mould or Probe Wall.

Fig. 5

of an interface heat transfer coefficient.

$$\dot{q}''_{o} = -h_I(\theta_o - \theta_w) \qquad \ldots\ldots (7)$$

It is assumed that this coefficient is independent of both temperature and time and depends only upon the physical situation.

This is the desired equation for q''_o except that it varies with time in an unknown manner. However its variation can be determined by applying the integral profile method to the wall of the probe.

Two distinct heat transfer modes can be recognised. During the initial stages of the experiment the mould wall surface temperature θ_w rises gradually as the metal solidifies against it, and the internal temperatures vary only within a region close to the interface. This region is bounded by the interface and a diffuse boundary which moves into the wall as the experiment proceeds. This boundary separates the region that has been affected by the heat flux from the region relatively unaffected. The integral profile method replaces this diffuse borderline with a definite but imaginary boundary at a variable distance δ from the interface. The temperature at this penetration depth is zero since it equals the initial probe temperature. (All other temperatures are measured relative to this initial 'zero' temperature). During each experiment the wall heats up and this boundary moves into the wall until it reaches the remote surface ($\delta \rightarrow R$). At this moment the first, semi infinite, heat transfer mode ends. Thereafter temperatures rise throughout the probe wall during the second, finite, mode. Different equations apply for θ''_w during the two modes but they are derived from the same basic equations.

3.3.1 Semi-Infinite Mode

Transient heat flow in the wall is described by the unsteady state heat conduction equation in one dimension

subscript w refers to mould or probe wall.

$$k_\omega \frac{\partial^2 \theta}{\partial x^2} = \rho_\omega c_\omega \frac{\partial \theta}{\partial \tau} \qquad \ldots\ldots (8)$$

Considering the semi infinite mode and integrating this equation from x = 0 to x = $-\delta$

$$\int_{-\delta}^{0} k_\omega \frac{\partial^2 \theta}{\partial x^2} dx = k_\omega \left[\frac{\partial \theta}{\partial x}\right]_0 - k_\omega \left[\frac{\partial \theta}{\partial x}\right]_{-\delta} = \int_{-\delta}^{0} \rho_\omega c_\omega \frac{\partial \theta}{\partial \tau} dx \qquad \ldots\ldots (9)$$

The temperature gradient at $-\delta$ is zero as it is the edge of penetration.

The temperature gradient at the mould surface is related in the normal way (eqn. 2, fig. 5), to the heat flux across the interface. Thus using the Leibnitz Integral Formula* both sides of the equation (9) can be evaluated.

$$h_I(\theta_0 - \theta_w) = \rho_\omega c_\omega \frac{d}{d\tau}\left\{\int_{-\delta}^{0} \theta dx\right\} + \rho_\omega c_\omega [\theta]_{-\delta} \frac{d(-\delta)}{d\tau} \qquad \ldots\ldots (10)$$

The temperature at the edge of penetration $\theta_{-\delta}$ is zero by definition. The integral appearing in the equation cannot be evaluated formally since the probe wall temperature distribution is unknown. It can be estimated however if a simple function is chosen to represent the temperature distribution by satisfying the following boundary conditions.

$$\text{at } x = 0 \qquad \theta = \theta_w$$

$$x = -\delta \qquad \theta = 0, \quad \frac{d\theta}{dx} = 0 \qquad \ldots\ldots (11)$$

A quadratic polynomial is suitable and becomes

$$\theta = \theta_w \left\{1 + 2\left(\frac{x}{\delta}\right) + \left(\frac{x}{\delta}\right)^2\right\} \qquad \ldots\ldots (12)$$

$$\therefore \quad \int_{-\delta}^{0} \theta dx = \tfrac{1}{3} \theta_w \delta \qquad \ldots\ldots (13)$$

---

* Leibnitz Theorem for differentiating an integral with moving limits -

$$\frac{d}{dx}\int_a^b f(x,t)dx = \int_a^b \frac{\partial f}{\partial x} dx + f(b,t)\frac{db}{dx} - f(a,t)\frac{da}{dx}$$

Now by differentiating the profile at x = 0 and using eqn. (7)

$$\delta = \frac{2 k_\omega \theta_W}{-q''_0} = \frac{2 k_\omega \theta_W}{+h_I(\theta_0 - \theta_W)} \qquad \ldots\ldots (14)$$

eqn (10) becomes , using eqn (13, 14)

$$h_I(\theta_0 - \theta_W) = \frac{2}{3}(\rho C)_\omega \frac{d}{d\tau}\left\{\frac{\theta_W^2}{+h_I(\theta_0 - \theta_W)}\right\} \qquad \ldots\ldots (15)$$

This is the desired differential equation for θ_W which when reorganised and written in dimensionless terms becomes –

$$\frac{d\theta^*_W}{d\xi} = \frac{\dfrac{3(\theta^*_0 - \theta^*_W)^3}{2(k^*\rho^*C^*)_\omega} + \theta^{*2}_W \dfrac{d\theta^*_0}{d\xi}}{\theta^*_W(2\theta^*_0 - \theta^*_W)} \qquad \ldots\ldots (16)$$

this includes the differential of θ^*_0 and so must be solved in conjunction with the earlier differential equations. The use of a standard numerical solution involves a small problem since $\frac{d\theta^*_W}{d\xi}$ is always infinite at the start as θ^*_W is zero. This is neatly overcome by writing equation (16) in terms of θ^{*2}_W since $\frac{d\theta^{*2}_W}{d\xi}$ is always finite.

Then if $Y = \theta^{*2}_W$

$$\frac{dY}{d\xi} = \frac{3T(\theta^*_0 - \sqrt{Y})^3 + 2Y\frac{d\theta^*_0}{d\xi}}{(2\theta^*_0 - \sqrt{Y})} \qquad \ldots\ldots (17)$$

The solution requires equations for f'_θ, f'_ξ which are derived from eqn 7 in dimensionless form.

$$q^*_0 = \theta^*_0 - \theta^*_W$$

thus $$\frac{dq^*_0}{d\xi} = \frac{d\theta^*_0}{d\xi} - \frac{d\theta^*_W}{d\xi} \qquad \ldots\ldots (18)$$

substituting from eqn 17 gives

$$\frac{dq^*_0}{d\xi} = \frac{2(\theta^*_0 - \sqrt{Y})}{2\theta^*_0 - \theta^*_W}\frac{d\theta^*_0}{d\xi} - \frac{3T(\theta^*_0 - \sqrt{Y})^3}{2Y(2\theta^*_0 - \sqrt{Y})}$$

and equating coefficients with equation 6 leads to -

$$f'_0 = \frac{2(\theta_0^* - \sqrt{\gamma})}{2\theta_0^* - \theta_w^*} \qquad \ldots\ldots (19)$$

$$f'_\xi = -\frac{3\gamma(\theta_0^* - \sqrt{\gamma})}{2\gamma(2\theta^* - \sqrt{\gamma})} \qquad \ldots\ldots (20)$$

For the numerical integration of equations 1, 2, 17 the initial boundary conditions for zero superheat ($q_\tau^* = 0$) are $\xi = 0$, $\theta_0^* = 1$, $\tau^* = 0$, $\theta_w^* = 0$. all necessary substitutions being made during the numerical procedure.

The semi infinite mode described by equation 17 persists until δ is equal to R the wall thickness, the time for this to occur is found by trial and error. Any integration of these three equations over a finite time step is only considered successful if δ does not exceed R . Unsuccessful integrations are repeated with half the time step and the procedure is continued until the condition is satisfied to any desired accuracy. Once this occurs the semi infinite mode is considered to have ended and the integration is continued with the equations for the finite heat transfer mode.

3.3.2 Finite Mode

Again equation 8 applies and when integrated it becomes

$$k_\omega \int_{-R}^{0} \frac{\partial^2 \theta}{\partial x^2} dx = \int_{-R}^{0} (\rho c)_\omega \frac{\partial \theta}{\partial \tau} dx$$

and as before the heat balance integral is

$$q''_R - q''_0 = (\rho c)_\omega \frac{d}{d\tau} \left\{ \int_{-R}^{0} \theta dx \right\} \qquad \left(\frac{dR}{d\tau} = 0 \right) \qquad \ldots\ldots (21)$$

again the integral is estimated by a profile determined by boundary conditions.

$$x=0 \; ; \; \Theta = \Theta_W ,$$

$$x=-R \; ; \; \Theta = \Theta_R \; , \; \frac{\partial \Theta}{\partial x} = -\frac{\dot{q}''_R}{k} = \frac{h_R \Theta_R}{k} \qquad \ldots\ldots (22)$$

which considers a general case with heat flux from the remote surface characterised by a heat transfer coefficient h_R .

This profile is

$$\Theta = \Theta_W + \left\{ 2(\Theta_W - \Theta_R) + \frac{\dot{q}''_R R}{k} \right\} \frac{x}{R} + \left\{ \Theta_W - \Theta_R + \frac{\dot{q}''_R R}{k} \right\} \left(\frac{x}{R} \right)^2 \ldots\ldots (23)$$

and

$$\int_{-R}^{0} \Theta \, dx = R \left\{ \frac{\Theta_W}{3} + \frac{2\Theta_R}{3} - \frac{\dot{q}''_R R}{6k} \right\}$$

Now by differentiating the profile at x = 0 and using equation (7)

$$\Theta_R = \frac{2k_w \Theta_W - h_I (\Theta_0 - \Theta_W) R}{h_R R + 2k} \qquad \ldots\ldots (24)$$

returning to the heat balance integral equation (21)

$$\dot{q}''_R - \dot{q}''_0 = (\rho c)_w R \frac{d}{dt} \left\{ \frac{\Theta_W}{3} + \frac{2\Theta_R}{3} - \frac{\dot{q}''_R R}{6k_w} \right\} \qquad \ldots\ldots (25)$$

rewriting in dimensionless terms and substituting for the two heat fluxes equations 7, 22.

$$\Theta_0^* - \Theta_W^* - h_R^* \Theta_R^* = R^* (\rho^* c^*)_w \frac{d}{d\xi} \left\{ \frac{\Theta_W^*}{3} + \Theta_R^* \left[\frac{2}{3} + \frac{h_R^* R^*}{6k_w^*} \right] \right\}$$

substituting for Θ_R in dimensionless terms gives this

$$-\frac{d\theta_w^*}{d\xi} = \frac{\left\{ 12 k_\omega^* \{(\theta_o^* - \theta_w^*)(h_R^* R^* + k_\omega^*) - \theta_w^* k_\omega^* h_R^* \} + \frac{d\theta_o^*}{d\xi} \cdot R^{*2} \rho_\omega^* c_\omega^* \{4 k_\omega^* + h_R^* R^*\} \right\}}{R^* \rho_\omega^* c_\omega^* \{4 k_\omega^* (h_R^* R^* + 3 k_\omega^* + R^*) + h_R^* R^{*2}\}} \quad \ldots\ldots (26)$$

differential equation for θ_w^* . As before this equation is to be solved in conjunction with equations 1, 2. In this case, however, f'_θ and f'_ξ are to be derived by substituting equations 26 into 18 and equating coefficients as before, thus

$$f'_\theta = \frac{12 k_\omega^{*2} + 4 k_\omega^* h_R^* R^*}{4 k^* \{h_R^* R^* + 3 k_\omega^* + R^*\} + h_R^* R^{*2}} \quad \ldots\ldots (19a)$$

$$f'_\xi = - \frac{12 k_\omega^* \{(\theta_o^* - \theta_w^*)(h_R^* R^* + k^*) - \theta_w k_\omega^* h_R^*\}}{R^* \gamma^* \{4 k^* (h_R^* R^* + 3 k^* + R^*) + h_R^* R^{*2}\}} \quad \ldots (20a)$$

These expressions can now be used in the integration of equations 1, 2, 26 starting from the values of θ_o^* θ_w^* , and t^* at which the semi infinite mode ended.

Such a numerical solution applies only for zero superheat but may simply be extended to include another differential equation to describe the variation of the melt temperature with time.

3.4 The Liquid Metal

The rate at which heat is transferred to the solid metal surface by convection in the liquid is given by the equation

$$\dot{q}''_t = -h_L (\theta_L - \theta_s)$$

Where h_L is the convection heat transfer coefficient and θ_L is the bulk liquid temperature. This is only valid if solid metal is formed immediately the liquid comes in contact

with the mould wall. The requisite differential equation for Θ_L is given by the overall heat balance on the liquid.

$$\dot{q}''_t = (m'' - \rho_L t) c_L \frac{d\Theta_L}{d\tau} \quad \ldots\ldots (27)$$

Where m'' is the mass of liquid per unit area of mould or probe surface,

$$\frac{d\Theta_L}{d\tau} = \frac{\dot{q}''_t}{(m'' - \rho_L t) c_L}$$

rewriting both of these equations in dimensionless form we obtain :-

$$q^*_t = h^*_L (\Theta^*_L - 1) \quad \ldots\ldots (28)$$

$$\frac{d\Theta^*_L}{d\xi} = \frac{h^*_L (\Theta^*_L - 1)}{(t^* - m^*) \rho^*_L c^*_L} \quad \ldots\ldots (29)$$

Equation (29) is a 4th differential equation to be solved simultaneously with the other three and during solution the value of q^*_t is substituted into equation 2, 5.

3.4.1 Addition of Heat by Furnace Power

Nearly all the ferrous experiments with superheat used furnace power to encourage rapid removal of solid material. Eqn. 27 for the heat balance on the liquid metal is no longer valid. If the rate of heat input is Q W/s then the equation becomes

$$\frac{Q}{A} + \dot{q}''_t = (m'' - \rho_L t) c_L \frac{d\Theta_L}{d\tau}$$

and the rate of fall of Θ_L is reduced.

In dimensionless form this becomes

$$\frac{d\Theta^*_L}{d\xi} = \frac{Q^* + h^*_L (\Theta^*_L - 1)}{(t^* - m^*) \rho^*_L c^*_L} \quad \ldots\ldots (29a)$$

requiring only the addition of an extra term to eqn. 29.

The effect of this extra term is very significant.

3.5 Presolidification

The condition for the 'presolidification mode' is discovered by imagining an infinitely small layer of solid metal on the mould wall surface. If the heat flux to this layer is greater than the heat dissipated the layer disappears.

That is if $h_L(\theta_L-\theta_s) > h_I(\theta_s-\theta_w)$

or $h_L^*(\theta_L^*-1)-(1-\theta_w^*)$ ... 30 is positive

no solidification will occur and the presolidification mode is said to exist, (Modes = 2)

The heat flux to the mould surface is then given by

$$\dot{q}_o'' = -h_L(\theta_L-\theta_s) \qquad \ldots\ldots (31)$$

so that in the semi infinite mode equation 16 is replaced by

$$\frac{d\theta_w^*}{d\xi} = \frac{3/2\, h_L^* T(\theta_L^*-\theta_w^*)^3 + \theta^{*2}\frac{d\theta_L^*}{d\xi}}{\theta_w^*(2\theta_L^*-\theta_w^*)} \qquad \ldots\ldots (32)$$

and as before

$$\frac{dY}{d\xi} = \frac{3h_L^* T(\theta_L^*-\sqrt{Y})^3 + 2Y\frac{d\theta_L^*}{d\xi}}{(2\theta_L^*-\sqrt{Y})} \qquad \ldots\ldots (33)$$

The numerical integration thus involves equation 29, 33 alone until the semi infinite mode is ended, when by substituting eqn. 31 into 35 the following relation for in the finite mode is obtained.

$$\frac{d\theta_w^*}{d\xi} = \frac{\left\{12k_\omega^*\{h_L^*(h_R^*R^*+k_\omega^*)(\theta_L^*-\theta_w^*)-\theta_w^*h_R^*k_\omega^*\} + \frac{d\theta_L^*}{d\xi}R^{*2}\rho_\omega^*C_\omega^*\{h_L^*R^*(4k_\omega^*+h_R^*R^*)\}\right\}}{R^*\rho_\omega^*C_\omega^*\{4k_\omega^*R^*(h_R^*+h_L^*)+12k_\omega^{*2}+h_R^*h_L^*R^*} \qquad \ldots\ldots (34)$$

and the equation for calculating θ_R^* is

$$\theta_R^* = \frac{\theta_w^*(2k_\omega^* + h_L^* R^*) - \theta_L^* R^* h_L^*}{h_R^* R^* + 2k_\omega^*} \quad \ldots\ldots (35)$$

At each step in the calculation a check can be made for the presolidification mode as for the semi infinite mode transfer.

3.6 Computation

The entire theoretical analysis has assumed unidirectional heat flow, and unfortunately heat flows radially through the probe wall and through the growing chill layer. However the method depends essentially on a heat balance, so that any error due to the use of unidirectional heat flow equations can be minimised by adjusting the effective densities of the probe wall and of the growing chill layer. This adjustment referred to allows the heat balance per unit area of the interface to be satisfied, whilst still maintaining the correct thickness for heat conduction in the probe wall and in the chill layer. Thus the effective density of the probe wall is given by

$$(\rho_\omega)_{eff} = \rho_\omega \left\{\frac{R_1 + R_2}{2R_2}\right\} \quad \ldots\ldots (36)$$

and the chill layer by

$$(\rho_s)_{eff} = \rho_s \left\{\frac{R_2 + R_\tau}{2R_1}\right\} \quad \ldots\ldots (37)$$

The use of these effective densities will reduce the error in using the unidirectional heat flow equations.

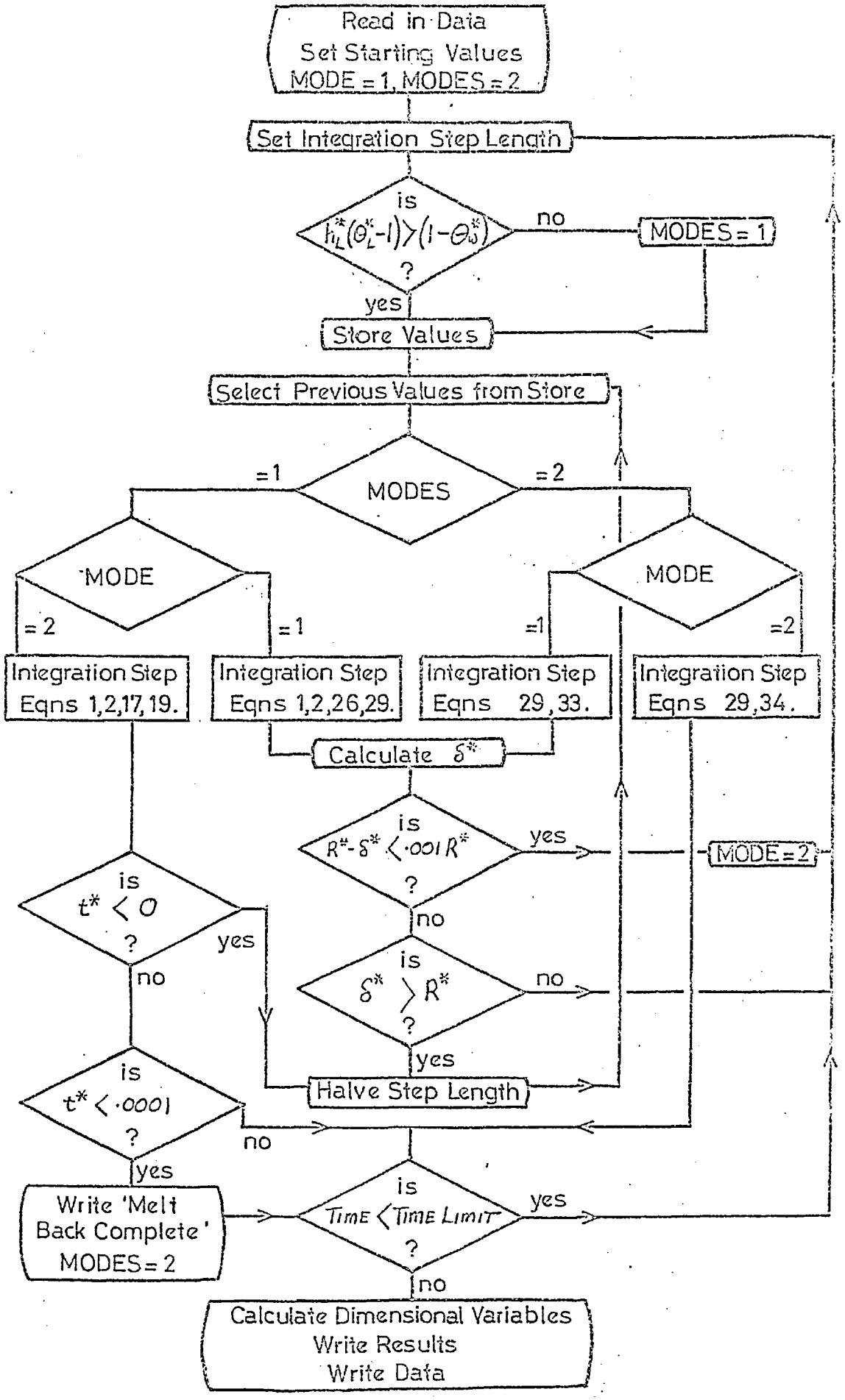
At intervals during the computation the theoretical heat balance was calculated. This checked that the heat given out by liquid metal and the solidifying metal equalled that absorbed by the mould wall. Normally this was accurate to within 1%.

The computation was carried out for each experimental system, with effective densities, at zero superheat. The theoretical curves presented are those which fit these experimental results best. The computation was repeated at superheats used experimentally for different liquid heat transfer coefficients, until melt back was produced at times comparable to the experiments.

If a continued theoretical description is needed when melt back is complete the equations (32, 34, 35) developed for presolidification will detail the continued heating of the mould wall.

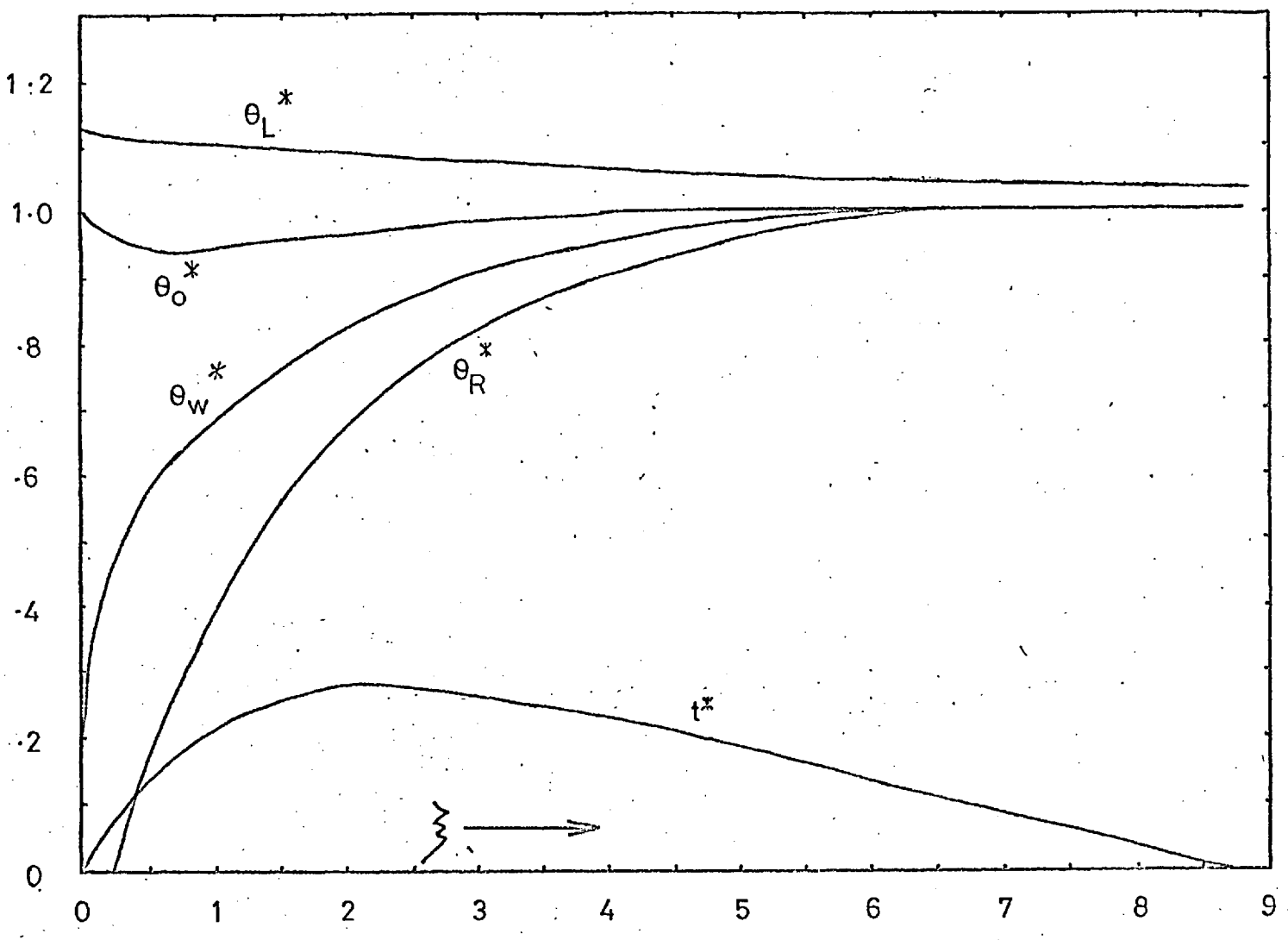
Cooling of the remote surface ($h_R \neq 0$) operates satisfactorily for a fixed value of the remote heat transfer coefficient. For cooling to be applied at the completion of melt back, the growth of a cold layer from the remote surface must be considered in a similar way to section 3.3.1 . The subsequent growth of a bonded chill layer will be in perfect contact with the mould wall and the heat flux from the solidifying metal will not be as described by equation 7 .

Fig. (6) is a simplified logic flow diagram for the programme and fig. (7) presents typical computation results in dimensionless form.



SIMPLIFIED ALGORITHM FOR COMPUTER PROGRAM.

Fig. 6



Dimensionless Results vs. Dimensionless Time. for specimen computation.

Fig. 7

4. APPARATUS

4.1 The Double Sided Clad Ingot

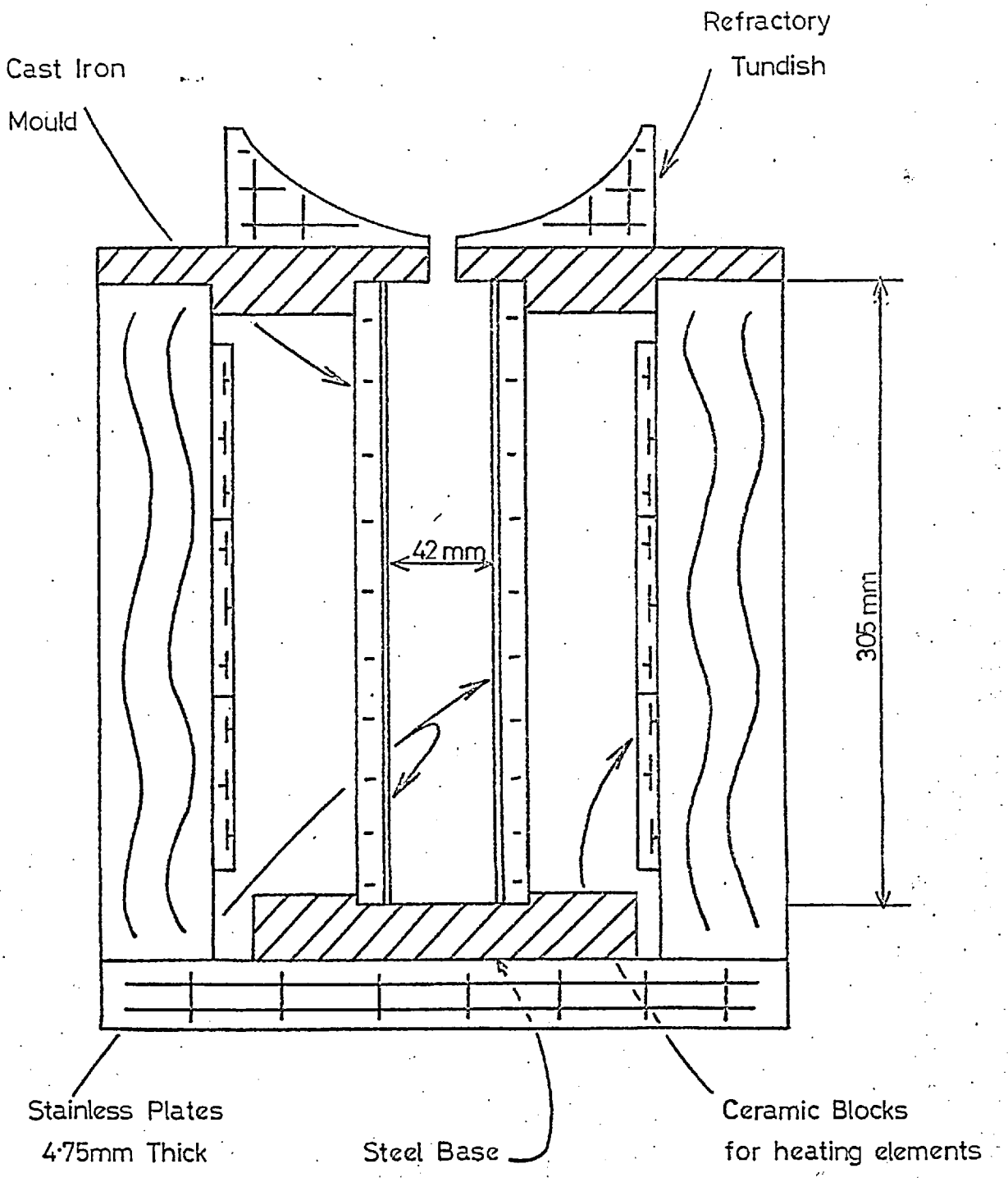
A cast iron ingot mould of internal dimensions; 110 mm x 305 mm x 50 mm, was lined with two stainless steel plates, 4.7 mm thick and the whole assembly was placed in an electric preheating furnace (fig. 8). About 9 kg. of low carbon-steel was melted in a high frequency furnace and after deoxidation it was poured into the refractory tundish and hence into the ingot mould. The temperatures of the mould and the stainless plates were monitored continuously on a potentiometric recorder, using Pt/PtRh. thermocouples and the melt temperature was measured immediately prior to pouring with a similar dip thermocouple.

4.2 The Liquid Metal Furnaces.

4.2.1 Ferrous

The 22 kg. high frequency furnace (fig. 9) was of standard construction with an acid refractory lining and was powered by a 50 kW. 5 K Hz generator. Slag formation on the melt surface was inhibited by enclosing the open top with a 'syndanio' cover and introducing forming gas to purge the atmosphere. The liquid metal temperature was measured continuously with a Pt/Pt 13% Rh thermocouple protected by an impervious cermet* sheath.

* Metamic 519, a molybdenum-alumina cermet, showed perfect thermal shock resistance and gave a very rapid response time. It was possible to observe the cessation of thermal convection currents during the solidification of cast iron. At high temperatures ($\sim$1300°C) in even mildly oxidising atmospheres volatalization of Molybdenum occurred reducing the life from about 10 hours immersed to less than an hour.



Preheat Furnace for Double-sided Cladding of a Steel Ingot

Fig. 8

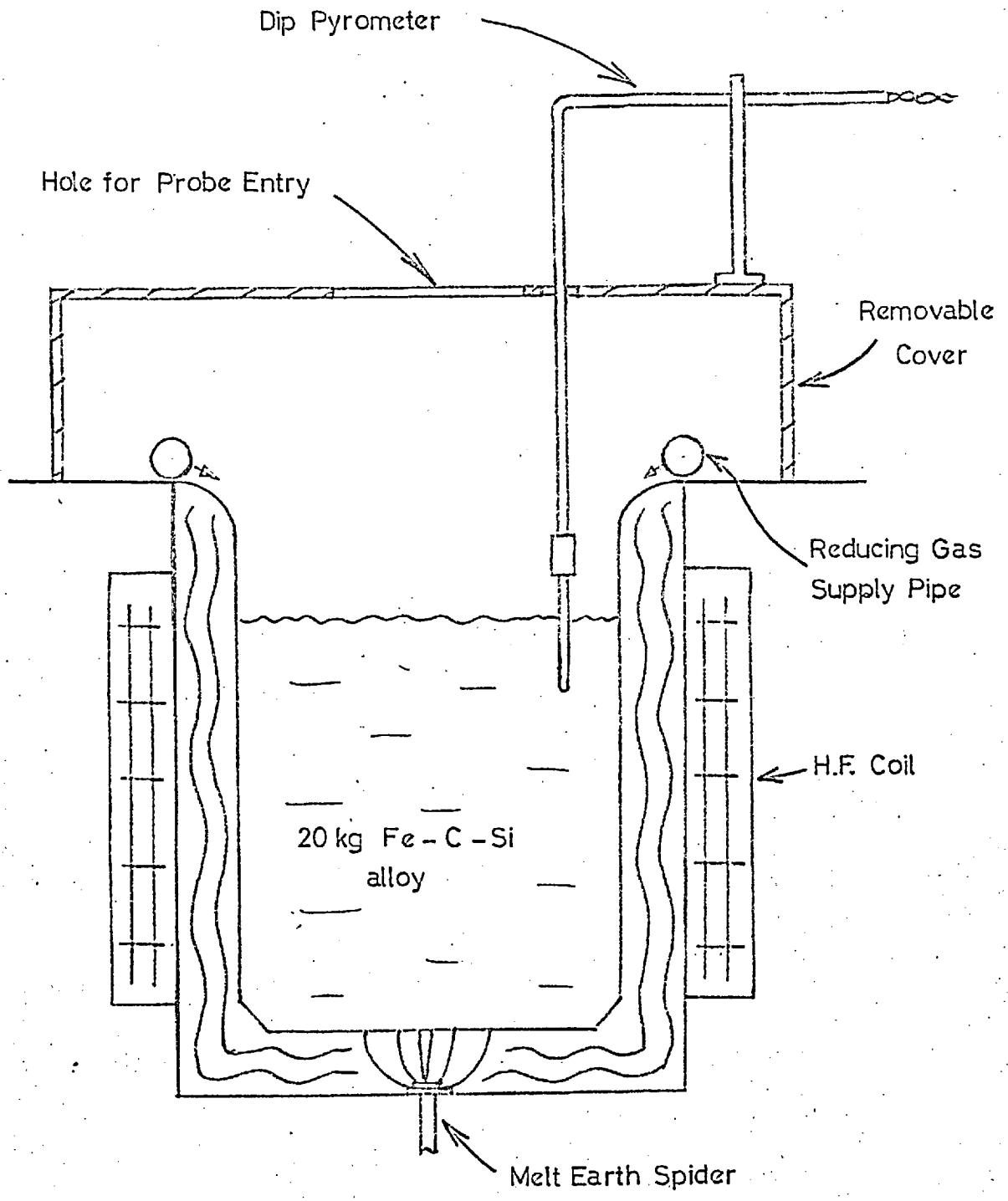


Diagram of Ferrous Melting Furnace

Fig. 9

4.2.2 Lead Alloy Furnace

This furnace (fig.10) consisted of a large austenitic stainless steel crucible, which contained 10 kg. of lead-tin eutectic alloy. It was powered by a 2 kW. 'thermocord' heater wrapped outside the crucible, and a 1 kW. mineral insulated, stainless sheathed heating coil immersed in the alloy. These were connected respectively to a fast cycling thyristor controller and a variable transformer. Heat losses were minimized by 100 mm of vermiculite insulation. The alloy was melted and remelted inside, but the assembly could be tilted if required to pour out the alloy. The bulk liquid temperature was measured by a stainless sheathed chromel/alumel thermocouple with its tip about 3 cms. below the liquid surface, connected via a cold junction to the data logger.

4.3 The Cylindrical Probes

4.3.1 Stainless Steel

Each probe (fig. 11) was made from a stainless steel cylinder, type 304L, with a heavy plug of the same material screwed into the bottom, as welding of the plug would have produced a potential weakness. This plug allowed chromel/alumel thermocouples to be spot welded onto the inside wall (fig. 12) and enabled the thin walled air cooling pipe to be centred accurately within the cylinder.

The probes were supported by three threaded rods adjusted to reduce rotational eccentricity to a minimum. The rods were supported on a flange that, in the case of the rotation experiments, was part of the rotation assembly.

4.3.2 L e a d

In order to overcome the problems involved in the manufacture of complete probes from lead, a stainless steel

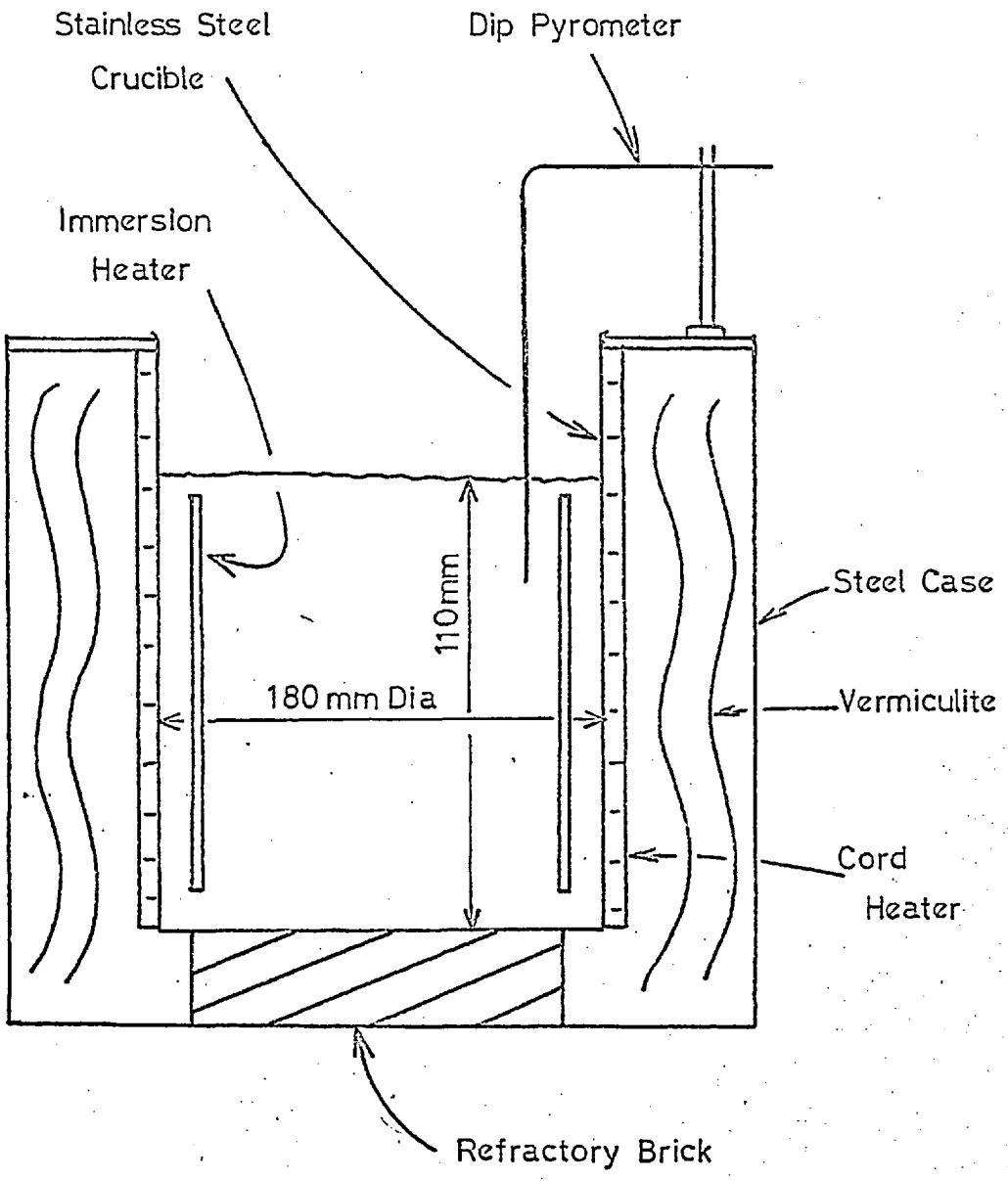
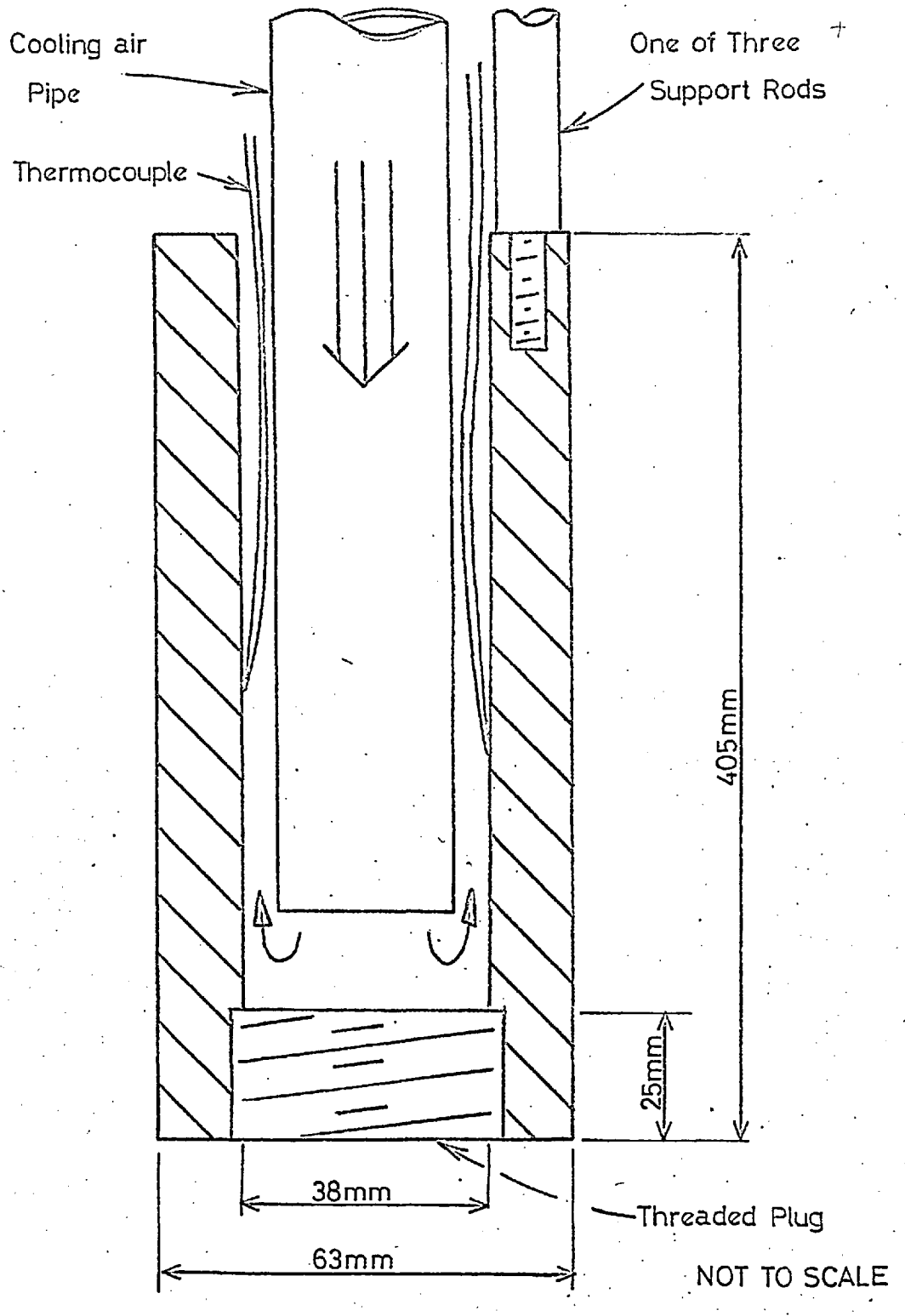


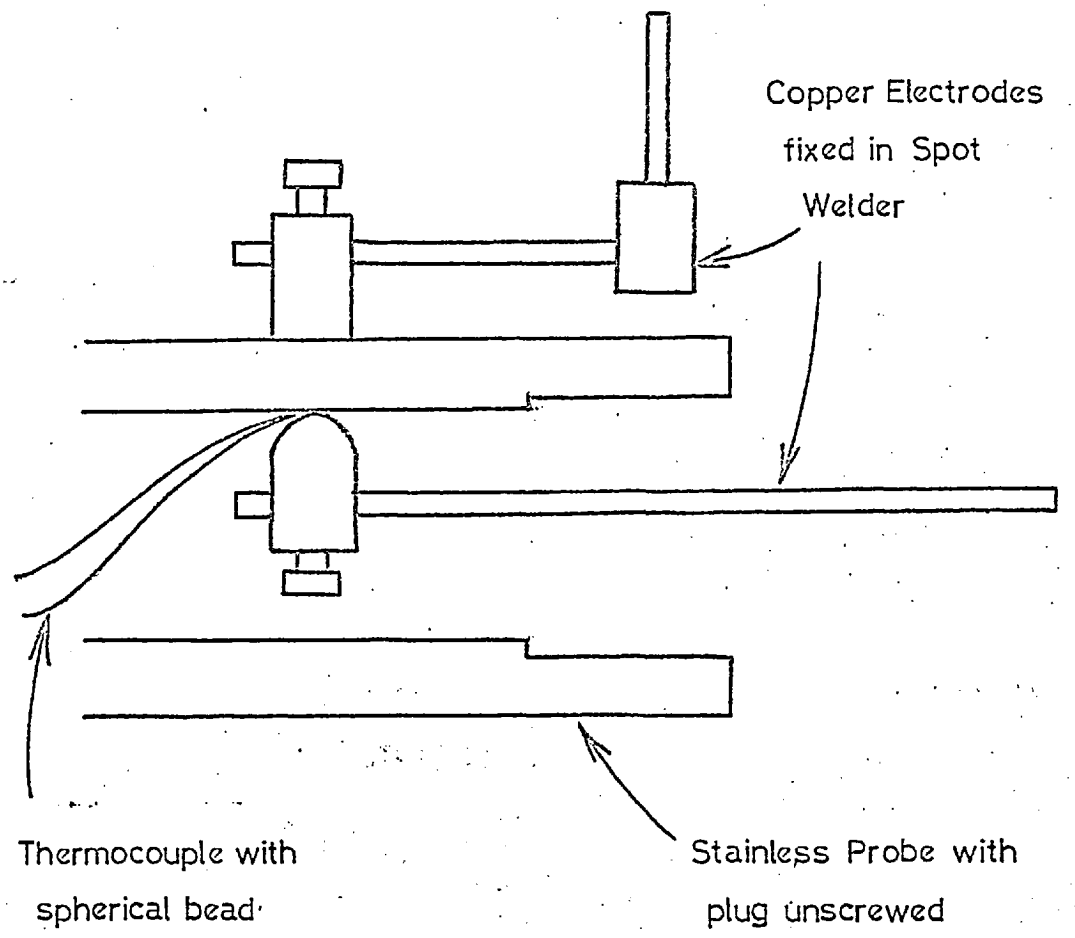
Diagram of Tin-Lead Melting Furnace

Fig. 10



Section of Stainless Steel Probe.

Fig. 11



Equipment for Spot-welding Thermocouples inside Stainless Steel Probes.

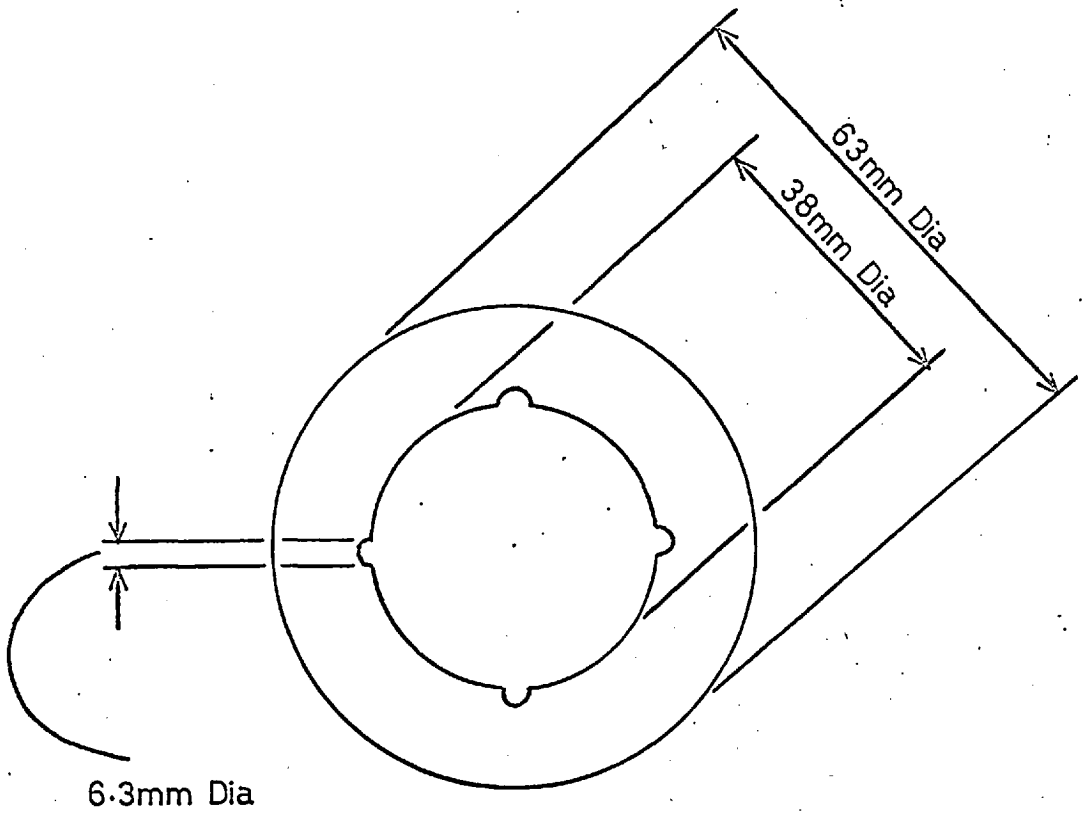
Fig. 12

probe was designed that contained an active section of lead. This consisted of an insert (fig. 13) that was made by casting in a permanent steel mould. After machining the end faces of the insert it fitted precisely over a stainless steel cage (fig. 14) which screwed into the upper section of the stainless steel probe, so that the parallel faces of the insert and the stainless provided an airtight seal. A stainless steel cap was screwed over the bottom end of the cage sealing the probe,(fig. 15) shows this assembly. Thermocouples were fixed to the inner wall of the insert using high temperature 'araldite' and the leads travelled up to the terminal block on the rotating assembly, through the narrow annulus between the air pipe and the probe wall.

4.4 Rotation of the Cylinders

The rotation assembly provided a compact vibration free support that allowed continuous rotation of the probe, an uninterrupted supply of cooling air and continuous monitoring of three thermocouple outputs. (Fig. 16) shows a section of this assembly which was supported on the central stator (d) by a ballrace (a). The friction drive wheel was held against the top rotor (g) and the side thrust resisted by another ballrace (b). The central pipe supplying the air cooling was stationary, eliminating the need for a rotating gas seal. Six copper rings (c) were bonded by 'araldite' to an ebonite sleeve, which was in turn fixed to the stator. The six copper connecting wires led out through holes in the stator.

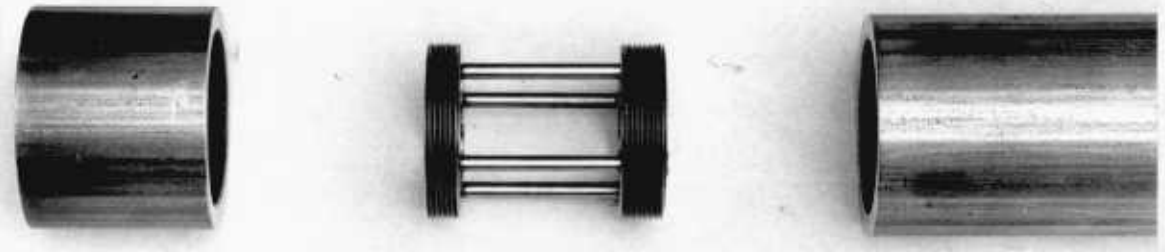
The contact brushes (e) were of cold rolled copper-Beryllium, set at an oblique angle so that the ring surface was continuously wiped clean. They were mounted in a 'Tufnel' block (f) on the rotating assembly which also served as the terminal block for the thermocouples. The tube (i) carried the cooling air and was stationary inside the probe supported by steel rods (h). The rotation drive was from a series wound A.C. motor via a



Plan View of Cast Lead Insert

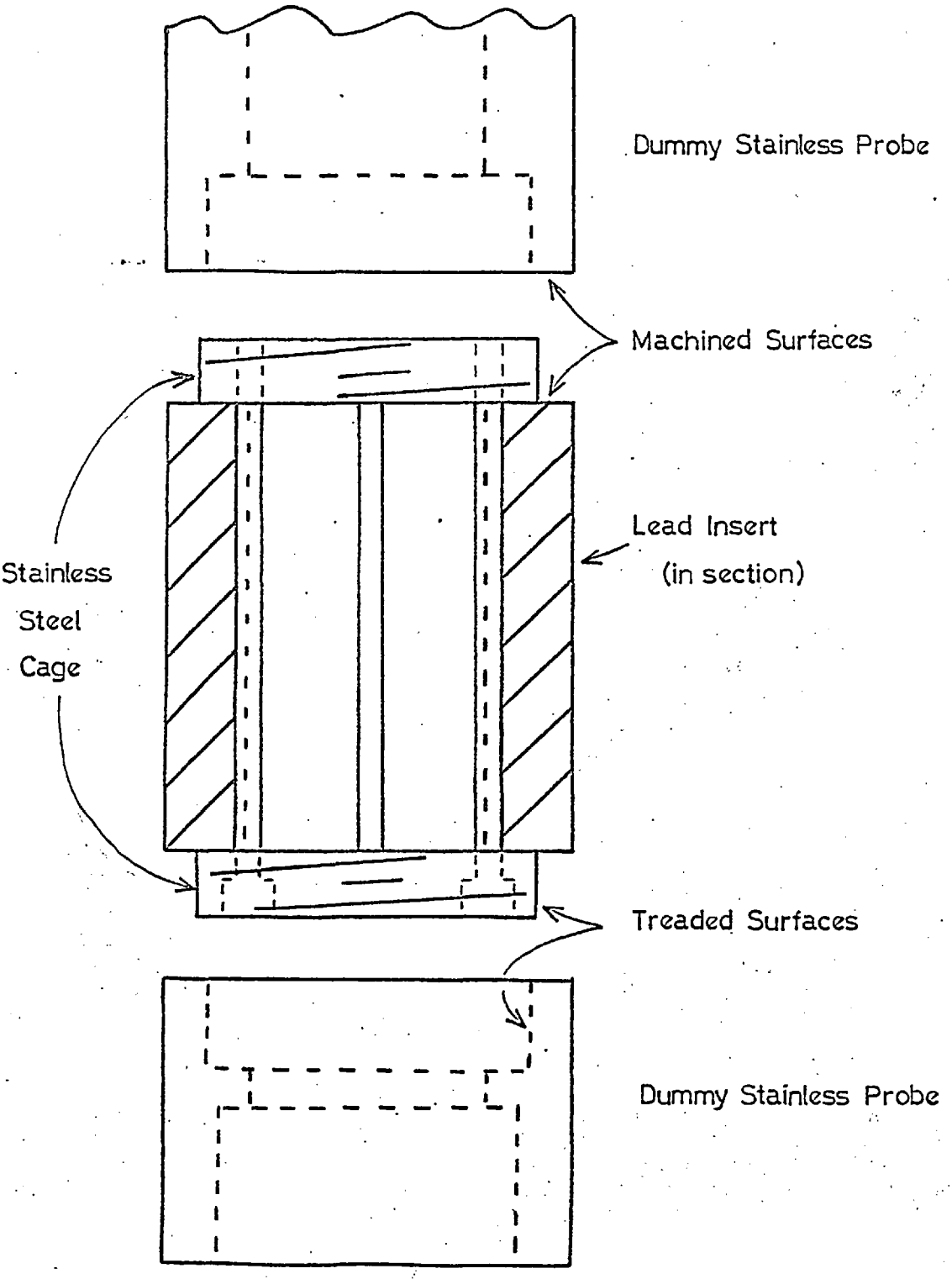
showing the four recesses which exactly matched the cage.

Fig. 13



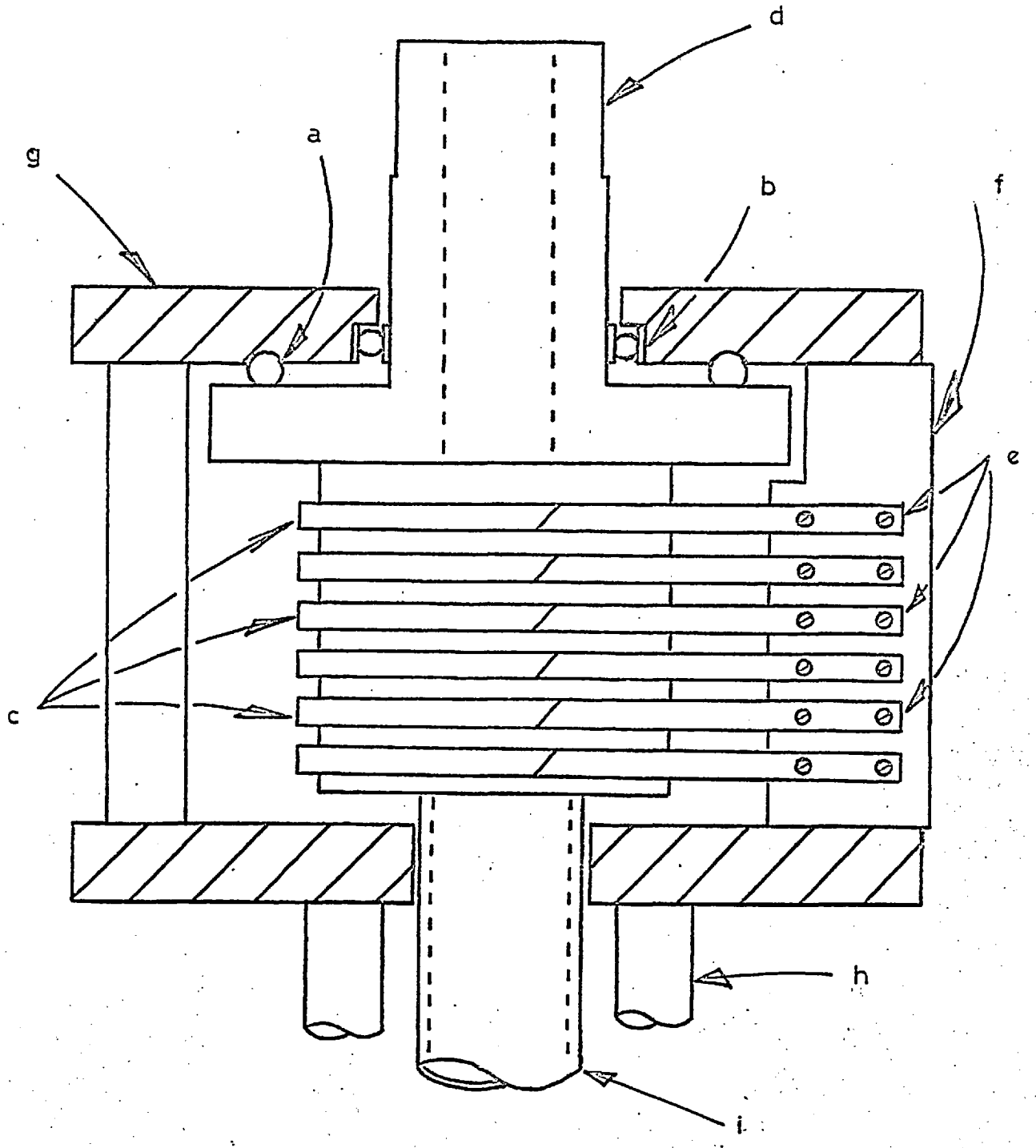
STAINLESS STEEL CAGE without Lead Insert.

Fig. 14



Section of Lead Probe Assembly.

Fig. 15



Section of Rotating Probe Support with Sliprings.

Fig. 16

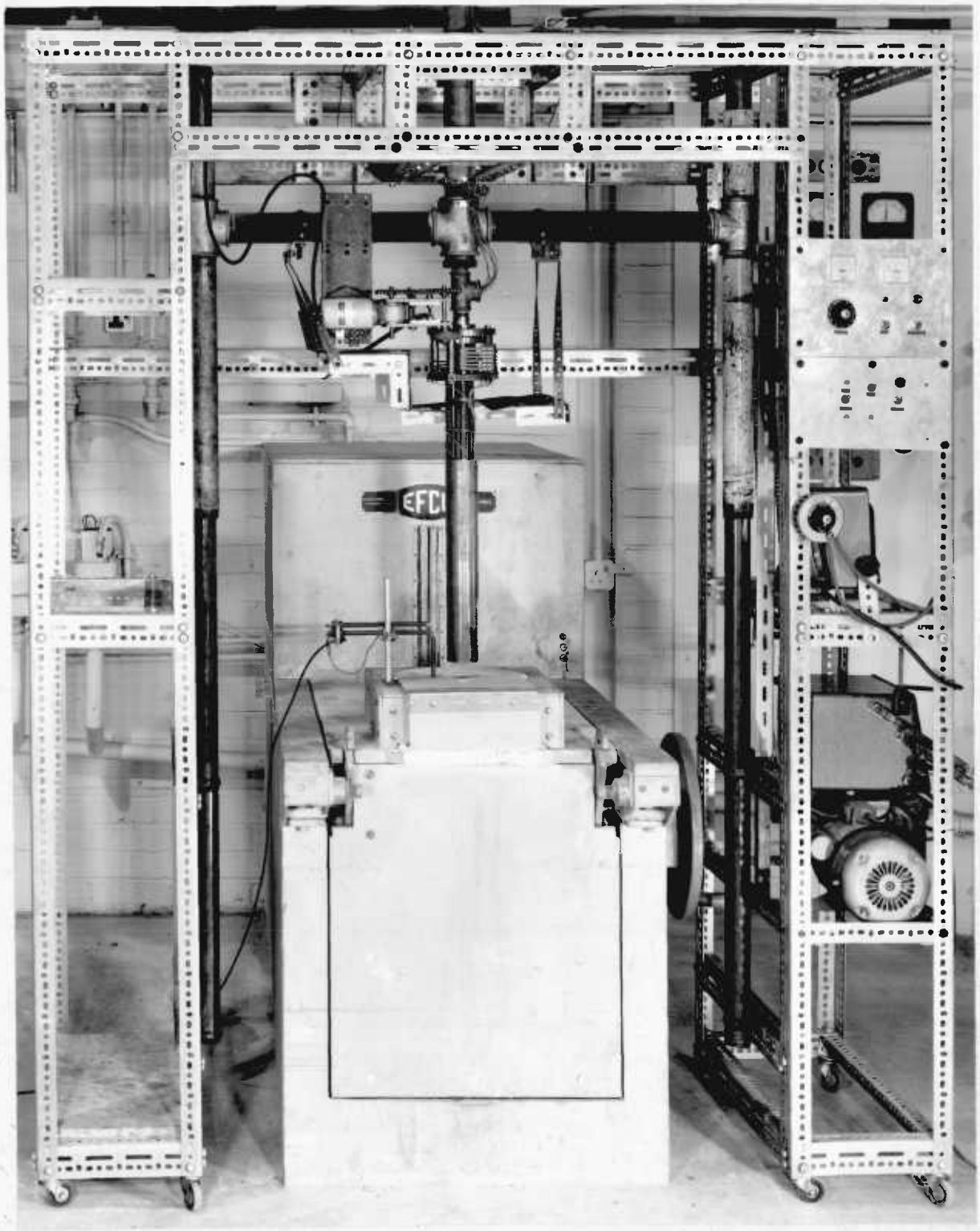
small chain to the rubber friction wheel held in contact with the rotor by a tension spring. The speed was monitored by a stroboscope set to flash at a frequency equal to twice the assembly rotational revs.

4.5 Ancillary Equipment

The probe assembly was supported by a moveable gantry which lowered the probes smoothly, at a fixed speed, into the liquid metal (fig. 17). The travel was limited at its upper and lower positions by micro switches. The entire gantry was moveable to enable the probes to be lowered into either the lead or ferrous metal baths.

The cooling air supply was from a Rootes blower via a pressure relief valve, by-pass valve, orifice plate, and solenoid valve, through a flexible coupling onto the central probe support stator. (fig. 18). The relief valve protected the blower, the by-pass valve controlled the air supply, and the solenoid valve allowed abrupt cut off of the air supply in an emergency. The forming gas flow rate was monitored by a rotameter.

Temperatures were recorded as millivolt readings on the 'Dynamo' data-logger, except during the ferrous liquidus arrests when a 'Leeds and Northrup' potentiometric pen recorder plotted the cooling curves. The data logger was entirely immune to mains or high frequency leakage, but the pen recorder required a hum/filter and a common earthing point with the ferrous melts to eliminate stray leakage currents.



A STAINLESS STEEL PROBE suspended from the Gantry over the Ferrous Furnace.

Fig. 17

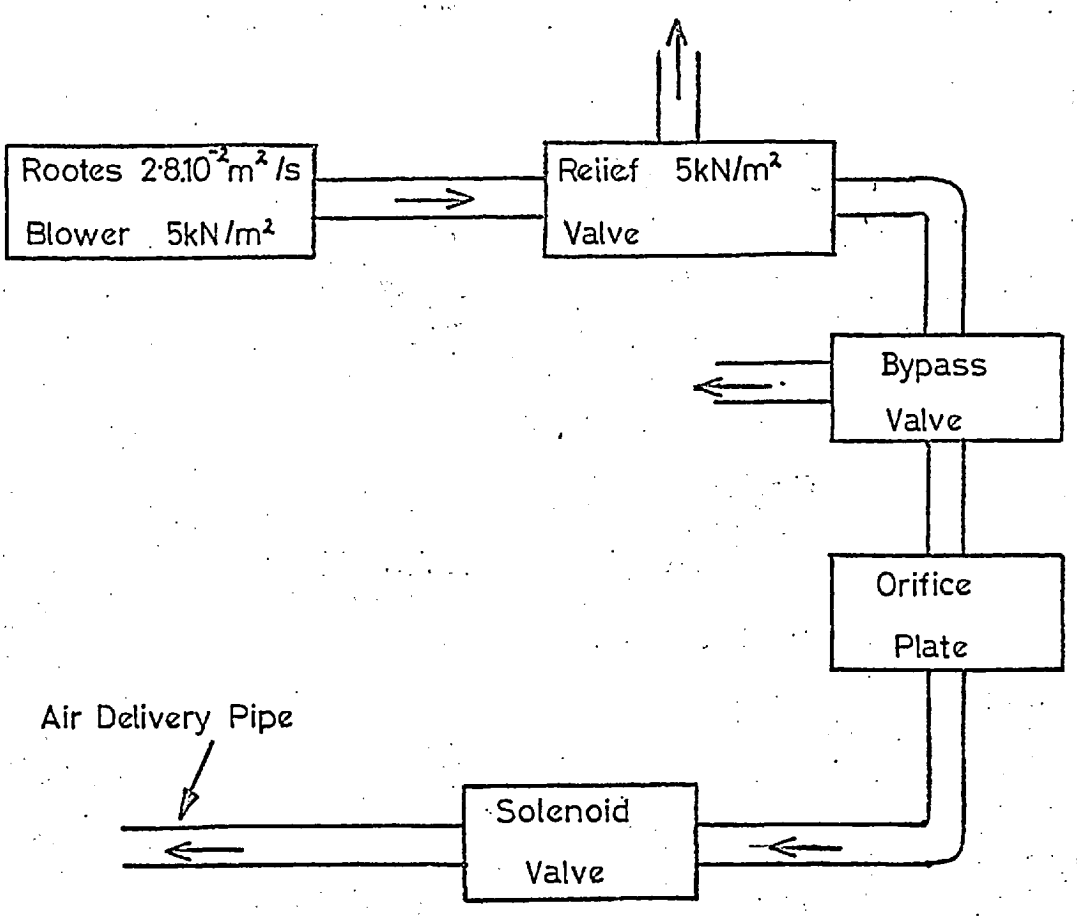


Diagram of Cooling Air Supply System.

Fig. 18

5. EXPERIMENTAL TECHNIQUE

5.1 Double Sided Ingot Cladding

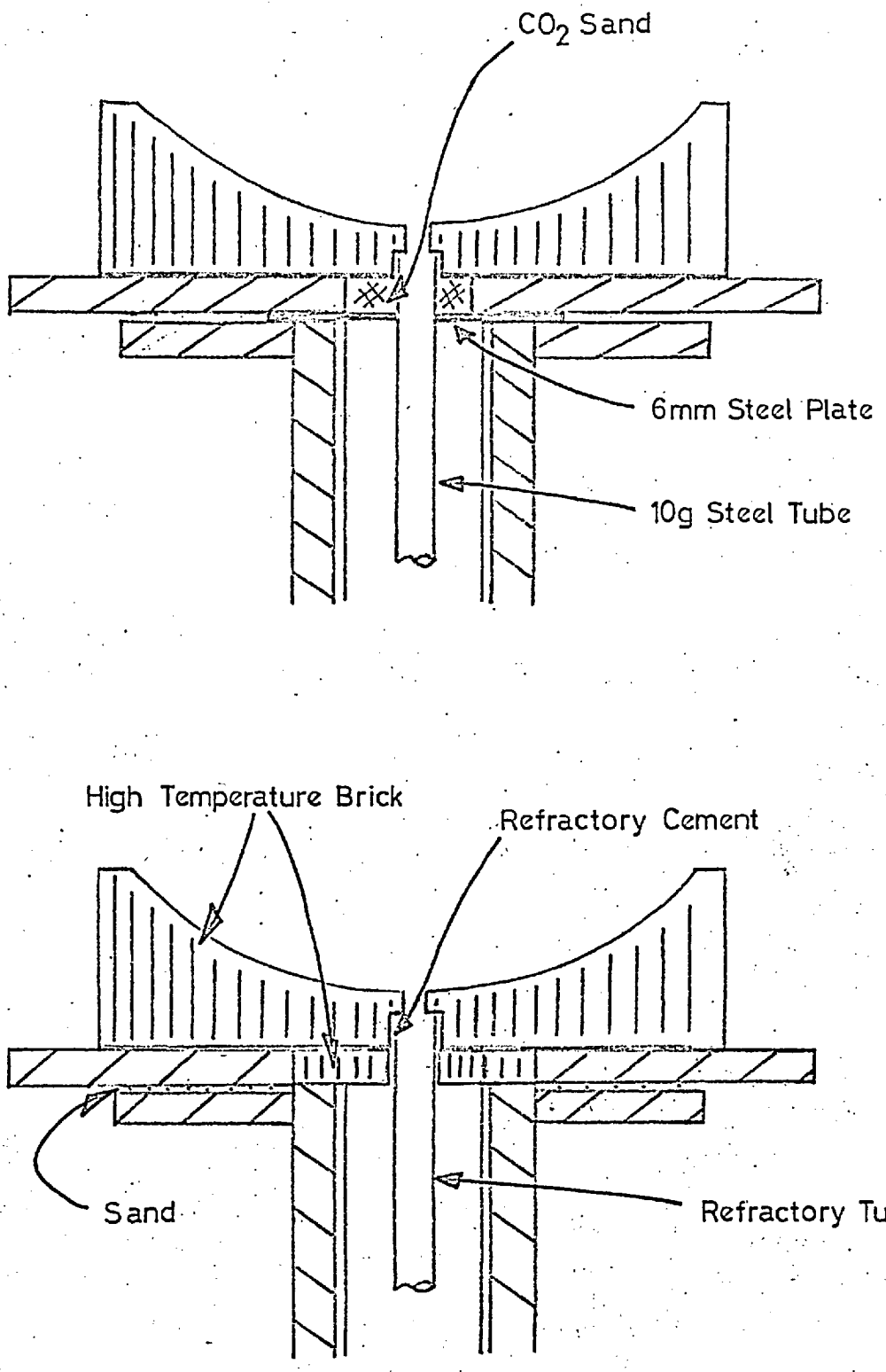
For the initial experiments the stainless steel plates were degreased, scratch brushed and quickly placed cold in the mould, immediately prior to casting. Only limited local bonding was produced despite gradually increased casting temperatures. Different surface preparations, including Copper and Nickel plating (these oxides are unstable at high temperatures), were used, with preheating the plates in situ under a non oxidising atmosphere, but there was no consistent improvement. Mould preheat (600 - 700°C) originally appeared to encourage bonding but problems of metal leaking behind the plates and, worst of all, the plates themselves melting soon showed that success was out of reach, despite several different plate fixing techniques. The stainless plates were fixed in the moulds by simple clips, refractory clays and 'autostick', but none of them was outstandingly successful. Modification of metal flow during the top pouring, causing the liquid to enter the mould through an internal tube, fig. (19), did not cause improvement, despite four different steel and refractory pipes. The areas of bond were measured by a planimeter after ultrasonic testing delineated the borders between bond and no bond.

The choice of process intrinsically limited the control of melting and casting. The melting of relatively pure iron in the small furnace was difficult without a small cast iron alloying addition to improve fluidity. Liquid metal temperature measurement was an exacting aspect of control which was finally solved by the cermet thermocouple sheaths.

5.2 Ferrous Experiments with Probes

5.2.1 Experimental Sequence

Each experiment began by melting the weighed charge in air, followed by removal of slag. The top gas cover was



Arrangement of 'Splash' Tubes inside Moulds.

Fig. 19

then positioned and the reducing gas supply started, and the melt pyrometer positioned with its tip 30 mm below the liquid surface. The melt was cooled and stirred simultaneously until the primary arrest point was reached. This allowed the composition to be checked from the phase diagram. Finally the liquid surface was skimmed again and the required melt temperature was selected by controlling the power input to the furnace. Lowering the probe for immersion was initiated manually. The static exposure time, from the moment the lower limit switch tripped automatically, to the manual start of lifting the probe from the liquid, was measured by a stopwatch.

The experiments began with immersions into eutectic cast iron, followed by 3% * cast iron, and finally 1.4% * steel. This gradual progression up the liquidus slope exploited completely the expertise gained at the lower temperature.

Bonding experiments followed directly after melt back was completed. The heat removed by the cooling air, at $10^{-2} m^3/s$, was 1.5 kW, which meant that the furnace power had to be reduced for solidification to occur.

5.2.2 Thermal Analysis

After melting each charge and removal of slag formed, the melt was cooled and stirred simultaneously. The cooling curve, as displayed on the high speed recorder, showed a pronounced arrest point at the eutectic point in 4.3% cast irons and a smaller, but still noticeable, arrest at liquidus temperatures in the two other alloys. If the liquidus temperature differed from that required a suitable addition of cast iron was made and the liquidus then rechecked. The accuracy of such a technique depended largely upon the reproduceability of liquidus arrest points, which was probably no better than $\pm$ 10°C. With the

* Carbon equivalent.

eutectic melts the small liquidus arrests were entirely suppressed by the eutectic arrests which were themselves within $\pm$ 4°C.

Removal of small liquid samples (~ .5 kg) and observation of solidification temperatures was only successful in demonstrating the pronounced arrests. To show smaller changes a slower cooling rate is needed, which required separate samples of at least 2 kg. The scale of operation did not permit this.

5.2.3 Experimental Control of Temperature and Composition

5.2.3.1 Eutectic Cast Iron

Cast Iron of the eutectic composition was chosen for the first experiments because of its unique melting point and the ease with which it can be handled and controlled.

Trial experiments were carried out in a 9 kg high frequency furnace, under similar conditions of acid lining and reducing atmosphere to that used in the larger furnace. They showed that, once slag had been removed after melting, it was possible to maintain a clean metal surface for up to half an hour except for a small amount of slag in a thin ring where the melt contacted the lining.

At first it was difficult to control the iron melt temperature and composition in the larger furnace. The eventual use of Metamic 519 as a thermocouple sheath material enabled reliable temperature measurement and control to be achieved. The melt temperature responded very slowly to manual power adjustments and during the time taken to correct any overshoot the composition drifted from that desired. The control of composition was exacerbated by a lack of rapid on line analysis; baths of acceptable composition were finally obtained however, by adjusting the initial charge composition and by using thermal analysis.

5.2.3.2 3% Cast Iron

Cast irons with a carbon equivalent content of 3% have a liquidus approximately halfway between the eutectic temperature and the estimated melting point of the 304 L stainless steel from which the probes were made.

The composition of these melts was known less precisely than with the eutectic irons. Attempts at thermal analysis were of little use; the liquidus arrests were supressed and the iron solidified white. The composition of these irons was known from the average charge composition, after an allowance for carbon loss during melting.

5.2.3.3 1.4% Steel

The 1.4% carbon equivalent irons possesses a liquidus which coincided with the estimated melting point of the probe material (1420°C). As prolonged exposure of the stainless steel at any superheat was now likely to melt the probe, auxilliary contacts on the recorder monitoring the inside wall temperatures were used to trip an alarm when the probe wall exceeded 1200°C. Cooling air could then be applied to keep the stainless solid.

5.2.4 Experimental Measurement

The accuracy with which the ferrous bath temperatures could be measured was several times better than that with which it could be controlled.

The real exposure time for any point on the probe was calculated by adding to the static exposure time, the time taken for each point on the probe to travel in and out of the liquid. The rotational speed of the probe assembly was preset before each dip, and maintained constant by manually adjusting the voltage to the motor during immersion.

The solid shells were easily removed once they were cracked (the use of a heavy hammer assisted the propagation of these cracks). When the pieces were assembled they formed a complete cylindrical shell, with its bottom.

Thickness readings were obtained from this shell by averaging individual ball ended micrometer readings taken from eight positions equally spaced around the circumferences of a circular section. Up to eighteen different sections on each shell were measured in this way and each section corresponded to a particular exposure time.

5.2.5 Preparation of Microstructures

It was easier to keep specimen flat during polishing if two specimen were placed together, with the comparatively hard stainless on the opposite sides of the mount. Preparation followed the normal pattern, with special care to avoid dragging out graphite from the grey irons. The final polish used 1/4 μm diamond on a low napp cloth.

Etching these composites is difficult, conventional solutions which attack stainless steel would completely destroy the low alloy metal. It was found that Beraha (59) used an alcoholic solution of hydrochloric and selenic acids which selectively deposits elemental selenium on both cast iron and stainless steel. The mechanism is probably reduction of selenic acid by hydrogen released from cathodic areas. Thin film interference within this fine deposit causes the surface to show different colours.

The mounted specimen were immersed in 2% Nital for 10s, and then for about 10 min. in a solution of 100 cc ethyl alcohol, 5 cc hydrochloric acid, 1 cc selenic acid. During the second process the composite was watched and removed from the solution when the stainless had turned a uniform red colour. Prolonged etching or the use of old solutions occasionally caused a deposit of red selenium powder, if an alcohol swab could not remove this the sample was repolished and re-etched. Fine polishing was very critical for good results as the etch highlighted scratches that were not visible before etching.

5.3 Lead Experiments

5.3.1 Experimental Sequence.

The liquid metal bath was prepared by melting the alloy and then preheating it to about 5°C above the selected temperature.

The metal surface was cleared of dross, using a stainless steel scraper and then with zero power input the melt cooled at about 2°C per minute. The liquid was stirred vigorously by a hand held, motorised, rotary stirrer, as efficient mixing of the alloy is essential in view of the density difference of the two components. When the indicated millivolts corresponded to the chosen tempe rature, the experiment began by lowering the probe into the alloy and simultaneously starting the data logger. The probe rotated at constant speed in the liquid, with continuous monitoring of the four thermocouples, until it was raised at the end of the experiment.

5.3.2 Thermal Analysis

Thermal analysis of a small sample of tin-lead eutectic was carried out but pronounced undercooling made it useless, fig. (20), as a check of composition. It did however confirm the correctness of the dip thermocouple at the eutectic point.

5.3.3 Experimental Measurement

After cutting away the metal enveloping the stainless cap, the lead insert was unscrewed. The unbonded layers were carefully cut from the insert and the average thickness calculated from eight individual ball ended micrometer readings, at three different diameters.

The outside wall temperature, θw, of the lead insert was measured by embedding a small stainless sheathed thermocouple in a groove cut in the surface and covering the tip with solder.

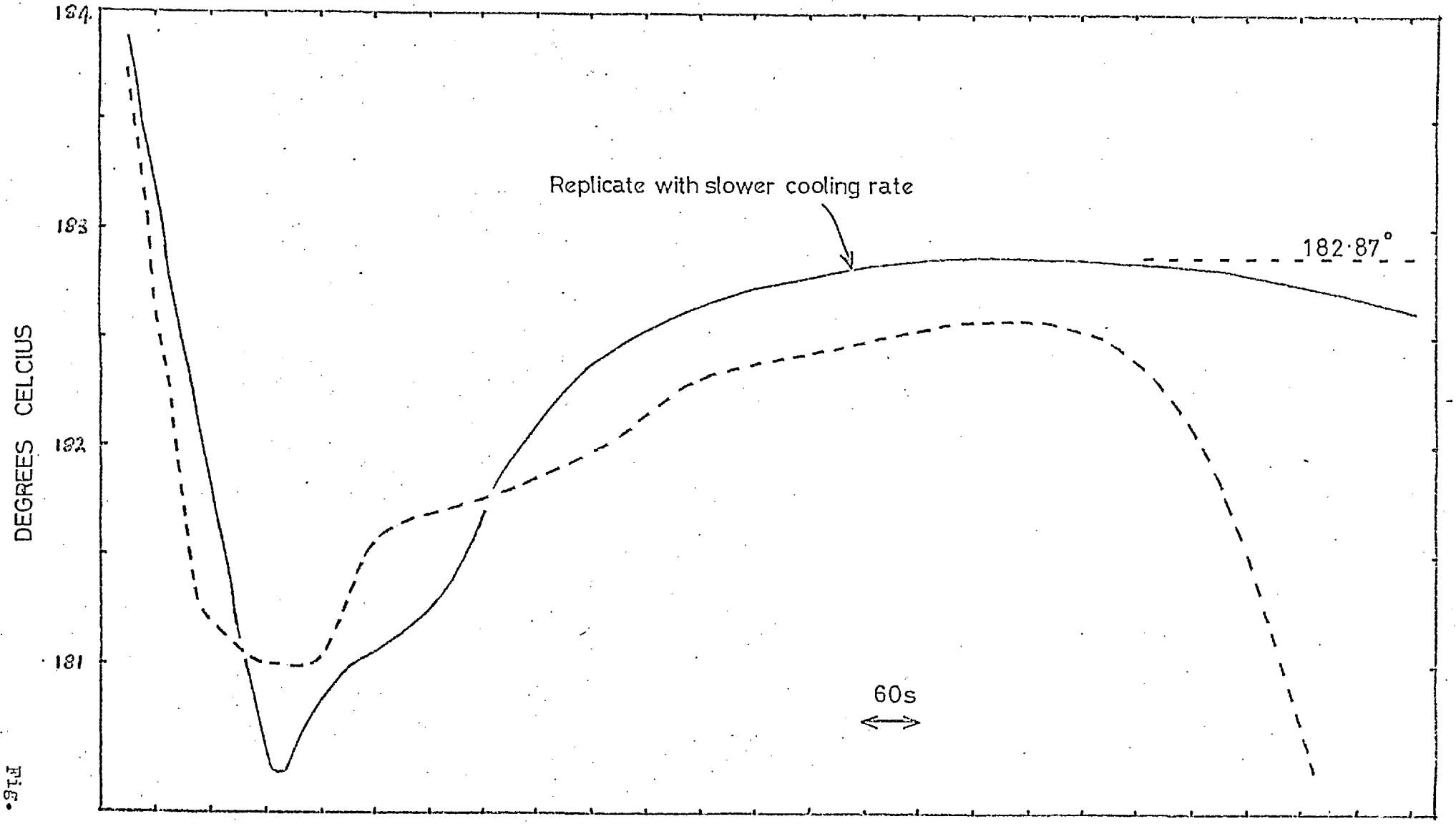


Fig. 20

Undercooling during Thermal Analysis of Eutectic Tin - Lead.

5.3.4 Preparation of Microstructures

The notorious problem of polishing pure lead has been solved by Clarke[60]. The use of his technique of prepared alumina papers prevented embedding particles, but as the correct vibratory polishing machine was not available manual polishing had to be used for the final preparation. Acceptable results were possible for the bulk of the lead but bevelling, despite double mounting, distorted the interface. Worst of all there was a compact row of diamond particles on the lead side of the interface, even 1/4 μm diamond obliterated detail.

6. RESULTS

6.1 Introduction to Presentation of Results.

The techniques used to produce a double sided clad ingot were not able to constantly form a bond between the stainless and mild steels, so the emphasis moved to solidifying metals around stainless steel.

Initially eutectic cast iron was solidified on to the cylindrical stainless steel probe at zero superheat. Interface heat transfer coefficients were estimated in these experiments by comparing the measured thickness of solidified metal and inner wall temperatures with the theoretical predictions.

In subsequent experiments, the time required for the complete removal of the chill layer, i.e. complete melt back, was determined at different superheats. In further experiments the melting process was allowed to continue for a little longer and the cooling air then blown through the centre of the probe. A bonded layer of eutectic iron was formed in this way on the outside of the probe.

A similar sequence was repeated with 3% cast iron and again with 1.4% steel, although it was not possible to bond layers of the steel to the probe. At first this was thought to be due to uneven melt back that was observed to occur, and the entire experimental sequence was repeated with a probe rotated throughout each experiment. This rotation eliminated the unevenness, but the stainless steel was attacked so rapidly that bonded steel layers could not be formed.

The sequence of no superheat, followed by superheat, was repeated with eutectic tin-lead solidifying on to both lead and stainless steel as the substrate, and finally the alloy was bonded to lead.

As the theory was not applicable to the solidification of non eutectic alloys no experiments were carried out at zero superheat for the determination of the interface heat transfer coefficient with the non eutectic alloys.

6.2 Double Sided Ingot Cladding

In general the amounts of bond between the stainless steel plates and the mild steel was small. Table (1) lists the selective areas of bonded plate, melted plate, and no bond for selected experiments. They are grouped in terms of temperature but no correlation can be found between the temperatures and the amount of bond.

Figure (21) represents the British Standard shear test (3740) and includes the results for test pieces cut from good areas of these ingots.

The electron probe traces across the interface of selected bonded areas, fig. (22),(23), demonstrates the inhibiting effect that nickel plating has on diffusion. The interface is reduced in thickness from 60 μm to about 8 μm.

6.3 Immersion of Static* Stainless Probes into Ferrous Alloys

6.3.1 Chill Layer Growth Eutectic Cast Iron

The results from selected individual experiments with eutectic cast iron at zero superheat, with zero power input are presented in figure (24), where measured thickness is compared with theoretical prediction. The chill layers did not bond to the stainless and were easily removed. The temperature readings of the inside wall obtained from these experiments are given in fig.(25), again with the predicted curve. In both cases an interface heat transfer coefficient of 2,500 $W/m^2\ ^oC$ gave good agreement with experimental values. The results from some other experiments were rejected because of uncertainty of either composition or temperature.

6.3.2 Chill Layer Growth and Melt Back

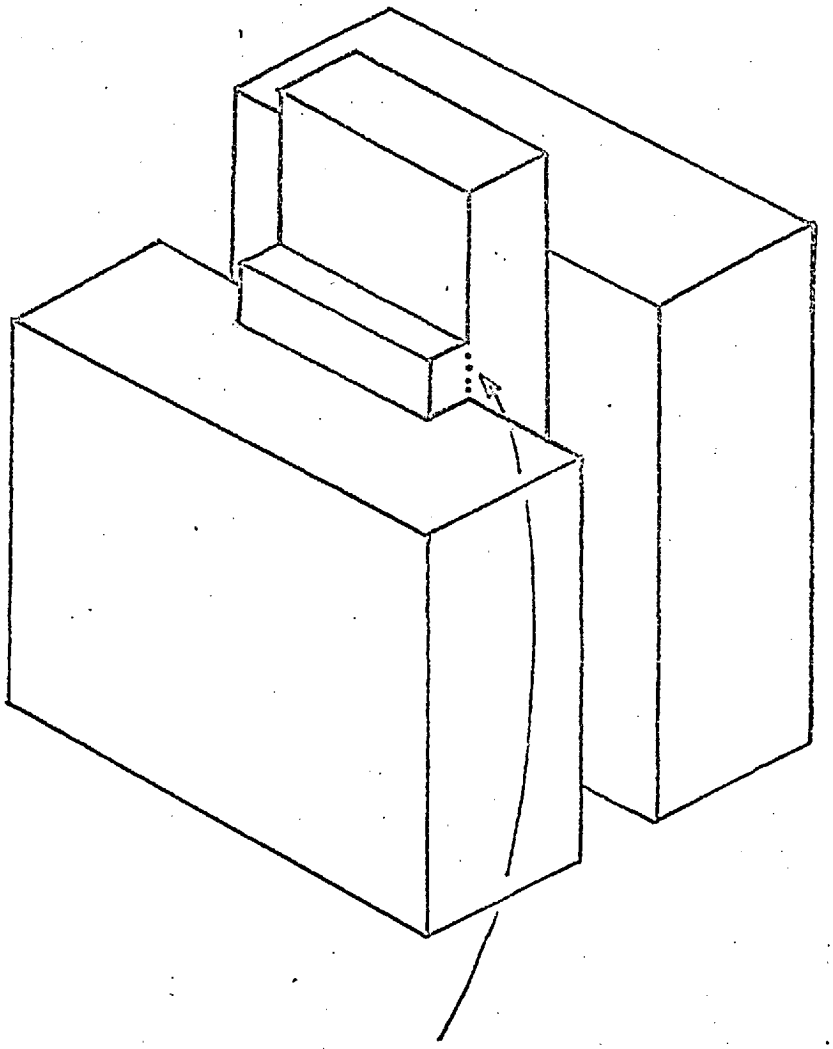
* Static refers to non rotation of the probes.

TABLE (1)

BOND AREAS - DOUBLE SIDED INGOT CLADDING

Plate Temp. °C	Melt Temp. °C	Bond Area %		Melt Area %		No Bond Area %		Average Bond %
433-465	1720	11	21	0	0	89	79	16
510-535	1675	11	0	0	0	89	100	6
513-542	1650	22	3	0	0	78	97	13
620-655	1600	0	0	100	100	0	0	0
585-603	1660	44	39	23	20	33	41	42
627-650	1720	35	9	45	56	20	35	22
645-675	1720	20	0	0	0	80	100	20
650	1720	13	19	0	1	87	80	16
680	1740	36	0	0	0	64	100	18
733-750	1720	0	0	90	90	10	10	0
725-770	1720	0	0	90	90	10	10	0
795-805	1750	32	10	59	3	9	87	21
795	1720	37	9	40	71	27	20	23
796-816	1710	42	28	32	48	26	24	35
760-808	1710	35	12	2	36	63	52	24
760-780	1705	27	27	0	17	73	56	27
750	1580	7	9	47	0	46	91	16
750	1537	12	39	0	0	88	61	25

Relative areas estimated after ultrasonic testing.



Tested under
Compression

Active Area of Test Piece 25·4 mm x 4·8 mm

Shear Test Results

1. 142 MN/m²
2. 181 MN/m²
3. 230 MN/m²
4. 297 MN/m²
5. 212 MN/m²
6. 181 MN/m²
7. 252 MN/m²

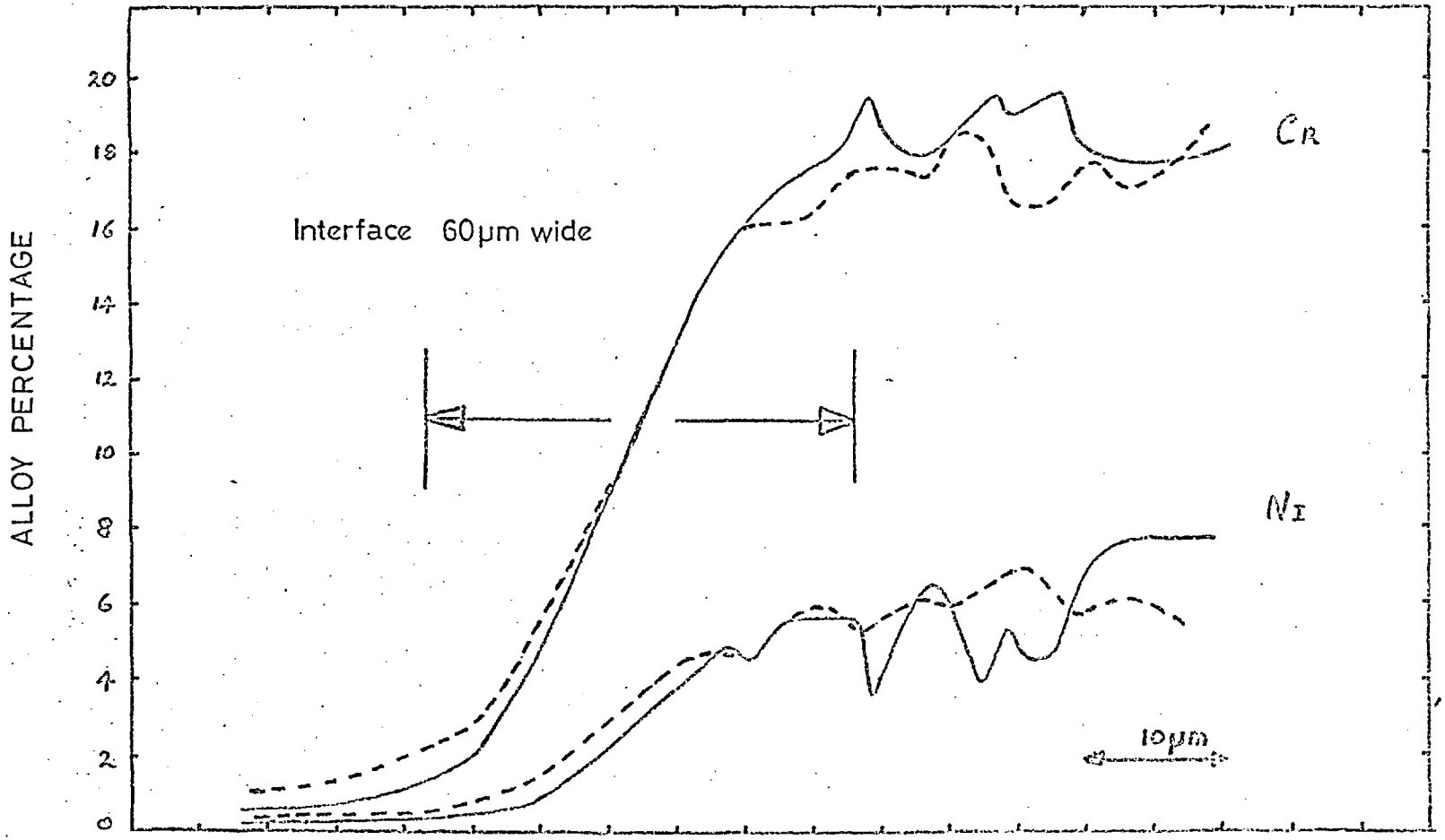
B.S. 3740

Minimum 10 t.s.i.

≡ 154 MN/m²

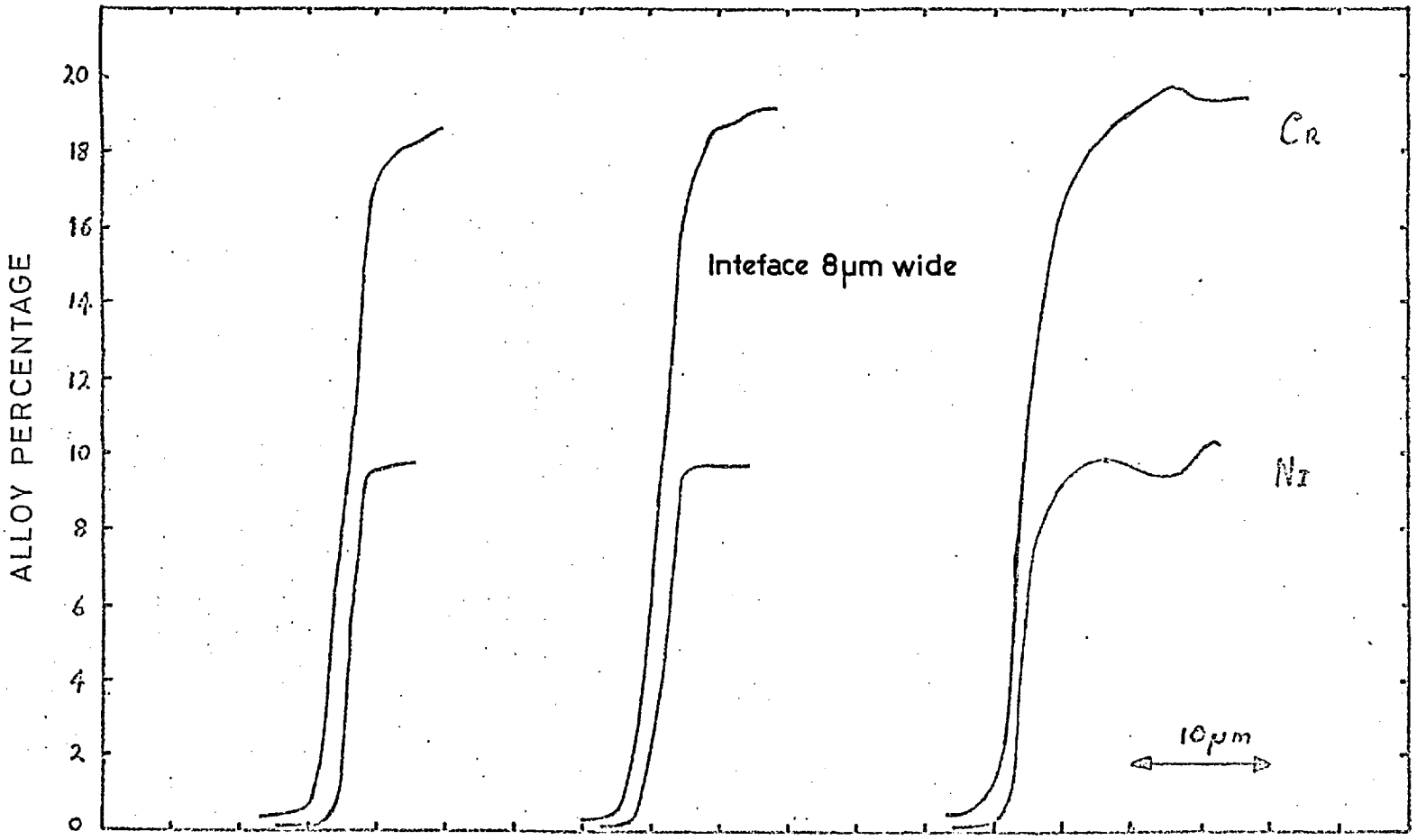
Bond Strength Shear Test and Results.

Fig. 21



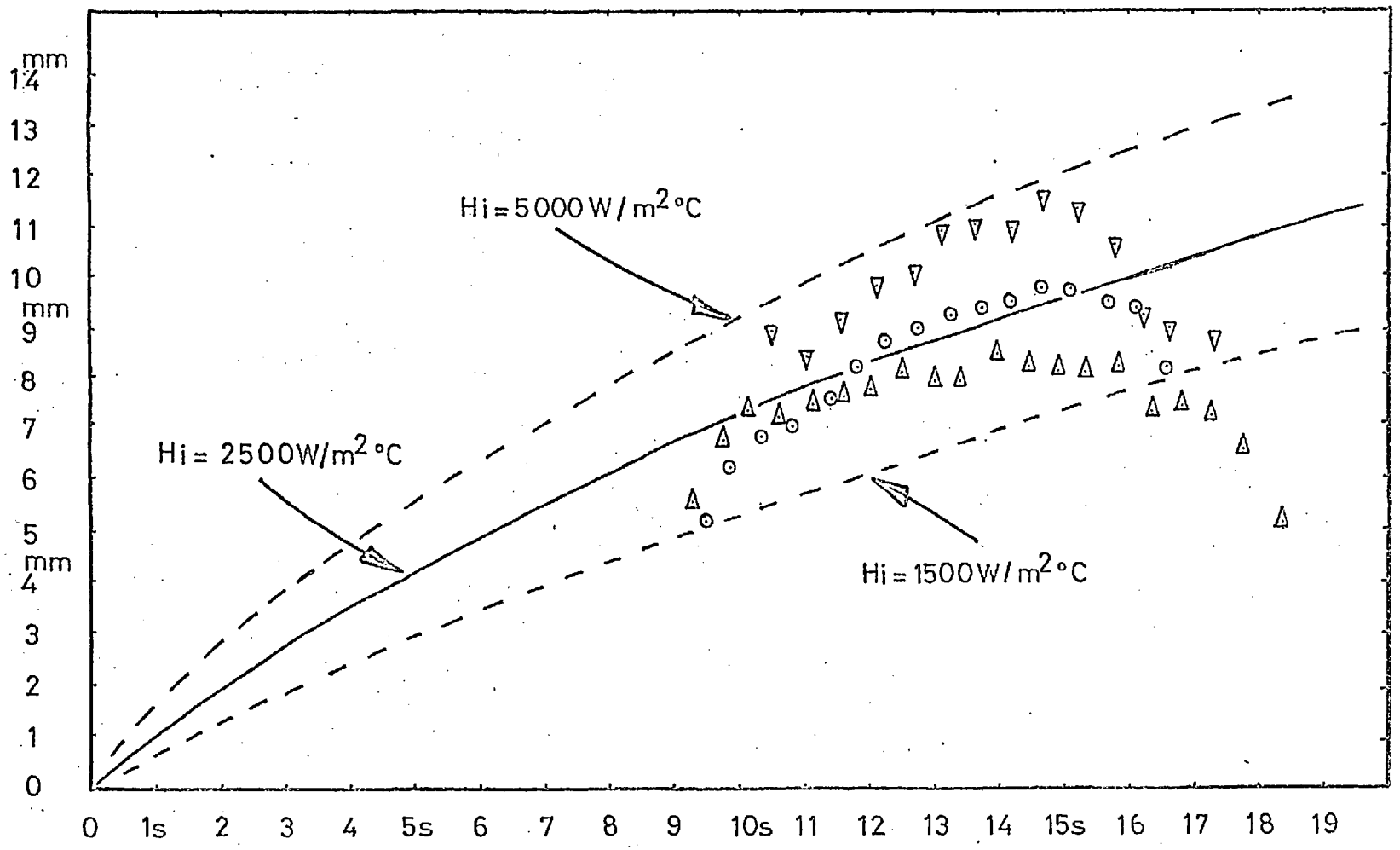
Chromium and Nickel Diffusion, for Two Stainless Clad Steel Specimen.

Fig. 22



Chromium and Nickel Diffusion, for Stainless Clad Speimen with Nickel Plating.

Fig. 23



Chill Layer Thickness vs. Exposure Time. Eutectic Cast Iron, Zero Superheat, Stainless Probe.

Fig. 24

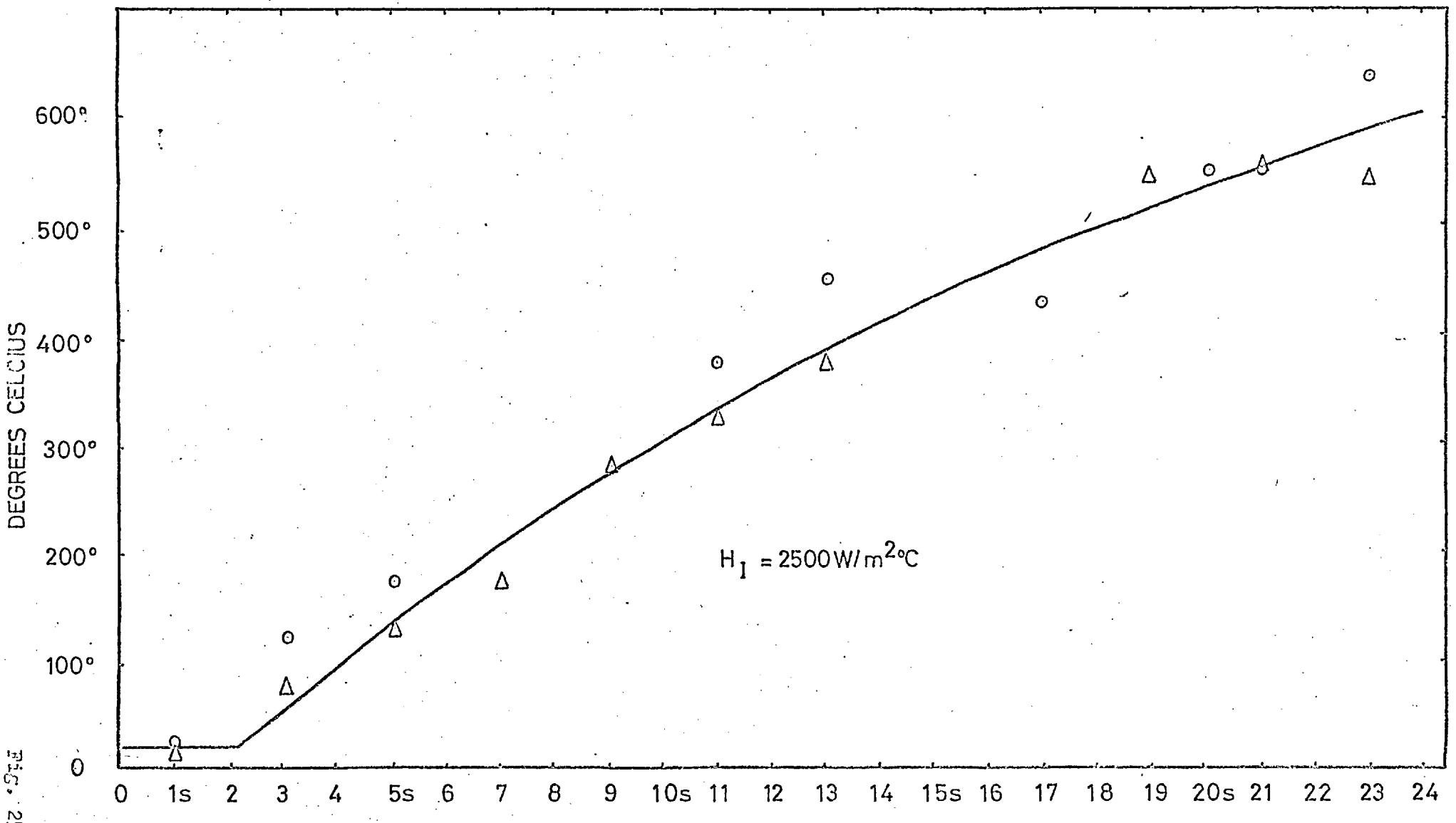


Fig. 25

Inside Wall Temperatures vs. Exposure Time. Eutectic Cast Iron, zero Superheat, Stainless Probe.

6.3.2.1 Eutectic Cast Iron at 50° Superheat

Melt back experiments were carried out with the furnace power preset at 30 kW, (16 kW was needed to keep the temperature constant) which gave the most suitable conditions for rapid removal of the chill layer. The maximum power of 40 kW could not normally be used as the furnace phase angle was very sensitive to changes in the mass of metal within the coil at high power.

Table (2) lists the conditions and average thickness for eleven separate experiments at 50°C of superheat. They show that 115s was insufficient time for the production of a uniformly clean stainless surface. The chill layer remaining after these experiments was less uniform than those at zero superheat, the irregularity being greater with thinner shells. On some probes there were several areas where the chill layer had melted away completely, adjacent to considerable thickness in other areas. In these cases an overall average thickness for the complete shell was calculated from the weight of each shell. These thicknesses are presented graphically in fig. (26). In addition results for two experiments without furnace power, set out for comparison, show the strong effect of the lack of power on the chill layer thickness. Fig.(27) presents corresponding temperature readings.

6.3.2.2 Eutectic Cast Iron at 90° Superheat.

Subsequent experiments at 90°C of superheat enabled complete melt back to be achieved in a more reasonable time. Table (3) gives the experimental conditions, showing the progress towards complete melt back. Fig.(28) presents the chill layer thickness plotted against

TABLE (2)

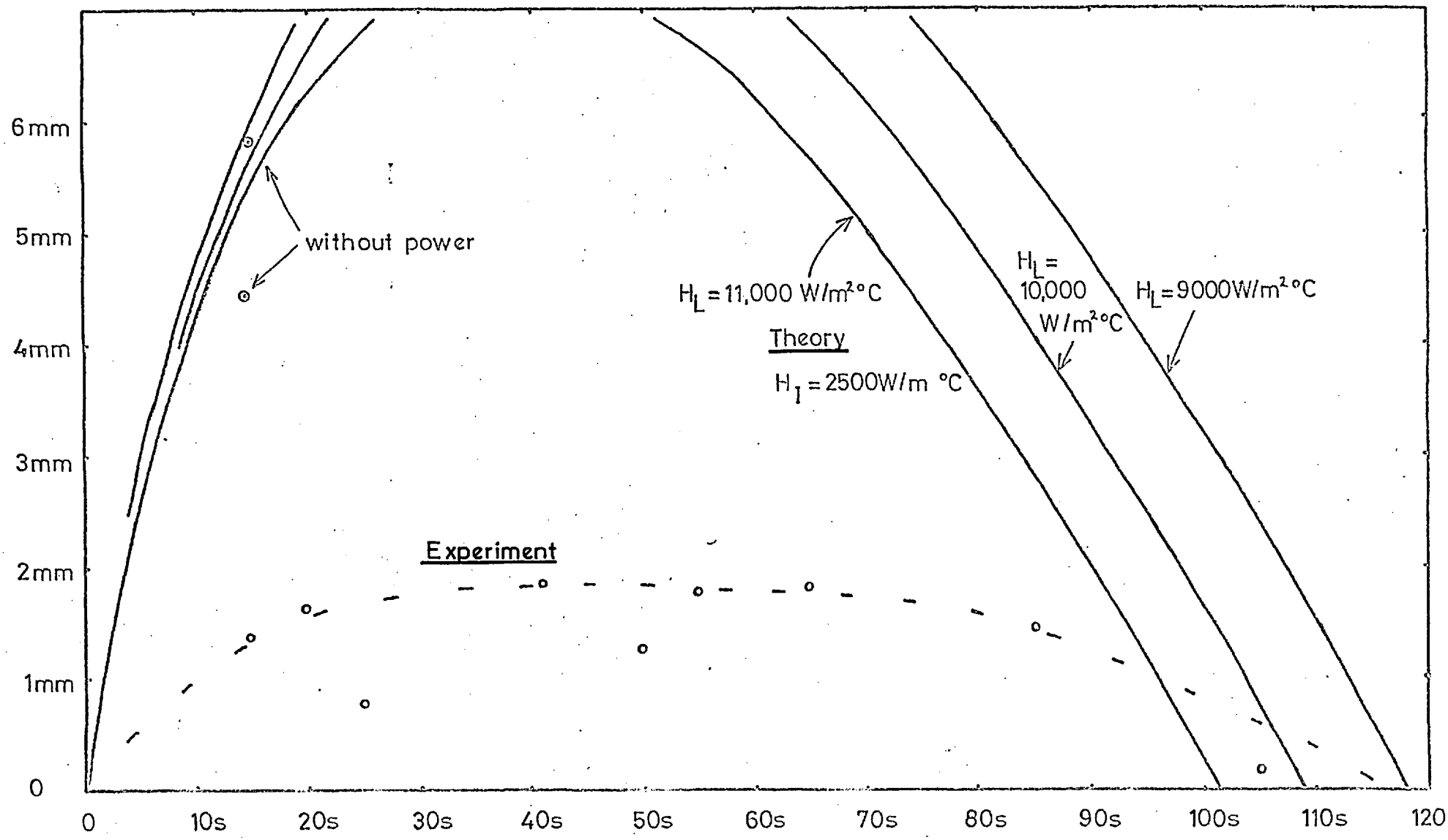
EXPERIMENTAL CONDITIONS AND AVERAGE THICKNESSES

EUTECTIC CAST IRON - 50°C SUPERHEAT

Temp.	Super-heat ø	Power	Static Exposure time	Average Exposure time	Weight of Shell *	Average thickness
°C	°C	kW	s	s	grams	mm
1203	58	30	10	15	347	1.37
1199	54	30	15	20	423	1.65
1185	50	30	20	25	170	.79
1185	50	30	36	41	430	1.86
1191	56	30	45	50	295	1.27
1193	57	30	50	55	414	1.80
1189	54	30	60	65	430	1.81
1188	57	30	80	85	339	1.47
1188	53	30	100	105	47	.20
1184	49	30	100	105	-	+ ve
1192	57	30	115	120	-	+ ve
1198	63	0	10	15	-	5.9
1192	57	0	10	15	-	4.5

* excluding the weight of the base piece.

ø above the measured arrest point.



Chill Layer Thickness vs. Exposure Time. Eutectic Cast Iron, 50°C Superheat, Stainless Probe.

Fig. 26

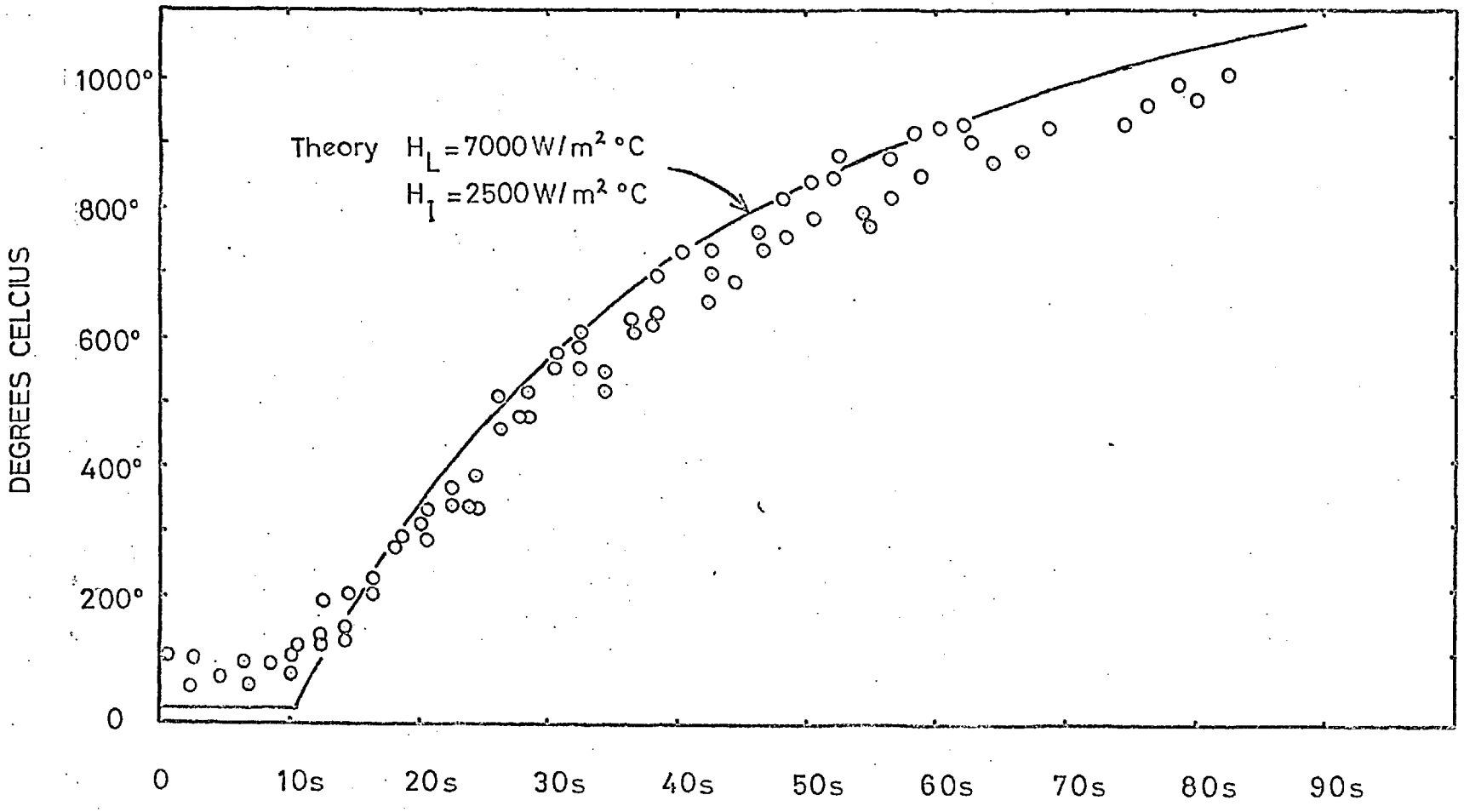


Fig. 27 Inside Wall Temperatures vs. Exposure Time. Eutectic Cast Iron, 50°C Superheat, Stainless Probe.

TABLE (3)

EXPERIMENTAL CONDITIONS AND AVERAGE THICKNESSES

EUTECTIC CAST IRON - 90° SUPERHEAT

Temp.	Super heat	Power	Static Exposure time	Average Exposure time	Weight of Shell	Average thickness
°C	°C	kW	s	s	grams	mm
1220	85	30	10	15	-	3.20 *
1208	73	30	35	40	520	2.18
1221	86	30	45	50	397	1.55
1226	91	30	50	55	186	.81
1221	86	30	60	65	221	.96
1227	92	30	80	85	+ ve	+ ve
1227	92	30	90	95	None	0.0
1231	96	16	10	15	-	5.4 *

* Average obtained from thickness measurements.

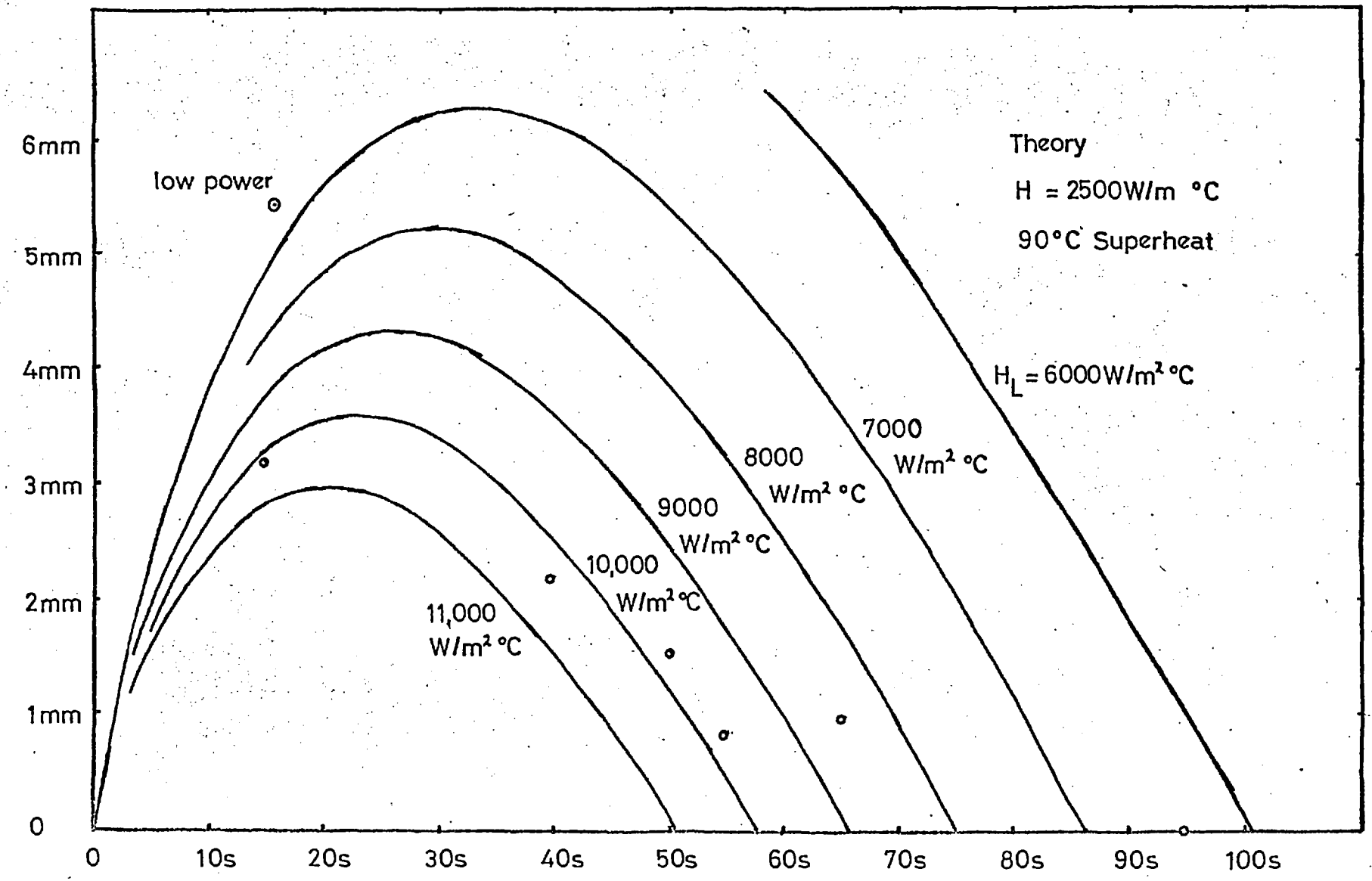


Fig. 28

Chill Layer Thickness vs. Exposure Time. Eutectic Cast Iron, 90°C Superheat, Stainless Probe.

exposure time and includes, as well as some theoretical predictions, one result at lower furnace power for comparison. The inside wall temperatures are similarly compared to these predictions, fig. (29). The reproduceability between experiments was good:- 90s static exposure at 90°C of superheat with eutectic cast iron and 30 kW. of preset furnace power, always produced a clean stainless steel surface.

The cast iron that solidified during these experiments exhibited an interesting structure. Close inspection of the shells in section showed that some of the iron had started solidifying white, yet a grey structure was formed at intervals. In every case the last metal to solidify was grey. A schematic drawing is shown in fig. (30).

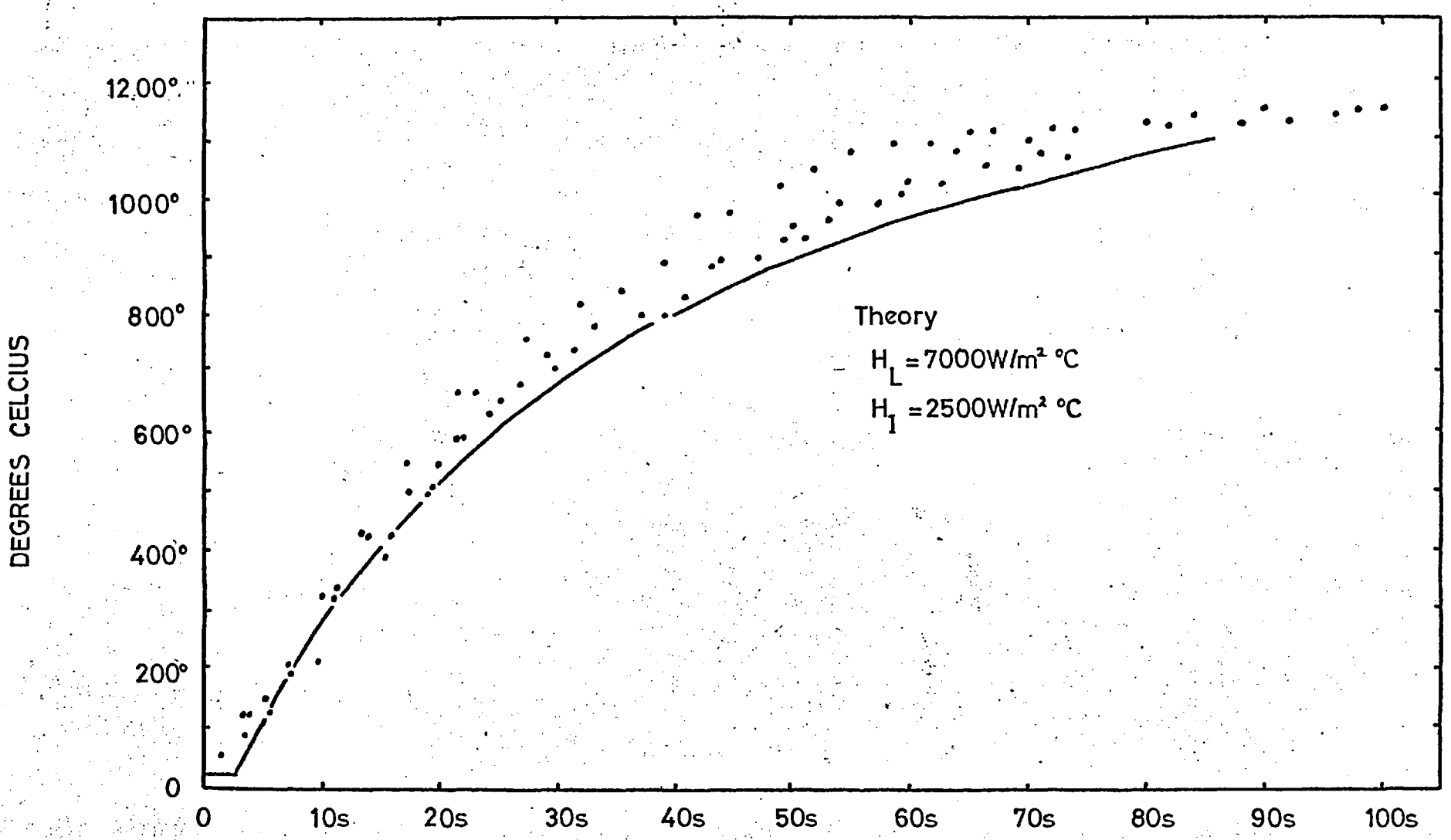
6.3.2.3 3% Cast Iron

The conditions required to produce a clean stainless steel surface were found in three experiments; the conditions are given in table (4).

Variations in heat transfer which caused problems later, were simply illustrated in the 2nd experiment. In this case the uneven chill layer enclosing the probe showed, on removal from the melt, a large variation in the outer surface temperature. The thin areas of the shell were bright red whilst the heavy regions were noticeably dark in comparison.

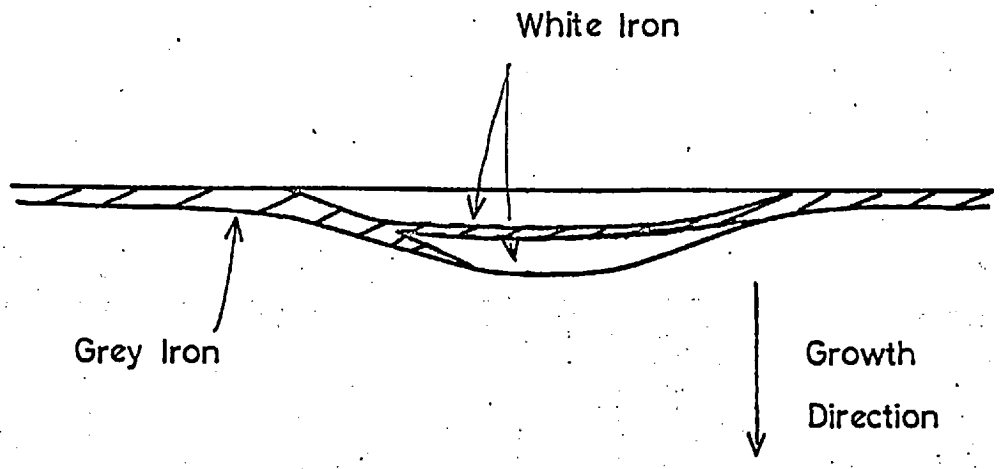
6.3.2.4 1.4% Steel

Experiments with a nominal 1.4% carbon steel were again carried out with the intention of producing a completely clean



Inside Wall Temperature vs. Exposure Time. Eutectic Cast Iron, 90°C Superheat, Stainless Probe.

Fig. 29



A Diagramatic Section of Eutectic Cast Iron Shell, showing grey and white bands.

Fig. 30

TABLE (4)

EXPERIMENTAL CONDITIONS AND QUALITATIVE RESULTS

3% CAST IRON

Temperature	Superheat	Power	Static Exposure time	Average Exposure time	
°C	°C	kW	s	s	
1360	60	30	40	45	Very heavy chill layer.
1361	60	30	60	65	Considerable amount of chill.
1370	70	30	90	95	No chill layer left.

stainless steel surface. The conditions are given in table (5) The initial experiments demonstrated that 150 sec. was insufficient for melt back at 50°C. of superheat. The third experiment boosted furnace power and required cooling air, (The power input swamped the additional loss of heat to the cooling air), but the complete chill layer was still present. Subsequent experiments used 90°C of superheat to speed up melt back. One such experiment with 90s static exposure emphasised the unevenness of the melt back process. Even though a high power input was used there was still some unremelted chill, despite severe melting of stainless steel regions that had been exposed.

Succeeding experiments involved preheating the stainless probe in a separate vertical tube furnace before immersing in the molten steel. This reduced the amount of chill formed and consequently the time for melt back. A limited amount of internal air cooling was used to reduce the inner wall temperature and inhibit the melting of the stainless wall. Four experiments, all concentrated near 40s exposure, established that the transition from remelting chill to melting stainless occurred at different times, in different positions, in different experiments and thus demonstrated that reproducible results could not be achieved.

The final experiment in this series used extreme conditions and endeavoured to produce even melt back. There was a measure of success but even though the melting was more uniform, the amount of solid stainless remaining was small. There was also insufficient cooling air in reserve to cause further solidification.

6.3.3 Bonding Experiments.

6.3.3.1 Eutectic Cast Iron

The solidification of metal onto the prepared stainless steel surface required more than internal air cooling. The progress towards the final technique for producing a

TABLE (5)

EXPERIMENTAL CONDITIONS & QUALITATIVE RESULTS - 1.4% STEEL.

Temp.	Super heat	Probe Preheat	Power	Static Exposure time	Air	
°C	°C	°C	kW	s	m^3/s	
1) 1448		-	30	40	-	large amount of chill, much more than with c.i.
2) 1471	50	-	30	60	-	less chill, partially bonded, still more than with c.i.
3) 1473	51	-	30 35 after 20s	150 total	7.10^{-3} after 60s	still complete chill layer, large amount.
4) 1515	90	-	30 39 after 30s	90 total	$6.5.10^{-3}$ after 45s.	stainless melted away on one side.
5) 1518	98	640 average	30	45 total	$6.5.10^{-3}$ after 20s	very uneven amount of chill, some stainless melted.
6) 1490	100	530	30	40 total	$6.5.10^{-3}$ after 20s	very uneven, some chill, adjacent to melted stainless
7) 1489	99	530	30	45 total	$6.5.10^{-3}$ after 20s	chill layer adjacent to deep melted depressions.
8) 1514	94	530	30	40 total	$6.5.10^{-3}$ after 20s	probe melted through completely in one area.
9) 1510	90	530	30 20 after 45s.	90 total	$3.2.10^{-2}$ after 18s	probe melted more evenly, no chill layer remaining.

satisfactory amount of bonded material is summarised in table (6) and the temperatures measured during the procedure are shown in fig. (31).

The microstructure of the bond is shown by fig. (32) where the gradual transition from a full grey iron structure to a plain stainless steel structure is seen across the interface.

The concentration profiles, fig. (33) from electron probe micro-analysis for Chromium and Nickel show the distance that the species diffused during bonding and cooling. The partial quantative analysis of five different phases presented in table (7) agree quite well with these traces.

6.3.3.2 3% Cast Iron

In this case 20s was allowed for dissolution of the stainless steel surface after melt back was complete. The temperatures measured are shown in fig. (34). Air cooling followed and the iron solidified after the furnace power was lowered, table (8). The metal solidified white and required a heavy slitting wheel on an automatic grinding machine for sectioning. The macrosections showed there was no bonding despite appreciable erosion during dissolution of the stainless steel.

6.4. Immersion of Rotating Probes into Lead Alloys

6.4.1 Chill Layer Growth

6.4.1.1 Lead Insert

The results from individual immersions of nine different lead inserts into eutectic tin lead were obtained under conditions of zero superheat, 68 r.p.m., with no furnace power. The chill layer produced during each experiment was easily cut from the insert, since there was no bonding. The thickness was then measured at three different circumferences. Two theoretical curves are presented, with

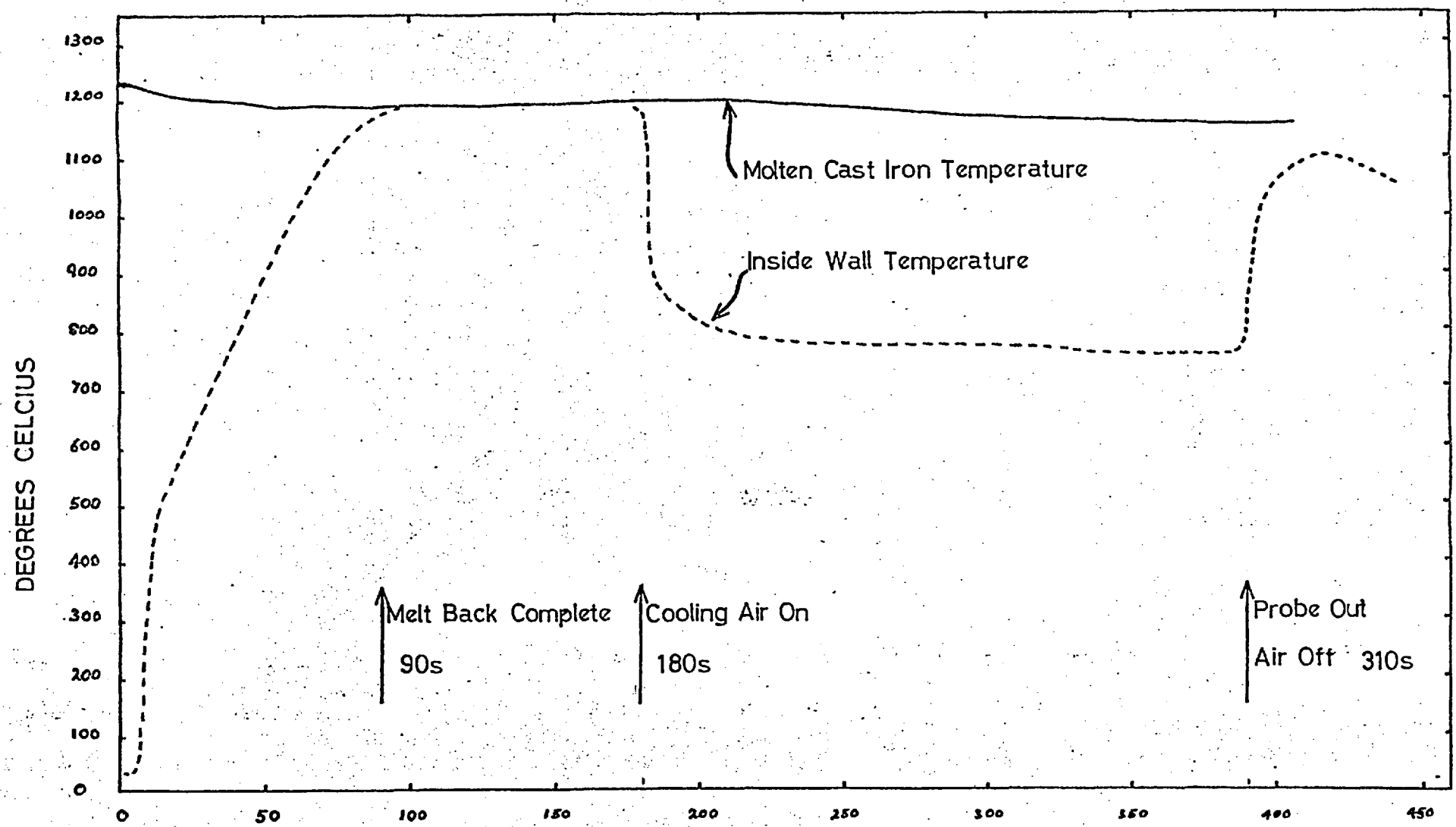
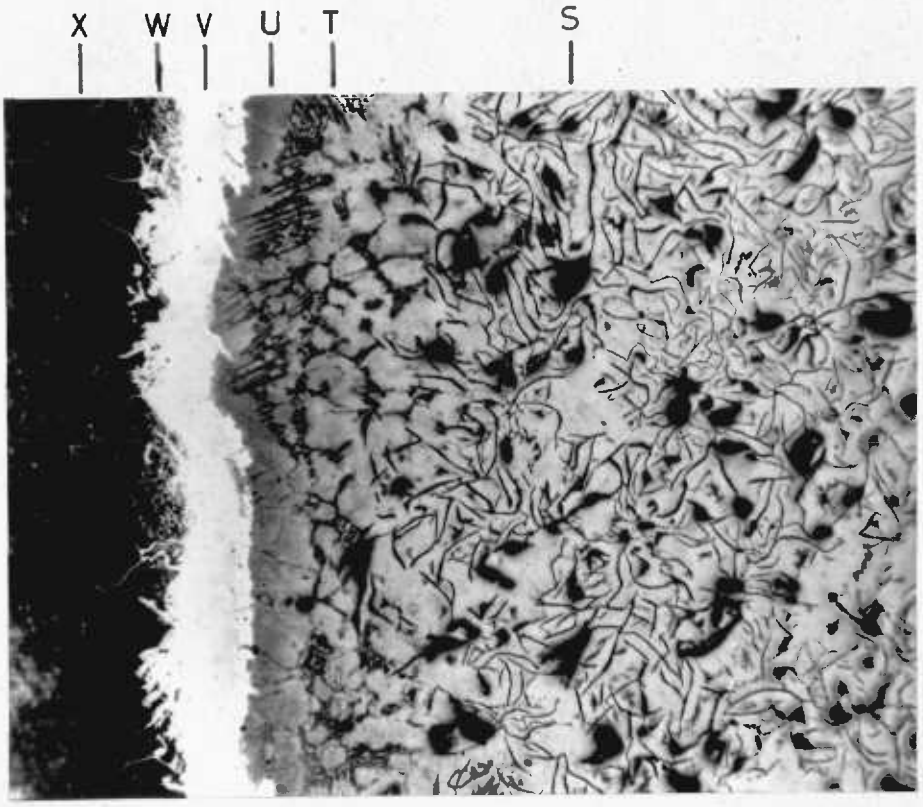


Fig. 31

Temperatures vs. Time for Eutectic Cast Iron Bonding Experiment.



X 240 ETCH: 10s in 2% NITAL
10 mins. in 'SELENIC ETCH'

MICROSTRUCTURE OF EUTECTIC CAST IRON BONDED TO STAINLESS STEEL WITHOUT ROTATION.

Fig. 32

TABLE (6)

EXPERIMENTAL CONDITIONS FOR EUTECTIC CAST IRON BONDING EXPERIMENTS

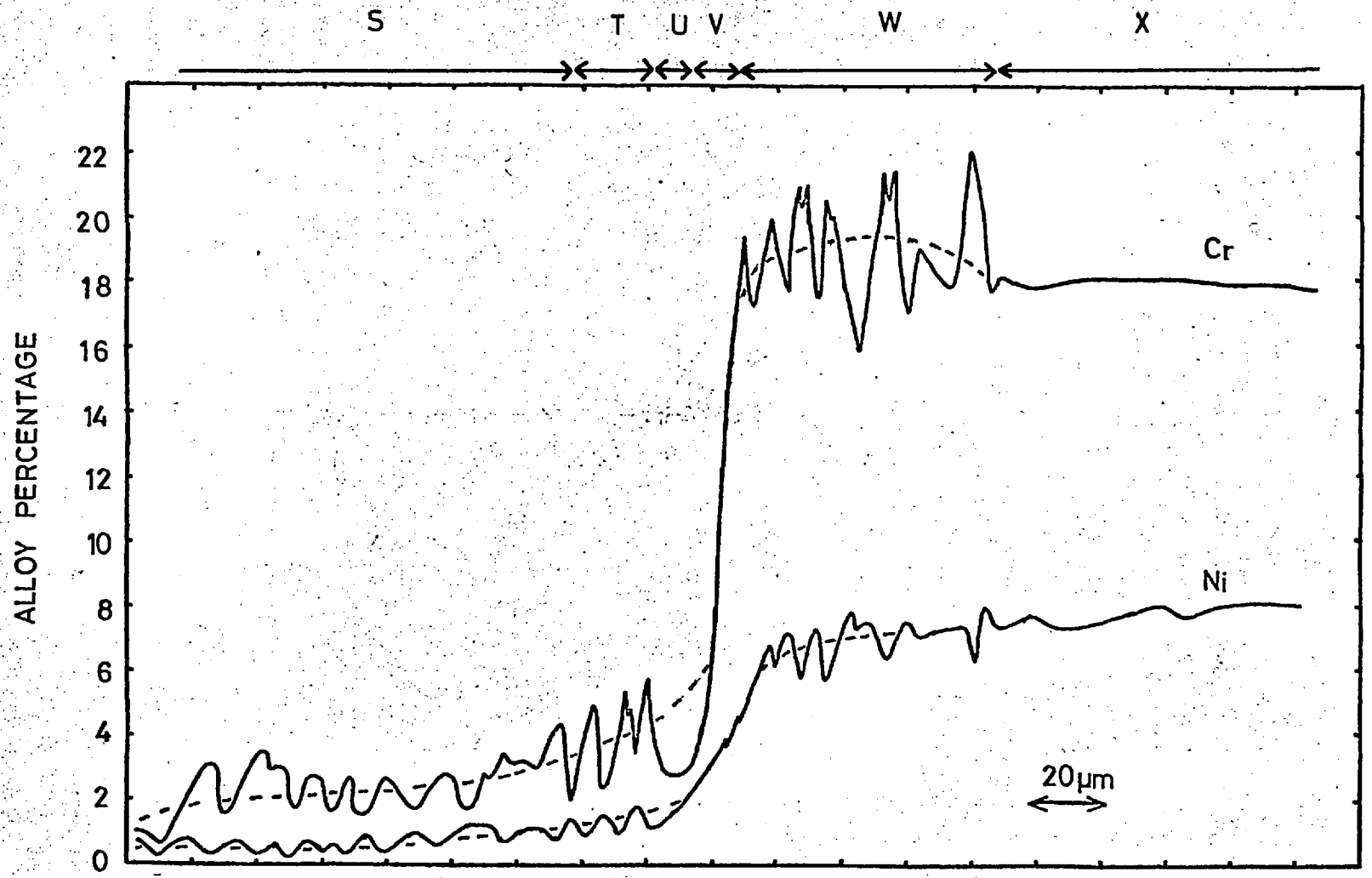
Initial Temperature	Initial Superheat	Furnace Power	Time to Melt Back	Time for Dissolution	Time for Air Cooling	Volume of Air	Comment
°C	°C	kW	s	s	s	m^3/s	
1125	90	30	90	*	270	$1.6.10^{-2}$	No Solidification
1125	90	30 10 kW after 105s	90	*	165	$2.6.10^{-2}$	A little solid metal. Some dissolution.
1125	90	30 10 kW after 105s	90	*	195	$3.4.10^{-2}$	Uniform bonded layer 10 mm thick.

TABLE (8)

EXPERIMENTAL CONDITIONS FOR 3% CAST IRON BONDING EXPERIMENT

1370	70	30 10 kW after 125s	90	20	130	$3.0.10^{-2}$	Uniform solidified layer.

* Whilst no time was deliberately allowed for dissolution, solidification did not occur immediately and some dissolution will have occurred.



Chromium and Nickel Diffusion for Stainless Clad Cast Iron.

No Probe Rotation.

Fig. 33

TABLE (7)

QUANTITATIVE ANALYSIS OF DIFFERENT PHASES IN A SPECIMEN BONDED WITHOUT ROTATION

	Chromium	Nickel	Silicon
T 'Dendrites'	4.4	.3	Low
T 'Matrix'	1.6	.8	High
U Intermediate Zone	3.2	3.0	Low
V Stainless Diffusion Zone	21.5	9.7	
W Stainless Disturbed Zone	21.8	11.9	

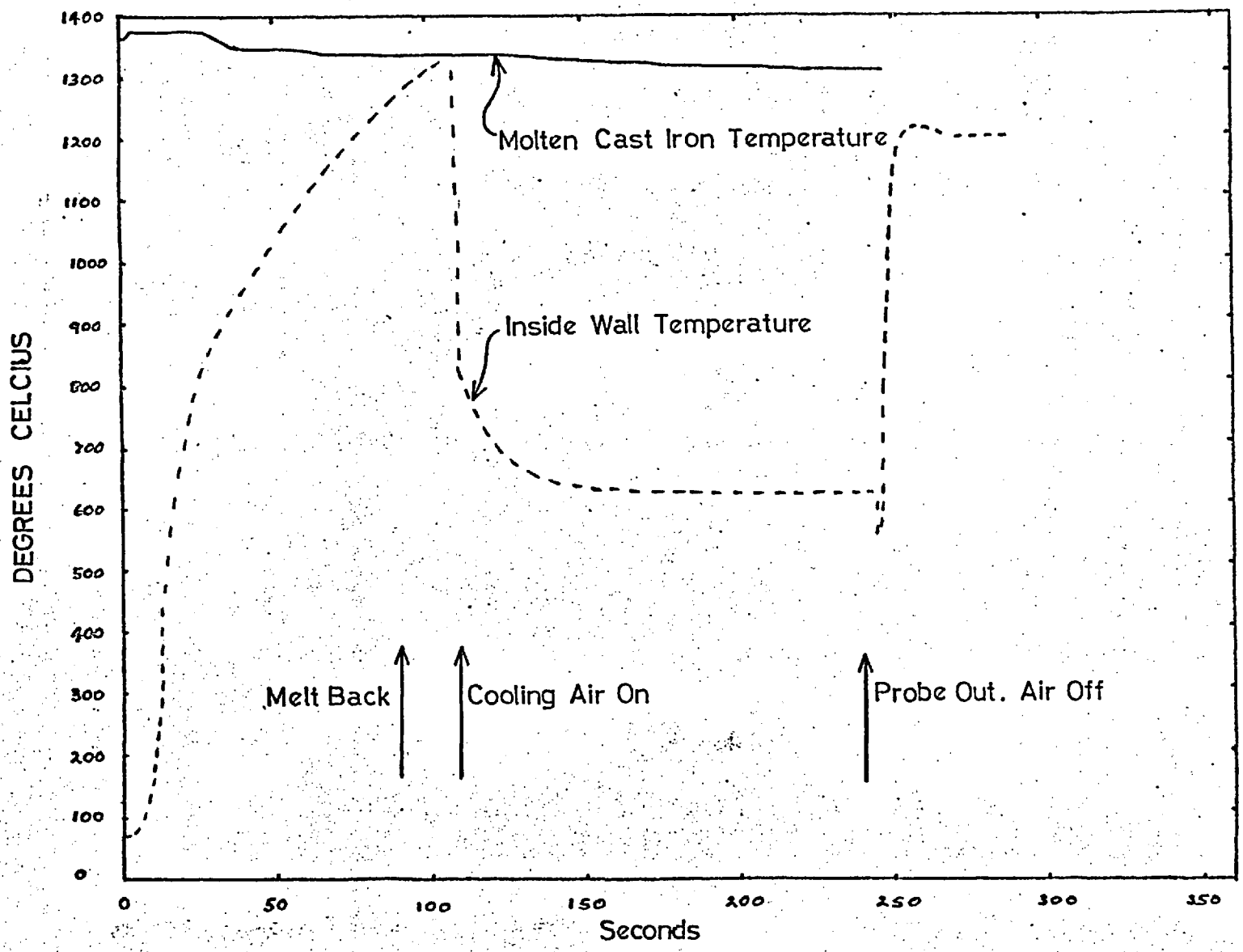


Fig. 34

Temperatures vs. Exposure Time during attempted Bonding of 3% Cast Iron.

these results fig. (35), the solid line was judged the best fit, corresponding to an interface heat transfer coefficient of 1500 $W/m^2\ ^oC$. The second dotted curve illustrates the effect of doubling this coefficient. The inside wall temperatures fig. (36) shows a similar trend with good agreement at low temperatures, but with higher exposure times the measured values fall below those predicted. All these measurements were consistent and reproduceable, the mean coefficient of variation of the thickness values being 3.36%

6.4.1.2 Stainless Probe

The solidification of tin-lead eutectics at zero superheat onto a stainless steel probe rotating at 68 r.p.m., and 200 r.p.m., again with no furnace power, produced anomolies. Fig. (37) presents the chill thickness from seven experiments and the theoretical curves which do not match the measured thickness except over a limited range. The solid layers appeared to be the result of a heavy spiral layer, superimposed upon a thin base layer. The best estimate for this interface coefficient is probably 2000 $W/m^2\ ^oC$.

The maximum thickness measured here is about 13 mm, nearly twice that for a lead insert, but the higher rotation speed depresses this value.

6.4.2 Chill Layer Growth and Melt Back

6.4.2.1 Lead Insert at 20^o Superheat and 68 r.p.m.

A heat balance calculation showed 20^oC of superheat would be sufficient for melt back. Table (9) summarises the thickness values obtained at this temperature and shows that the chill layer at the mid point of the insert was melted before that at the edge. Each experiment produced three average thicknesses and usually that corresponding to

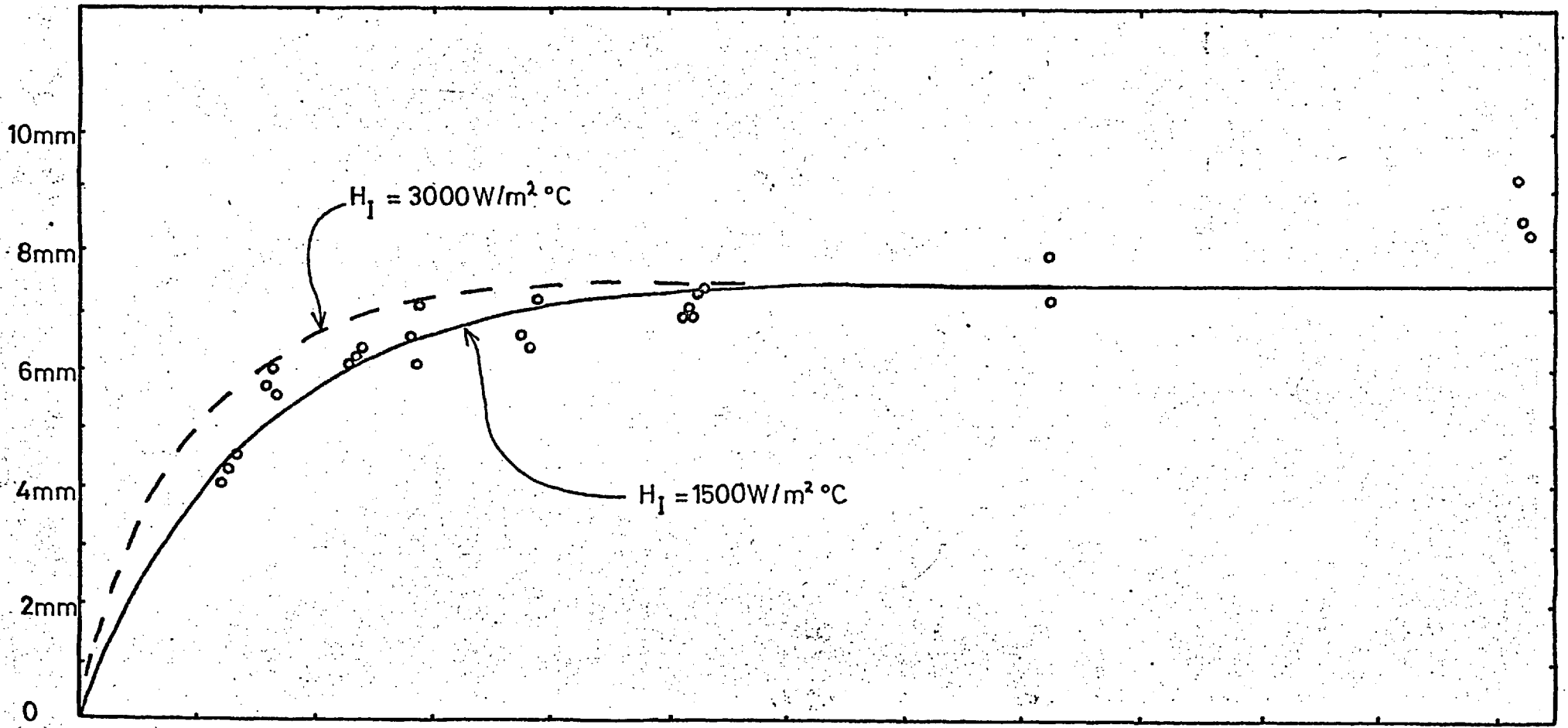


Fig. 35

Chill Layer Thickness vs. Exposure Time. Eutectic Sn-Pb, Zero Superheat, Pb Insert, 68 r.p.m..

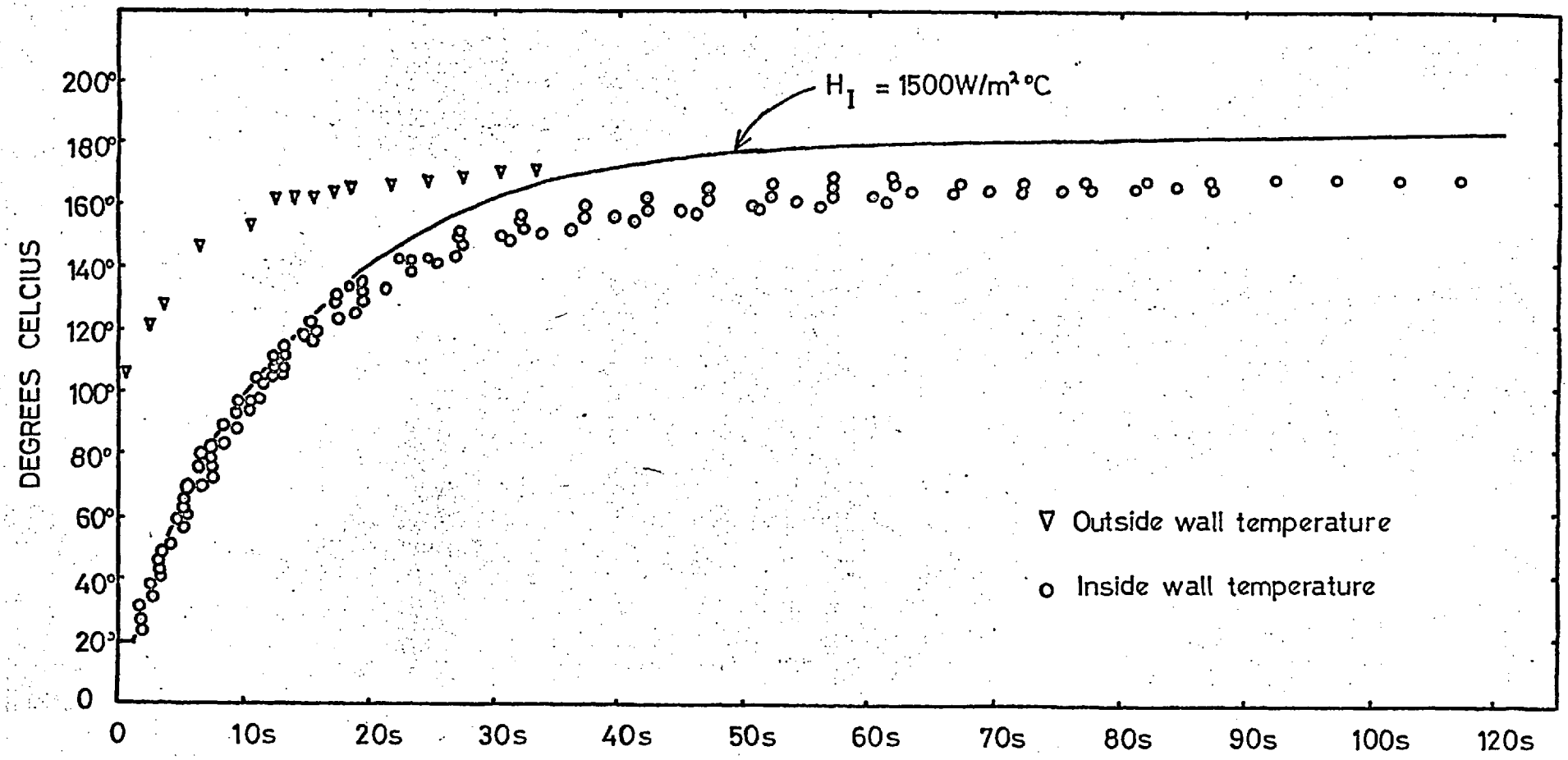


Fig. 36

Inside and Outside Wall Temperatures vs. Exposure Time. Eutectic Sn-Pb, Zero Superheat, Pb Insert, 68 r.p.m..

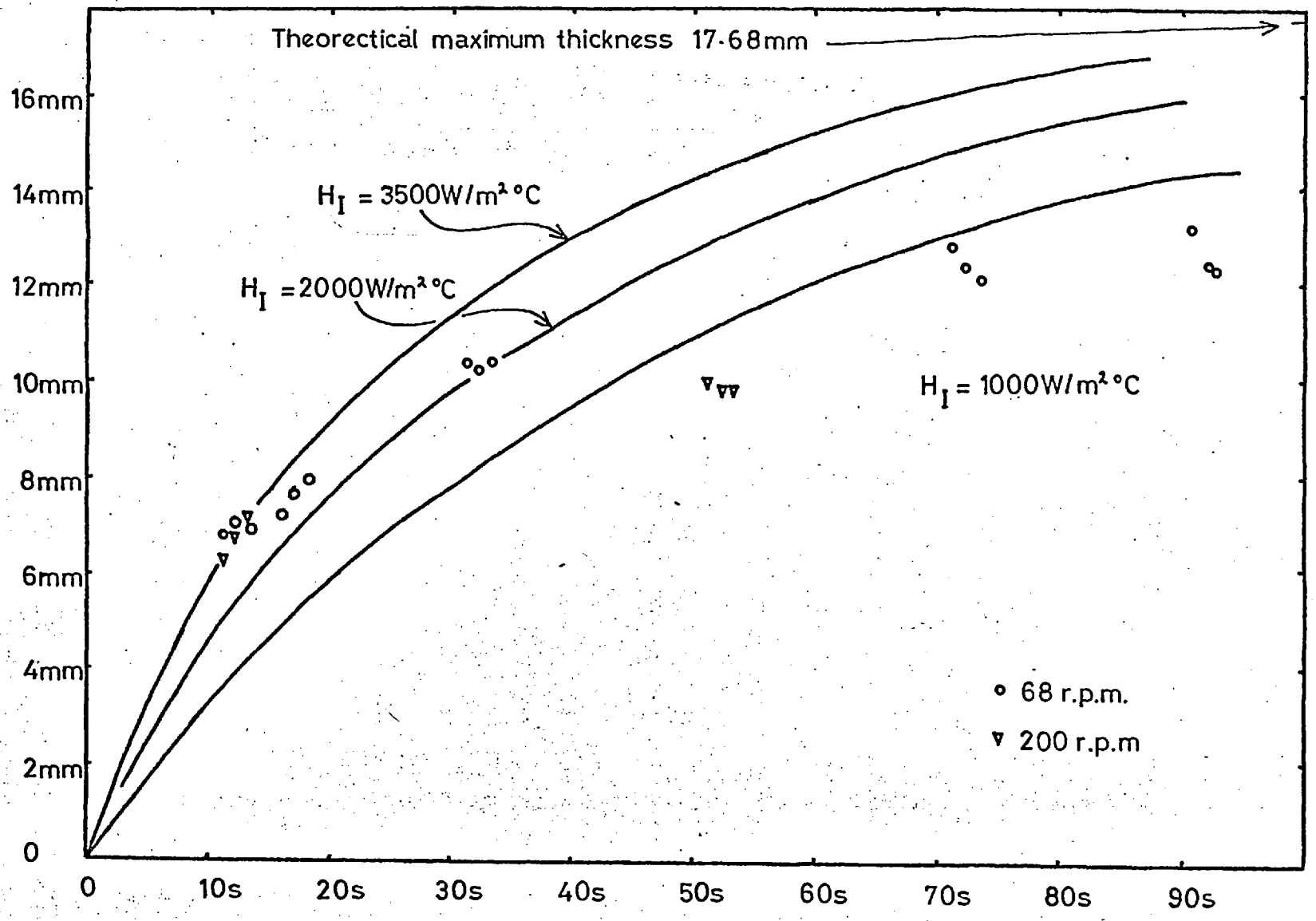


Fig. 37

Chill Layer Thickness vs. Exposure Time. Eutectic Sn-Pb, Zero Superheat, Stainless Probe.

T A B L E (9)

THICKNESS RESULTS, QUANTITATIVE. Sn-Pb at 20°C
SUPERHEAT on Pb INSERT, 68 r.p.m., ZERO POWER

Exposure time	Measured thickness		Comment
s	mm		
11.8	3.28		
12.3	3.15		
12.9	3.63		
12.2	2.74		
12.6	2.51		
13.1	2.18		
17.3	2.87		
17.9	2.62		
18.4	2.82		
22.2	3.20	2.95	
22.6	2.72	2.18	
23.1	2.97	2.79	
31.3	1.02		Clear patches appeared in midpoint of insert in spiral fashion.
31.8	1.19		
31.3	1.80		
32.3	1.78		Clear spiral patches.
32.9	1.70		
33.4	1.96		

T A B L E (10)

THICKNESS RESULTS QUALITATIVE

42.3	Insert mid point all clear.
52.3	Wider clear region in centre.
62.3	Insert clear except edges.
92.3	Insert completely clear.

the insert mid point was the lowest. Melt back was complete in the centre after 40s, but an additional 20s was needed to remove the chill from the edges of the insert in contact with the stainless.

Figures (38) (39) present the quantitative results with different computed predictions. The combination of H_I = 1500 W/m^2 °C (the value found before) and H_L = 5000 W/m^2 °C produces theoretical meltback at 42s, fig. (38), which coincides with the exposure time required to remove chill material at the mid point of the insert, but the curve falls below the actual values.

Table (10) presents qualitative results for longer exposure times when thickness measurements were no longer possible.

The second graph gives curves for a higher interface coefficient (3000 W/m^2 °C) and this follows the trend of the average thickness measurements quite well. An attempt to resolve this contradiction by measuring the outer wall temperature of the insert, θ_w, produced fig. (40). Even the higher theoretical interface coefficient fails to match the rapid change in the outer surface temperature. The lowest curve agrees very well with the inner wall temperatures. Fig. (41) presents the melt and inner temperatures on a different scale, initially the liquid temperature does not fall as predicted, and after about 15s the measured and predicted inner wall temperatures diverge.

6.4.2.2 Lead Insert at 20° Superheat and 200r.p.m.

The increase of rotational speed to 200 r.p.m. during four experiments dramatically reduced the time for melt back. Table (11) shows only 27s exposure was required; theoretical melt back of 25s is obtained with H_I = 1500, H_L = 7000 W/m^2°C. Fig. (42) shows two inserts that were immersed rotating into liquid tin lead at about 210°C for prolonged times. The surface dissolution is orientation dependent, similar to an etching reaction.

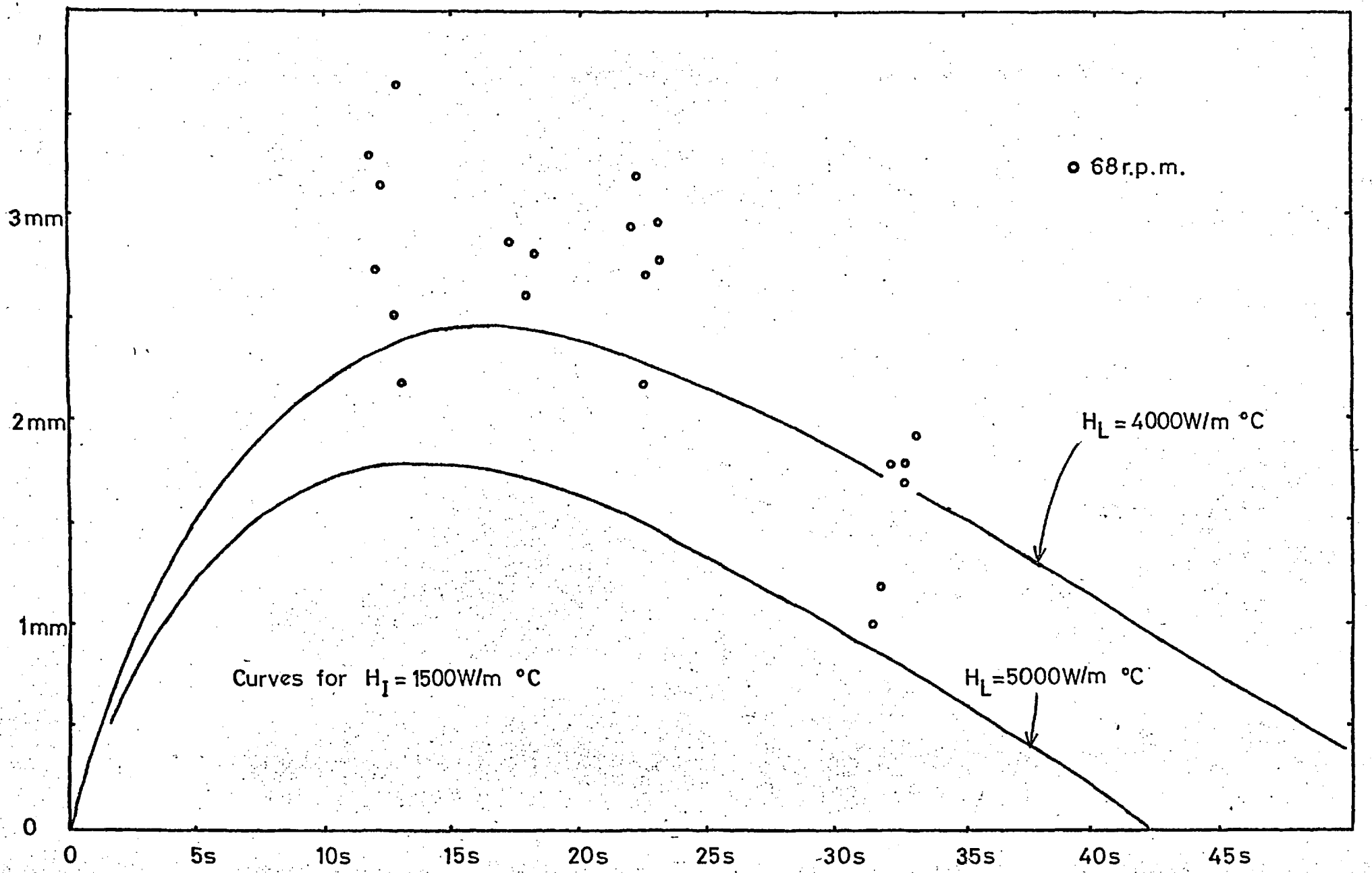


Fig. 38

Chill Layer Thickness vs. Exposure Time. Eutectic Sn-Pb, 20°C Superheat, Pb Insert.

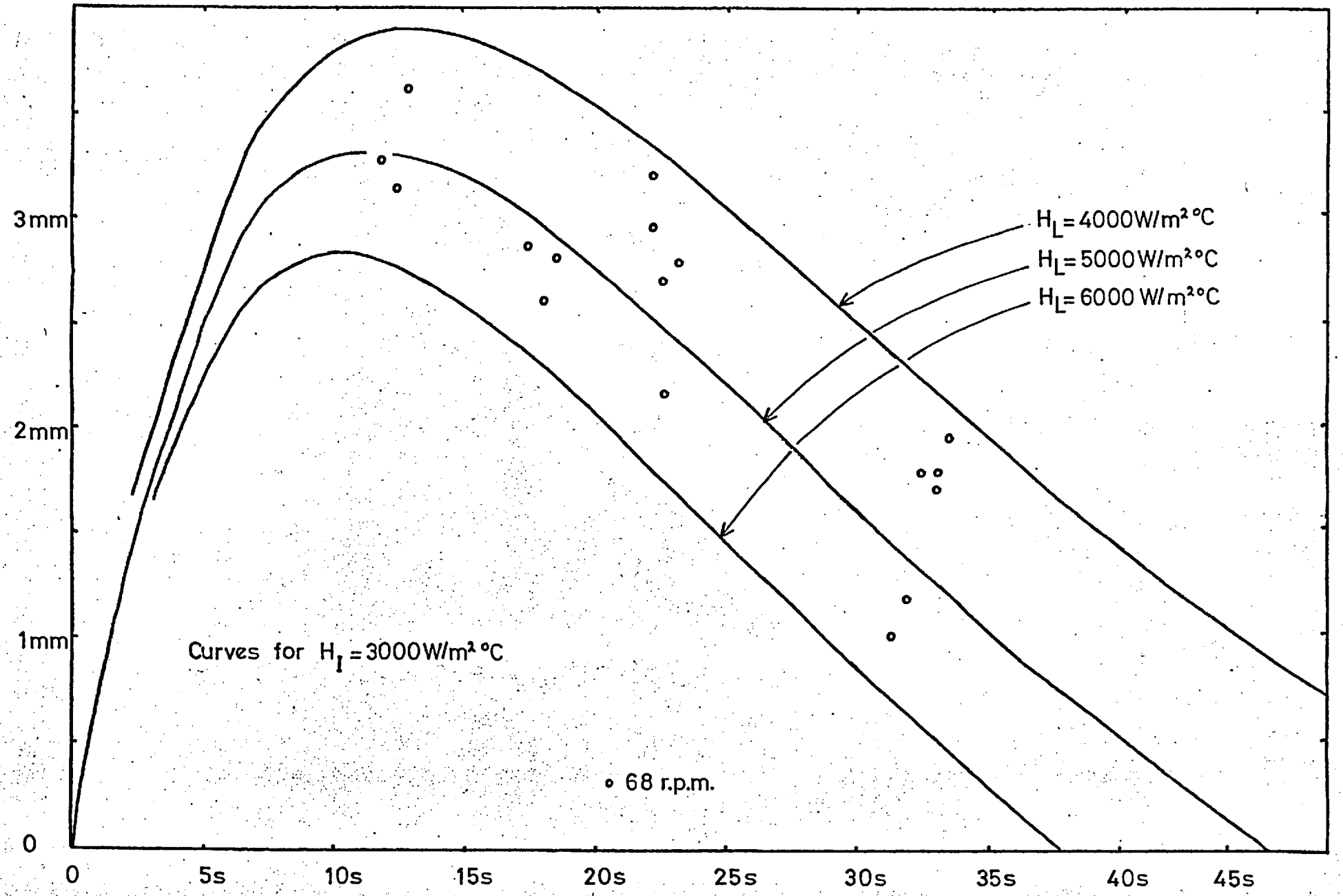


Fig. 39

Chill Layer Thickneness vs. Exposure Time. Eutectic Sn-Pb, 20°C Superheat, Pb Insert.

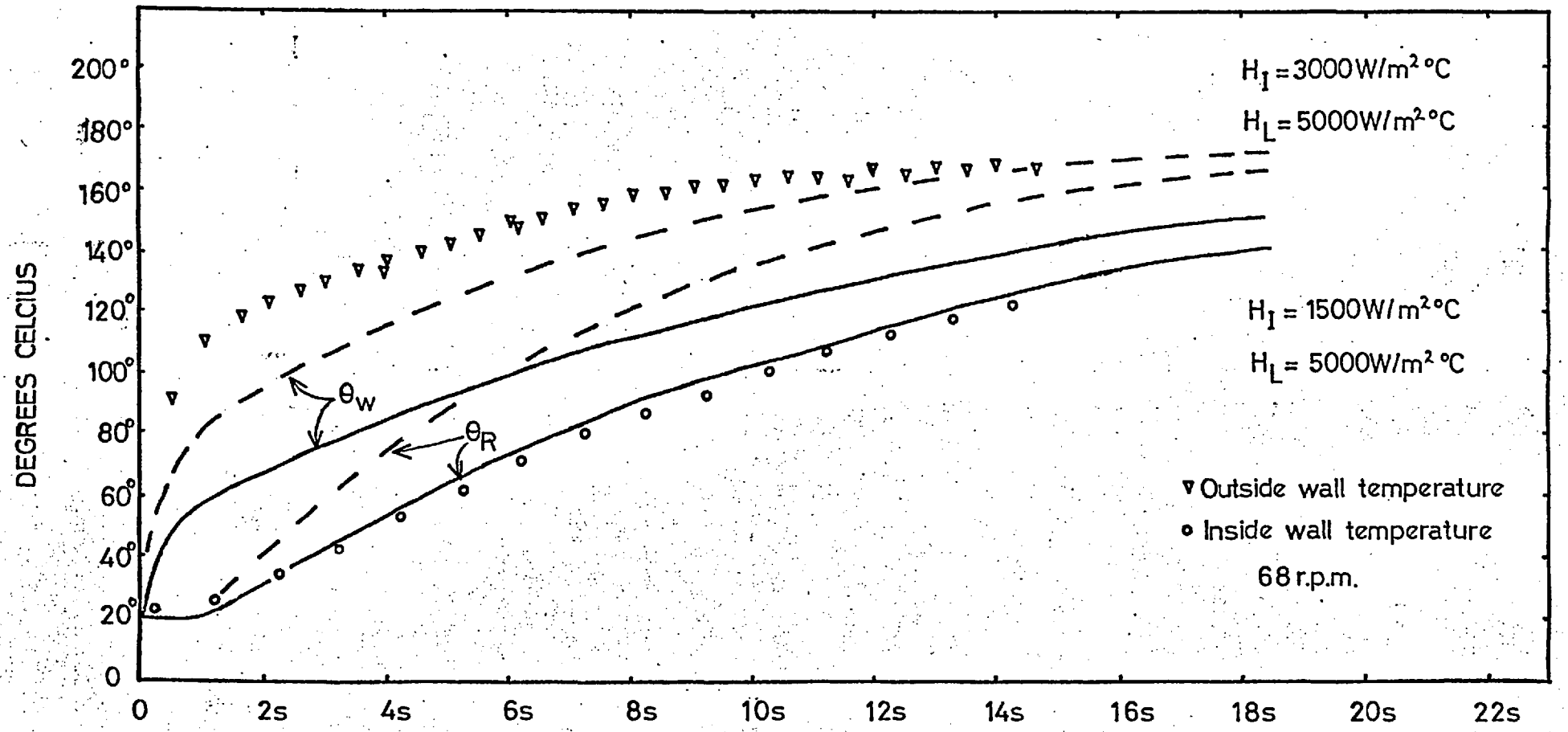


Fig. 40

Wall Temperatures vs. Exposure Time. Eutectic Sn-Pb, 20°C Superheat, Pb Insert.

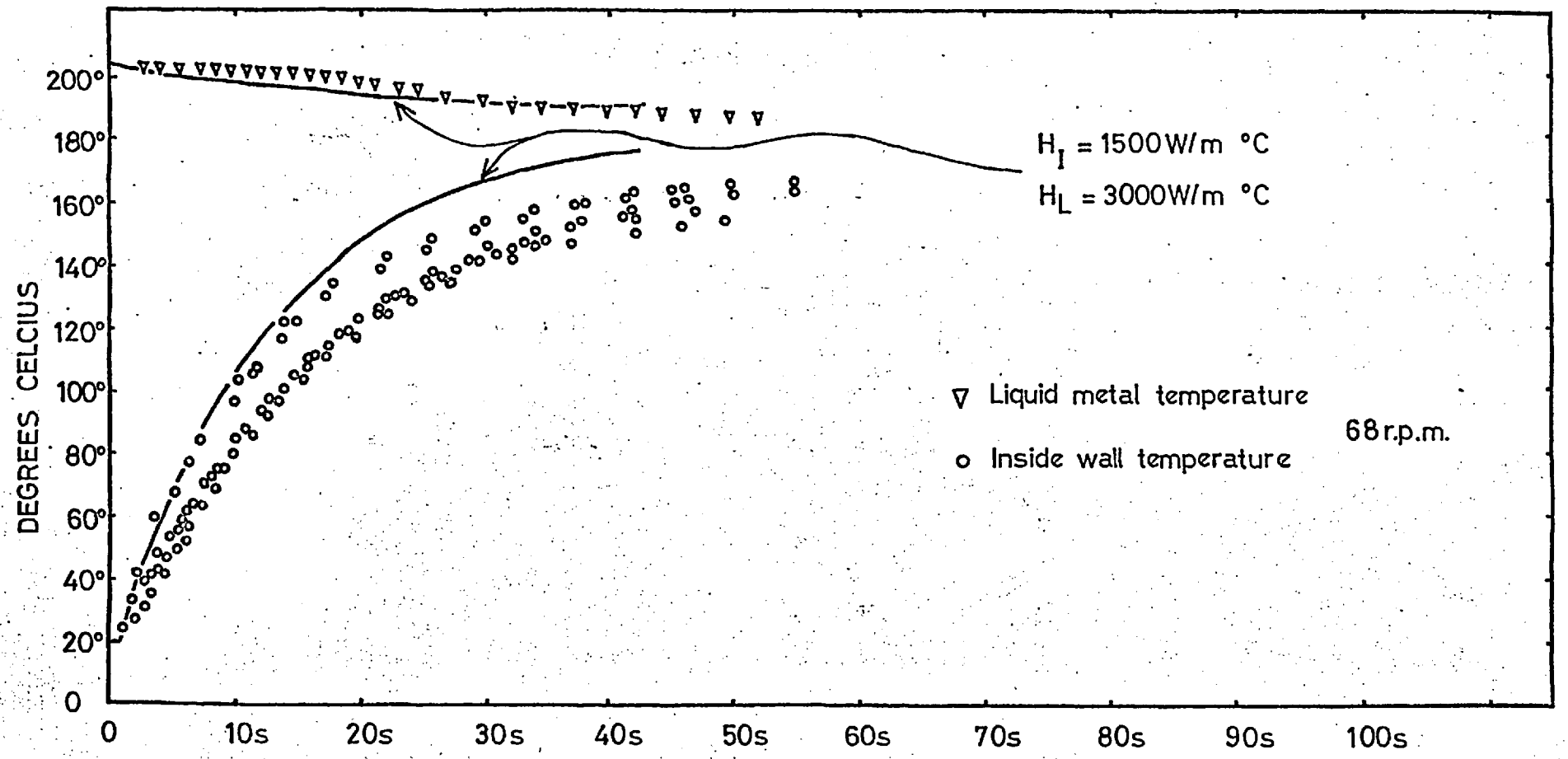


Fig. 41

Temperatures vs. Exposure Time. Eutectic Sn-Pb, 20°C Superheat, Pb Insert.

T A B L E (11)

THICKNESS RESULTS FOR Sn-Pb EUTECTIC ON Pb INSERT 20°C
SUPERHEAT 200 r.p.m., ZERO POWER

Exposure Time s	Measured Thickness mm	C o m m e n t s
12.16	4.24	
12.58	3.73	
13.1	2.29	
22.16	1.52	
22.58	.25	
27	-	Complete melt back on insert.
32	-	Complete melt back on insert.

T A B L E (12)

THICKNESS RESULTS FOR Sn-Pb EUTECTIC ON Pb INSERT 30°C
SUPERHEAT WITH 68 r.p.m., ZERO POWER

12	-	A few clear spiral pattern patches.
17	-	Insert mid point 2/3 clear
22	-	Complete melt back (twice)
32	-	Complete melt back.



SURFACE DISSOLUTION OF TWO LEAD INSERTS

Immersion in Sn-Pb at 30° Superheat
200 r.p.m.

Fig. 42

6.4.2.3 Lead Insert at 30° Superheat and 68 r.p.m.

As it was not possible to bond the materials with initially 20°C of superheat, subsequent experiments used 30° superheat to encourage bonding. Table (12) lists qualitative results from five such experiments showing that 20s static exposure produced complete melt back. Three extra experiments at 30°C of superheat demonstrated the critical importance of rotation speed. 20s exposure without rotation failed to produce melt back, 15s at probe rotation of 136 r.p.m. caused complete melt back and 10s at 200 r.p.m. also caused complete melt back. The conditions that just produced melt back are summarised in table (13).

6.4.2.4 Stainless Probe

Probe immersion at 30°C of superheat produced complete melt back in 45s and 30s with the probe rotating at 68 r.p.m. and 200 r.p.m. respectively. Fig. (43) presents the measured thickness plotted against real exposure time, and includes a theoretical curve. This curve was produced with similar liquid heat transfer coefficients to those used before (sects. 4.2.1, 4.2.2) and did not show melt back, as there was insufficient superheat. However certain conditions such as $H_I = 2000$, $H_L = 9000$ W/m^2 °C produce zero thickness in less than 10s. The second solid curve is a similar borderline case, with thickness remaining below .6 mm for nearly 10s.

6.4.3 Bonding Experiments. Lead Insert

Table (14) lists the experimental conditions during the seven bonding experiments. In the first experiment an additional thermocouple was suspended in the liquid close to the rotating probe surface. This thermocouple showed that the liquid close to the probe cools initially much more quickly than the liquid around the remote sensor. (fig 44) The theoretical melt back prediction for the bulk liquid temperature falls in between these two measured temperatures. Experiments that started with 20°C of superheat and gave 20s

T A B L E (13)

EXPERIMENTAL CONDITIONS THAT JUST PRODUCE MELT BACK
Sn - Pb - Pb

At Mid Point	On All Insert.
20°C 40s 68 r.p.m.	20°C 60s 68 r.p.m. 20° C 25s 200 r.p.m.
30°C 17s 68 r.p.m.	30°C 20s 68 r.p.m. 30°C 10s 200 r.p.m.

On average add 2s for real exposure time.

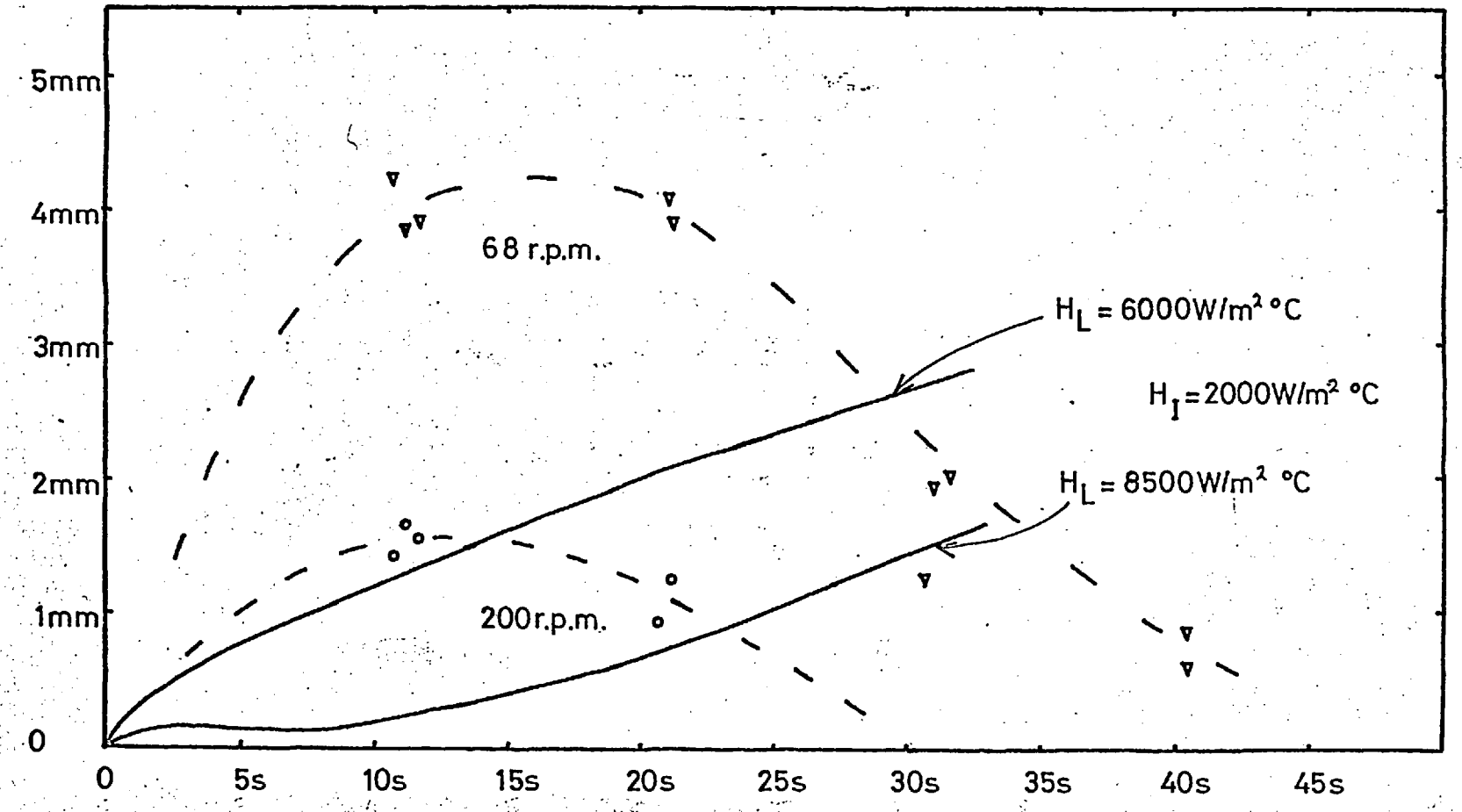


Fig. 43

Chill Layer Thickness vs. Exposure Time. Eutectic Sn-Pb, 30°C Superheat, Stainless Probe.

TABLE (14)

EXPERIMENTAL CONDITIONS FOR BONDING EXPERIMENTS, Sn-Pb EUTECTIC ONTO Pb INSERTS - 68 r.p.m. ZERO POWER

	Original Temperature	Original Superheat	Time to Melt Back	Time for Dissolution	Time for Air	Volume of air	Comment
	^{o}C	^{o}C	s*	s	s	m^3/s	
1	203	20	60	0	95	$1.4.10^{-2}$	No Bond.
2	203	20	60	0	95	$1.4.10^{-2}$	Surface Prepn.** No Bond.
3	213	30	20	10	90	$2.6.10^{-2}$	No Bond
4	213	30	20	20	80	$1.4.10^{-2}$	Insufficient solid metal.
5	213	30	20	20	200	$1.4.10^{-2}$	Bond O.K.
6	213	30	20	20	140	$2.3.10^{-2}$	Bond O.K.
7	213	30	20	20	110	$3.2.10^{-2}$	Bond O.K.

* Static exposure times.

** 400 # and 600 # SiC. paper + Carbon Tetrachloride.

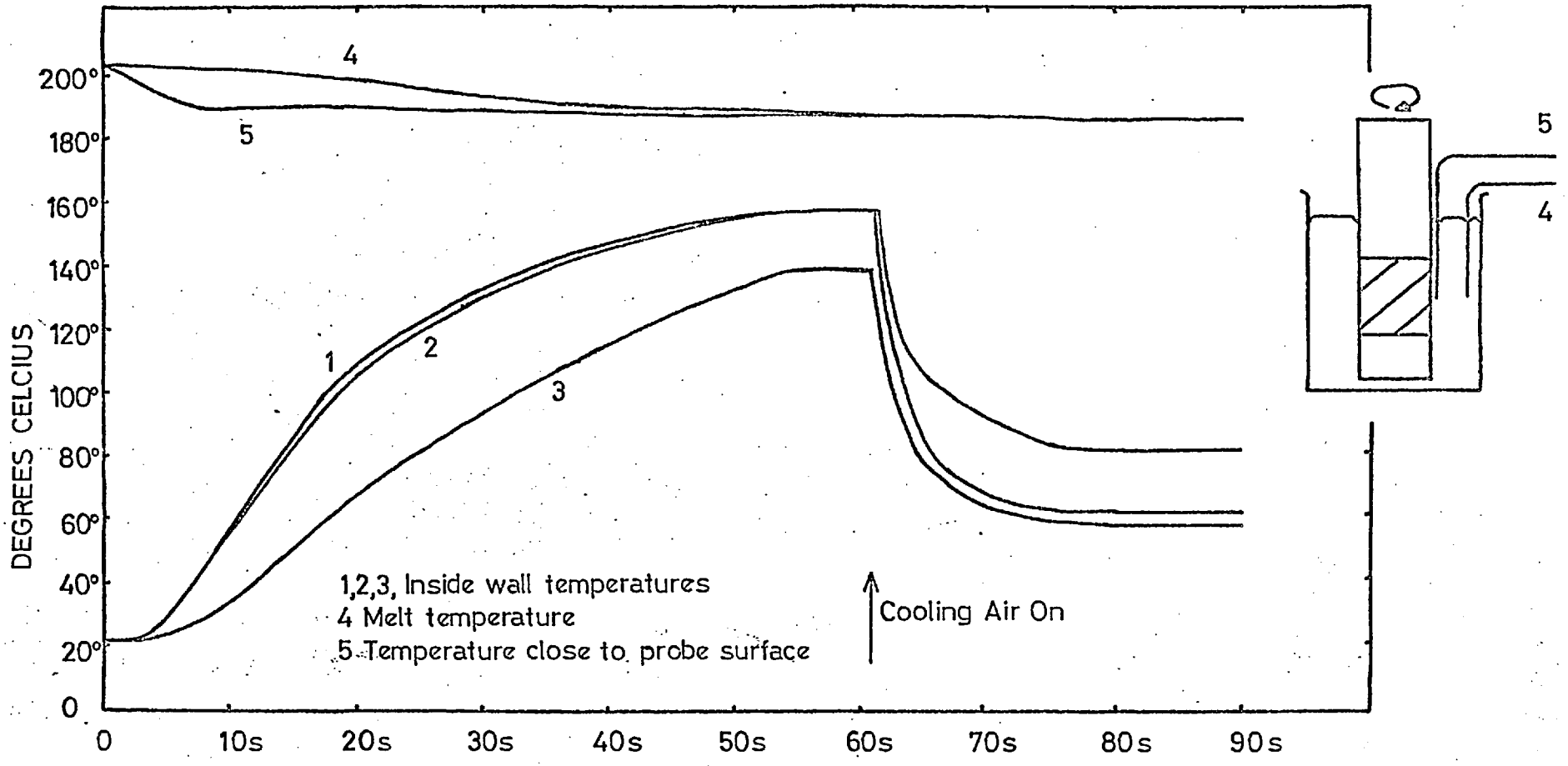


Fig. 44

Temperatures vs. Exposure Time. Eutectic Sn-Pb on Pb Insert Bonding Experiment, No1 Table 14.

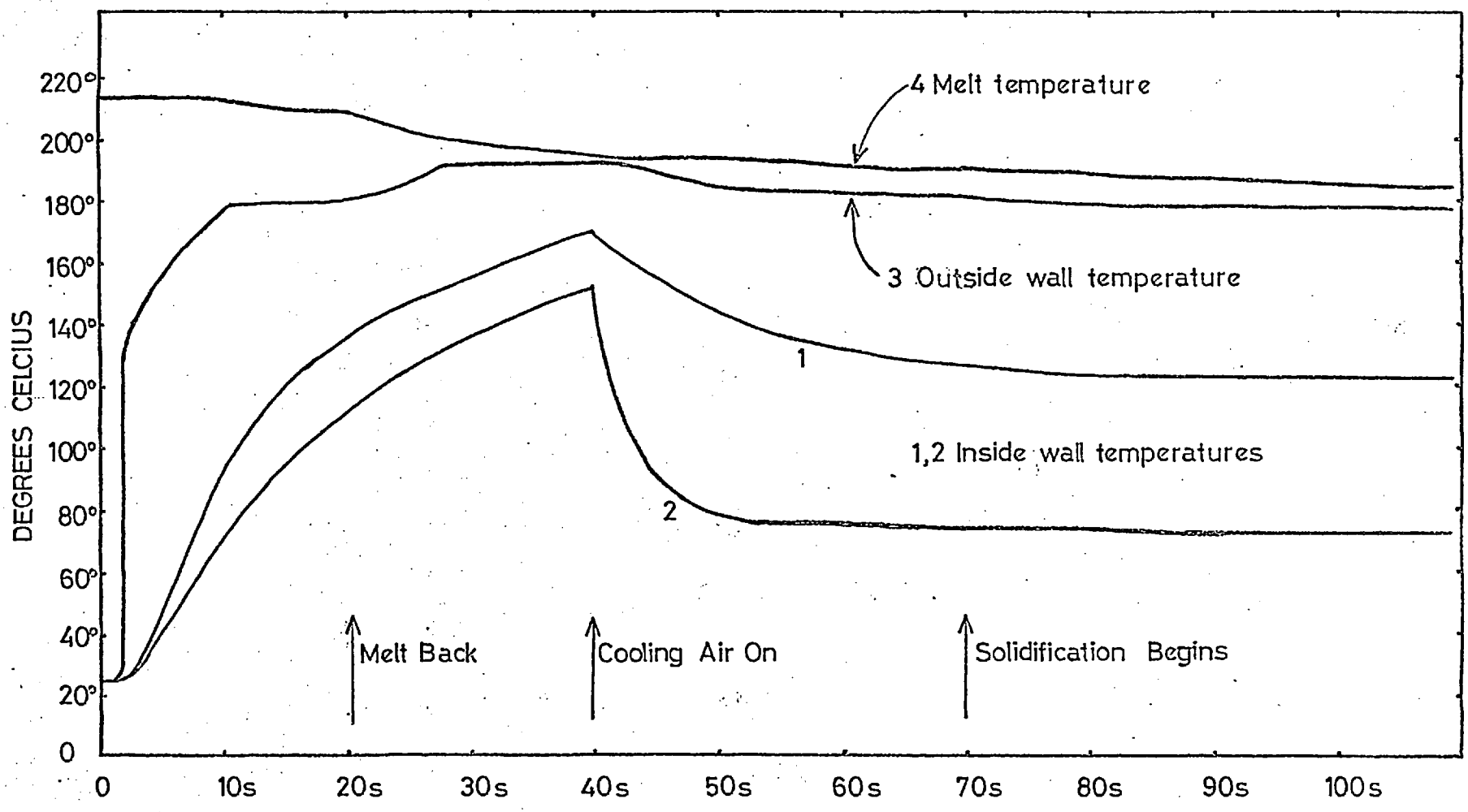


Fig. 45

Temperatures vs. Exposure Time. Eutectic Sn-Pb on Pb Insert Bonding Experiment, No 6 Table 14.

dissolution for the insert midpoint did not produce bonding even with careful surface preparation. At 30°C of superheat, 13s exposure at the centre of the insert was insufficient, yet 23s for dissolution produced good bonds. The final three bonding experiments used progressively more cooling air, but no difference in the microstructures was apparent. Fig. (45) shows temperatures during one such experiment, including the inset outer wall temperature.

Electron probe traces, Fig. (46) demonstrated that there was practically no diffusiom of tin across the interface.

6.5 Immersion of Rotating Stainless Probes into Ferrous Alloys

6.5.1 Chill Layer Growth. Eutectic Cast Iron

Three experiments at zero superheat again showed a large variation between consecutive experiments; the absolute values are about half of the predicted thickness for $H_i = 2{,}500$ W/m^2 °C, but a value of 500 W/m^2 °C produces a curve that passes between the measured thickness values, Fig. (47). The inside wall temperatures, presented in Fig. (48) however agree best with the curve for $H_i = 2{,}500$ W/m^2 °C.

6.5.2 Chill Layer Growth and Melt Back

6.5.2.1 Eutectic Cast Iron

The melt back time under conditions of 200 r.p.m., 30 kW and initially 90° superheat was found to be 45s static* exposure, exactly half that without rotation. Theoretical melt back is produced under these conditions by $H_i = 2{,}500$, $H_L = 11{,}000$/m^2 °C and these curves are compared to the thickness measured in Fig. (49). The temperatures agree surprisingly well, as shown in Fig. (50), those for the liquid metal coinciding exactly.

* Static here refers only to the vertical motion of the probe.

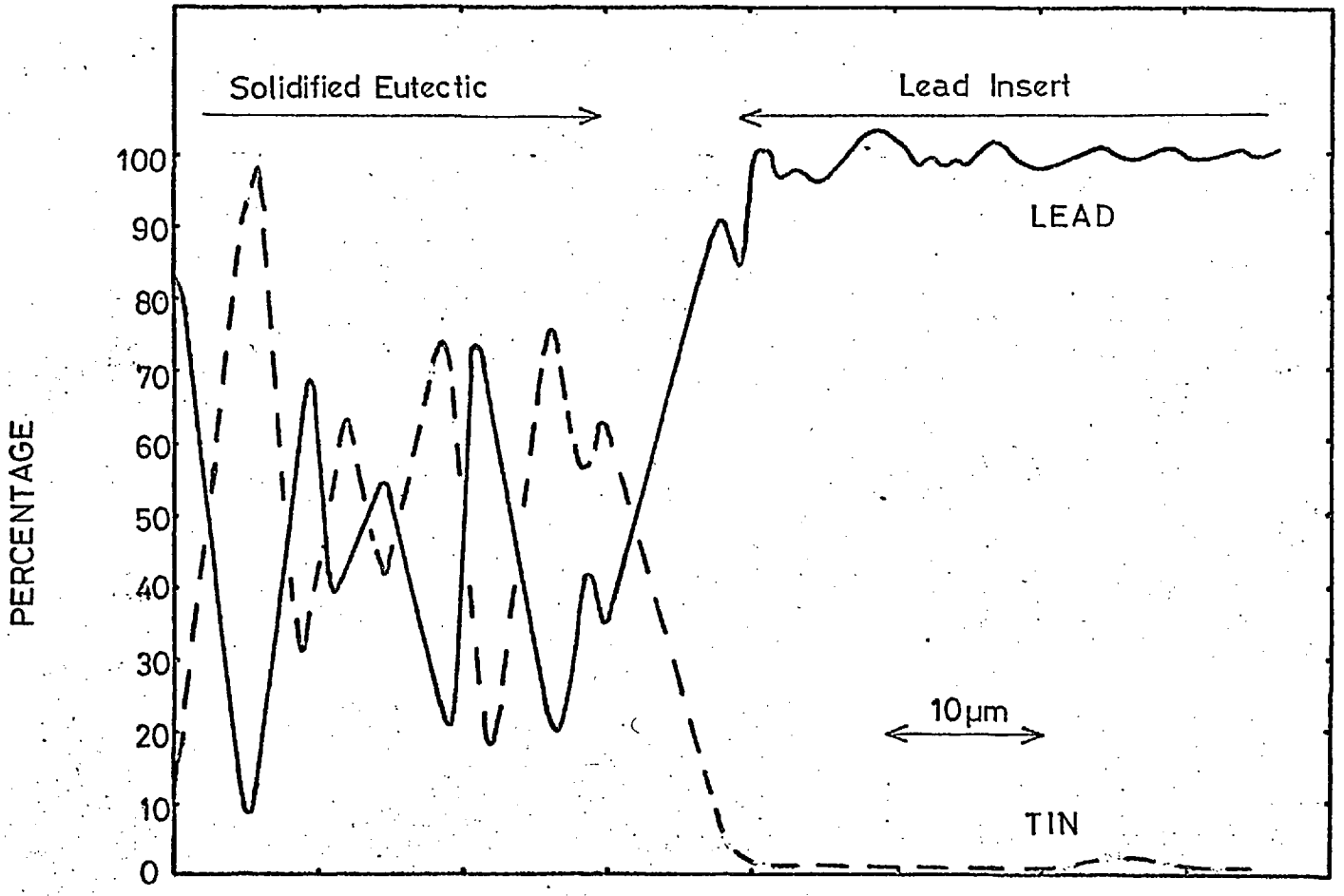


Fig. 46

Lead and Tin Diffusion for Eutectic Pb-Sn Clad Pb.

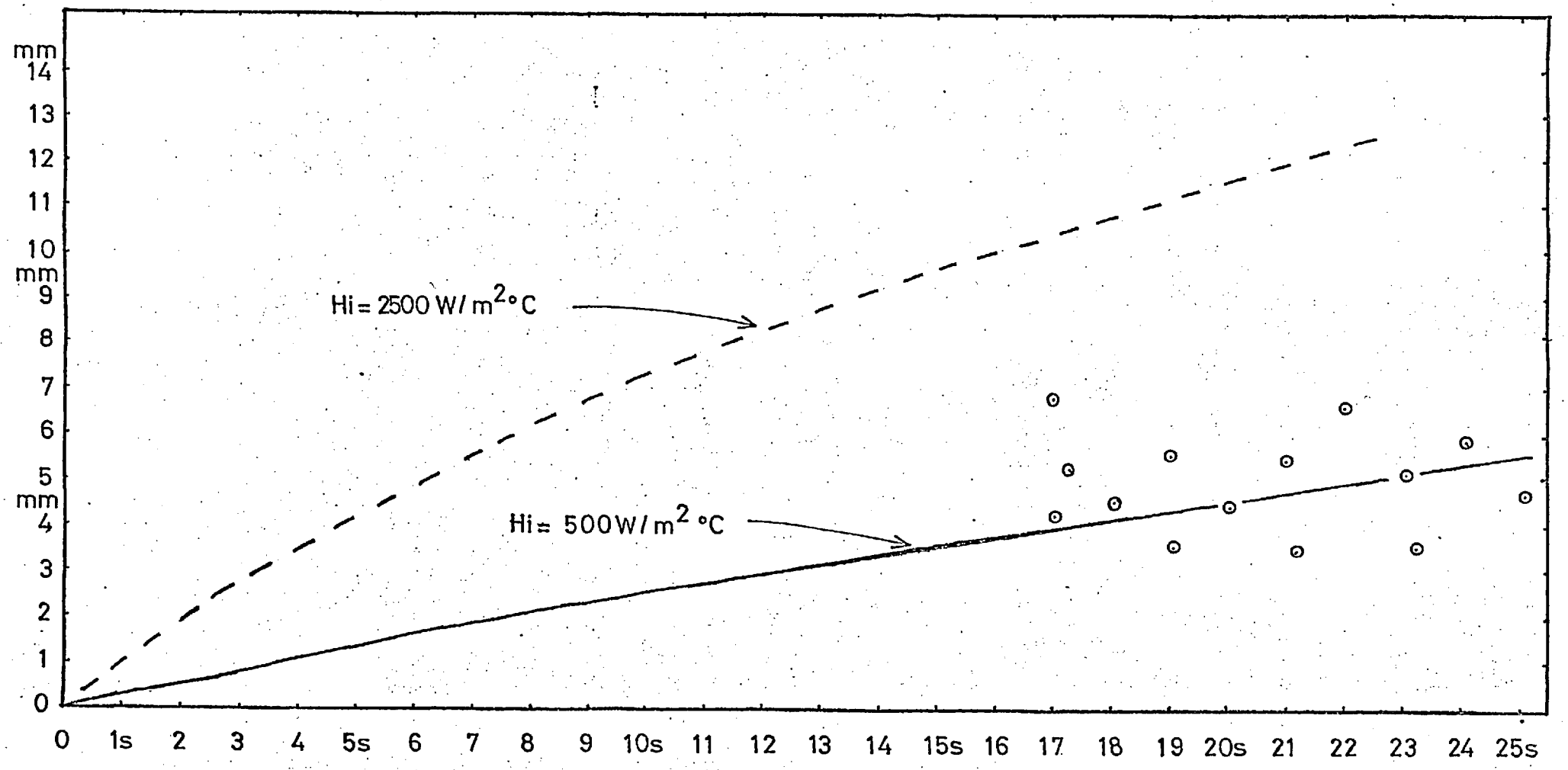


Fig. 47

Chill Layer Thickness vs. Exposure Time. Eutectic Cast Iron, zero Superheat, Stainless Probe rotating at 200 r.p.m..

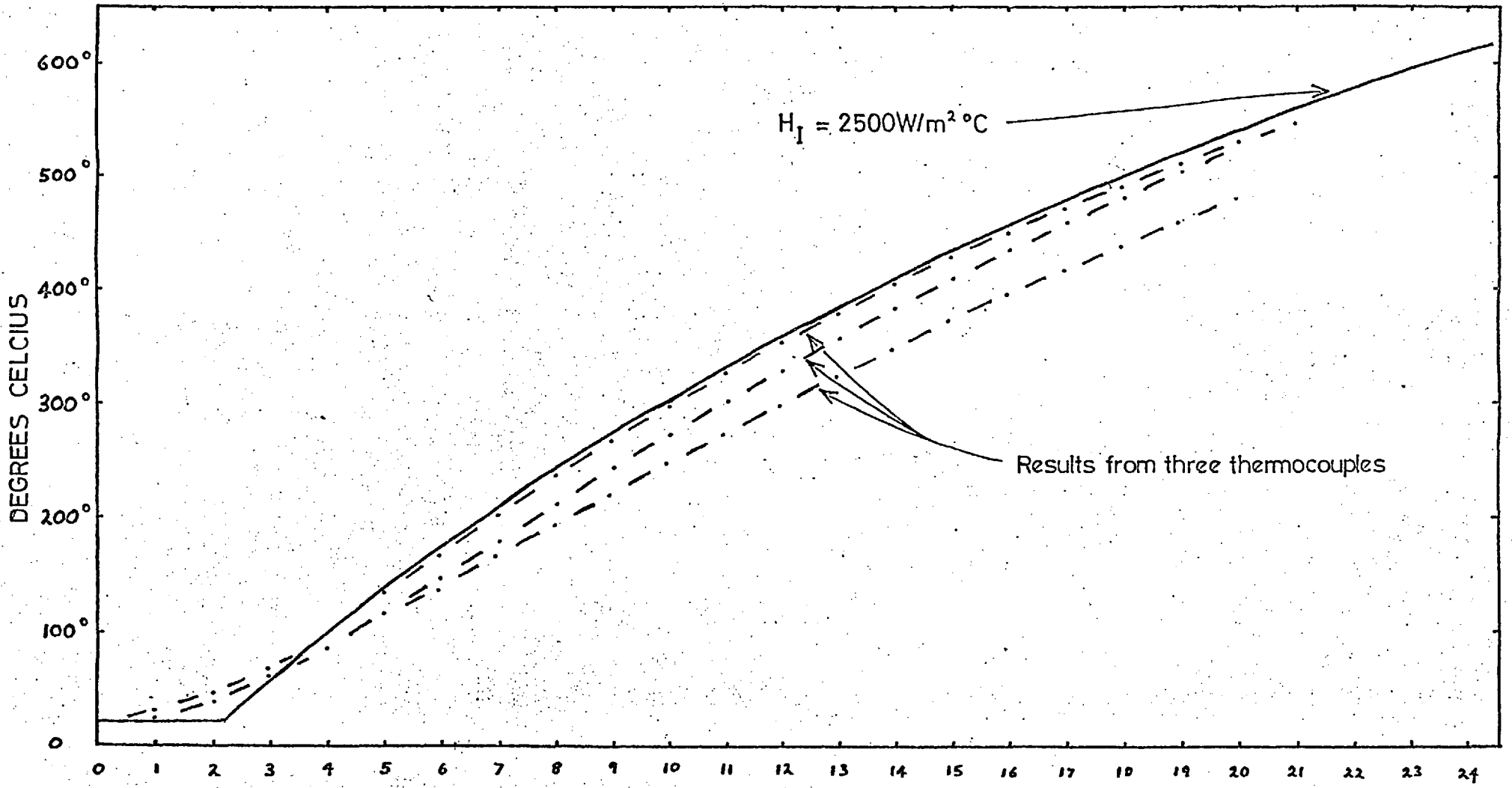
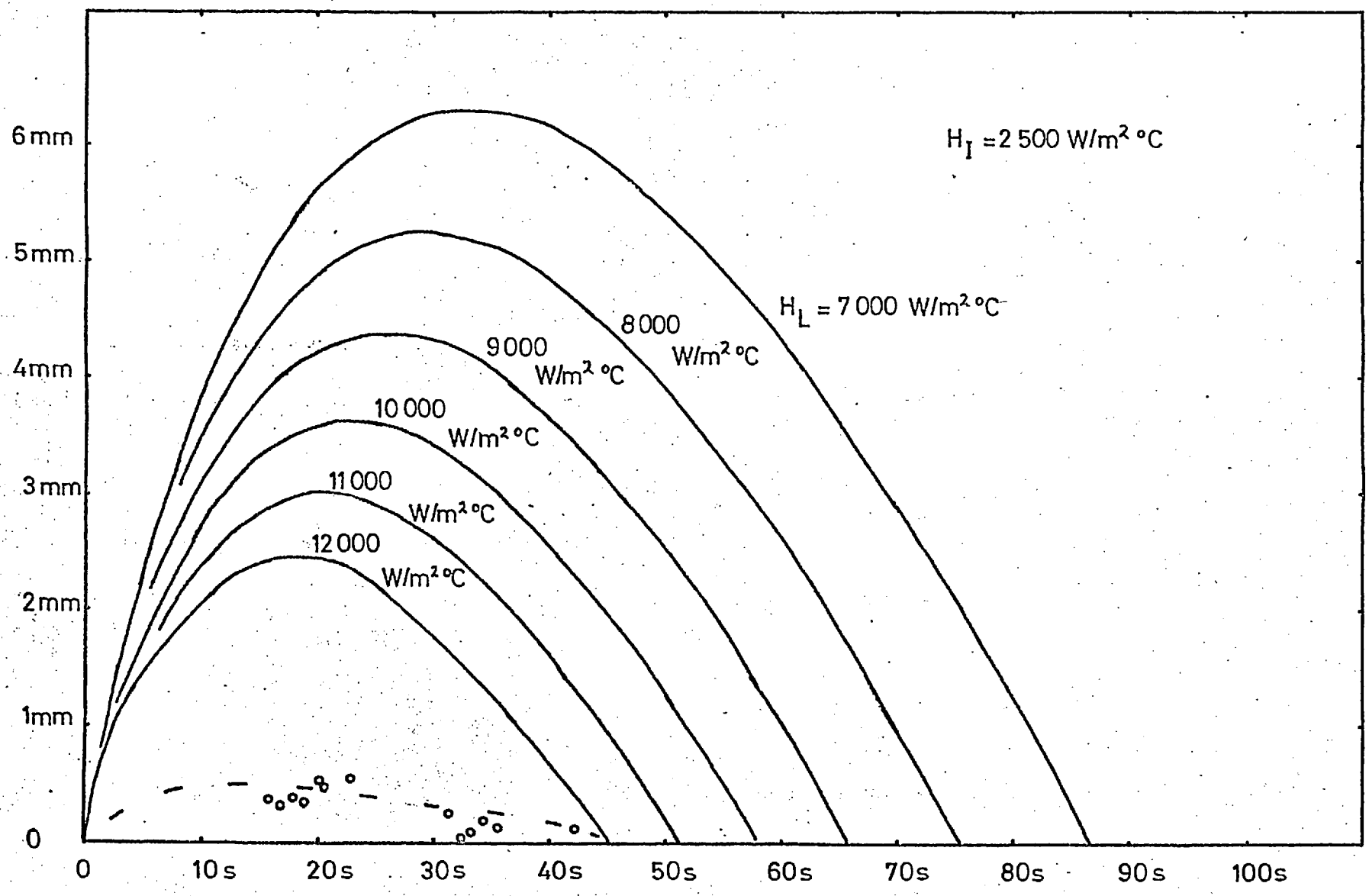


Fig. 48

Inside Wall Temperatures vs. Exposure Time. Eutectic Cast Iron, zero Superheat, Stainless Probe rotating at 200r.p.m..



Chill Thickness vs. Exposure Time. Eutectic Cast Iron, 90°C Superheat, Stainless Probe rotating at 200 r.p.m..

Fig. 49

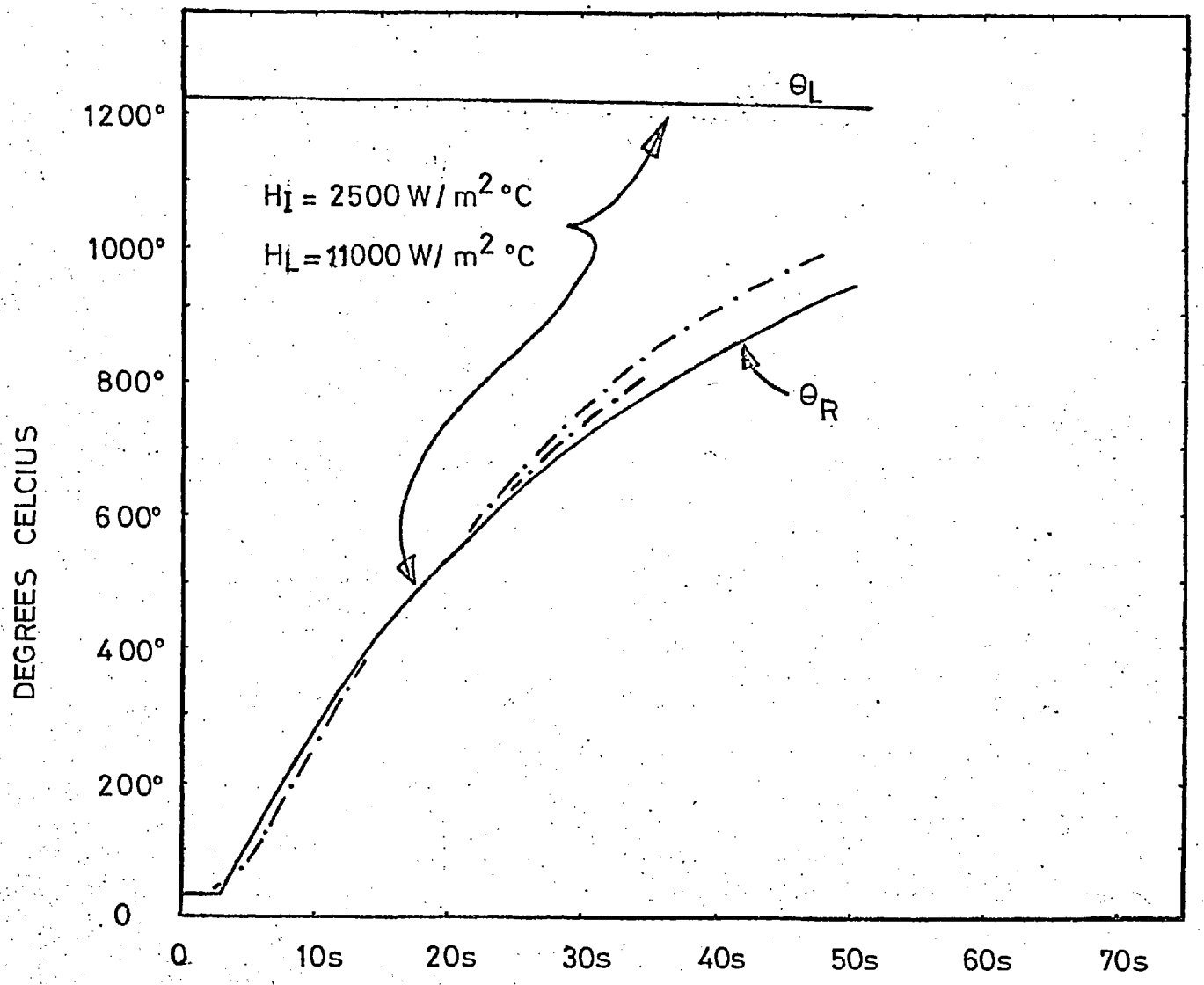


Fig. 50

Temperatures vs Exposure Time. Eutectic Cast Iron, 90°C Superheat, Stainless Probe rotating at 200 r.p.m..

6.5.2.2. 1.4% Steel

Table (15) summarises the seven experiments carried out, under conditions of 200 r.p.m. and initially 90°C of superheat, searching for melt back conditions. The results were a definite improvement on those without rotation, the photographs fig. (51) show the smoothness of the chill layers in comparison to those without rotation. Experiments 6 and 7 show there was a very fine balance between incomplete melt back and the complete melting of the stainless. Conditions between subsequent experiments were not reproducible, small variations in liquidus temperature and superheat had a large effect upon the rate of chill removal.

6.5.3 Bonding Experiments

6.5.3.1 Eutectic Cast Iron

Two attempts to bond this eutectic alloy to stainless steel were made, see table (16). The first did not allow any time for dissolution of the stainless surface and no bond was produced. The second allowed 15s for dissolution after melt back was completed, before starting the air cooling and was then successful in producing a bond. The inside thermocouples failed immediately the air cooling began. Electron probe traces and a photomicrograph are presented in figs. (52), (53).

6.5.3.2 1.4% Steel.

The uncertainty concerning the time for melt back caused difficulty in judging the correct moment for the start of air cooling. The experiment anticipated the melting of the probe by reducing power at 50s, and turning the air on at 55s, about 15s before melt back was expected. The sudden blast of air caused steel to spray out of the furnace and the experiment had to be terminated abruptly, see table (17).

TABLE (15)

EXPERIMENTAL CONDITIONS AND QUALITATIVE RESULTS
1.4% STEEL AT 200 r.p.m.

	Liquidus Temperature	Melt Temperature	Superheat	Power	Static Exposure Time	Comments
	°C	°C	°C	kW	s	
1	1437	1517	80	30	30	Smooth and Even. Thick.
2	1432	1509	77	30	50	Smooth but thick.
3	1415	1510	95	30	60	Smooth, a little thinner.
4	1415	1506	91	30	80	Melt back just began.
5	1420	1509	89	30	70	Large amount of melt back.
6	1417	1510	93	30	60	No stainless exposed.
7	1417	1510	93	30	70	All stainless melted.



(2) (3) (4) (5) (6)

WITH ROTATION Numbers refer to Table (15)

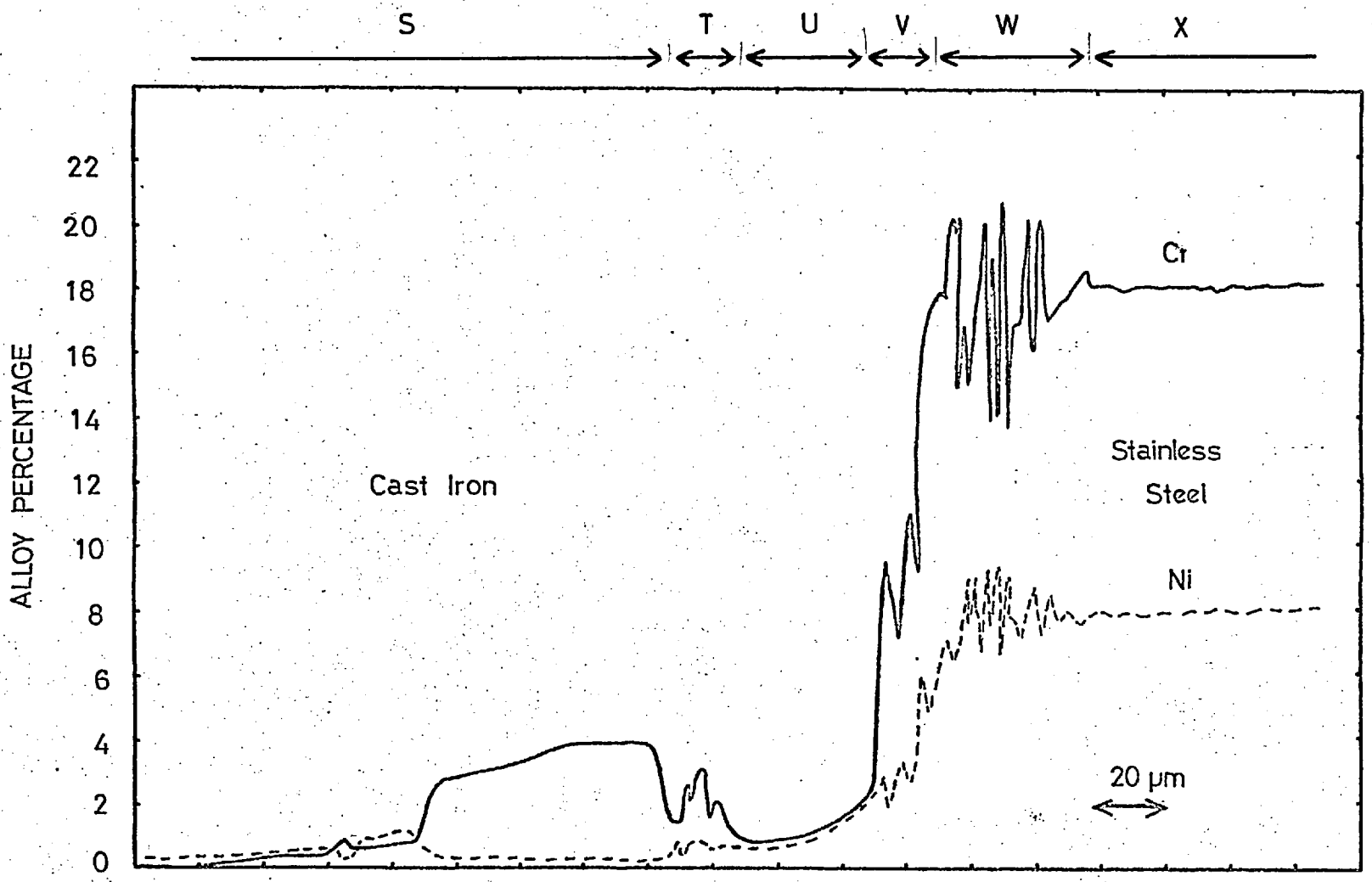


(5) (6) (7) (8) (9)

NO ROTATION Numbers refer to Table (5)

STAINLESS STEEL PROBES AFTER IMMERSION IN 1.4% STEEL AT ABOUT 90°C of SUPERHEAT.

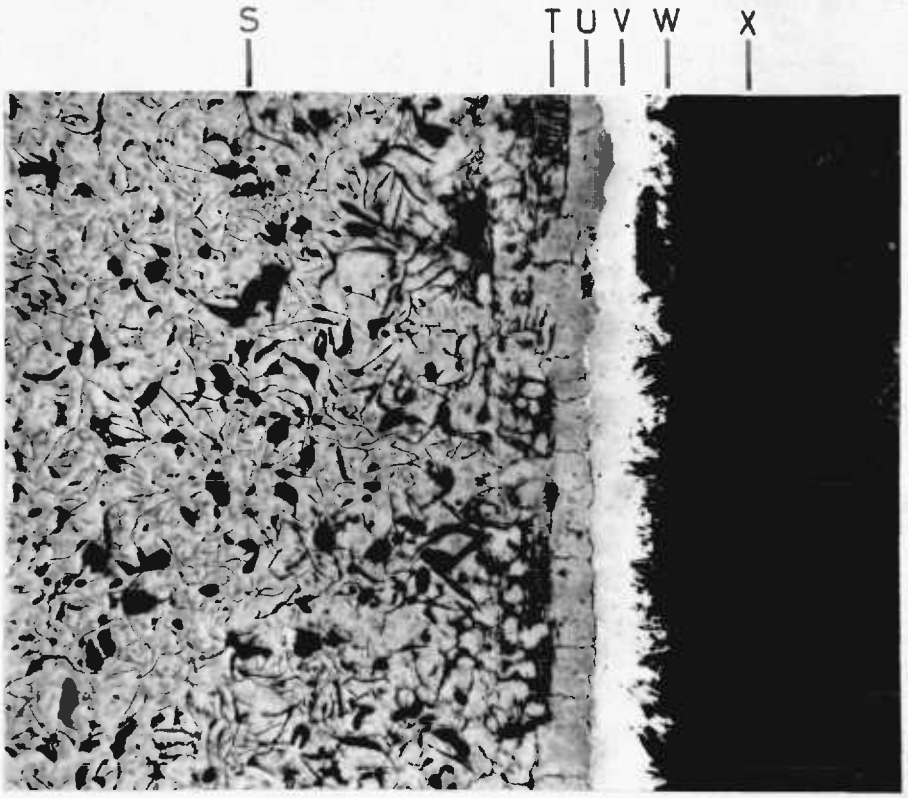
Fig. 51



Chromium and Nickel Diffusion for Stainless Clad Cast Iron.

Stainless Probe rotating at 200 r.p.m..

Fig. 52



X 240 ETCH: 10s in 2% NITAL
10 mins. in 'SELENIC ETCH'

MICROSTRUCTURE OF EUTECTIC CAST IRON BONDED TO STAINLESS STEEL WITH ROTATION 200 r.p.m.

Fig. 53

T A B L E (16)

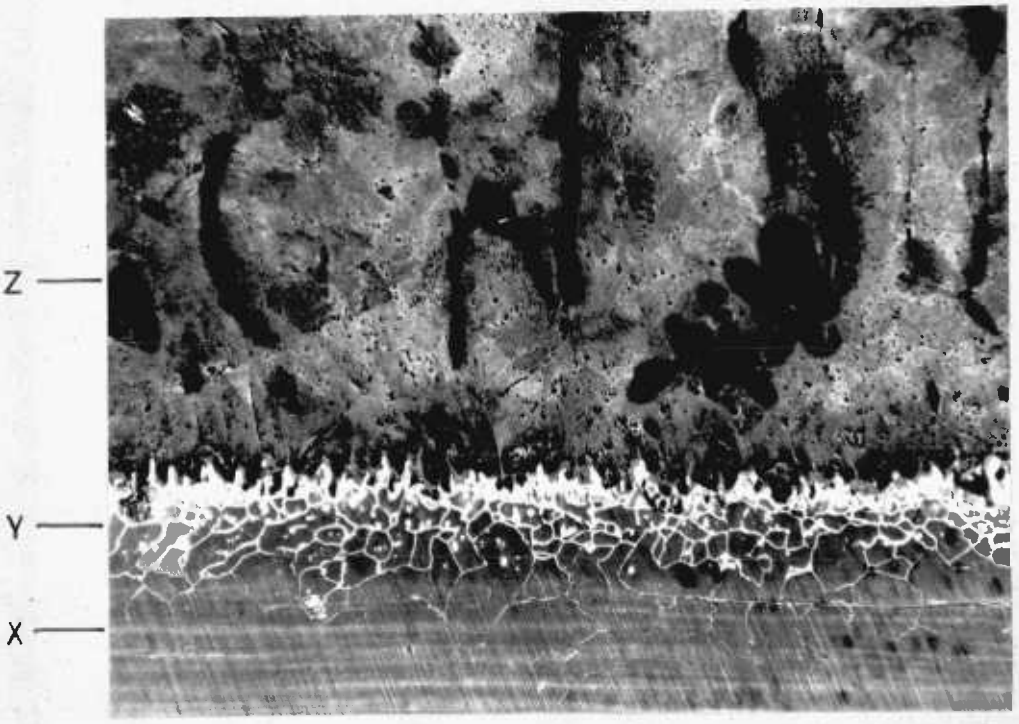
EXPERIMENTAL CONDITIONS FOR BONDING EXPERIMENTS.
EUTECTIC CAST IRON, 200 r.p.m.

Original Temperature	Original Superheat	Furnace Power	Time to Melt Back	Time for Dissolution	Time for Air	Volume of Air.	
°C	°C	kW	s	s	s	m^3/s	Comment.
Eutectic Cast Iron							
1226	91	30 5 after 60s.	45	0	135	$3.2.10^{-2}$	No Bond
1232	97	30 10 after 70s	45	15	210	$3.0.10^{-2}$	Bond O.K.

T A B L E (17)

1.4% Steel							
1420	90	30 10 after 50s	70	-15*	3	$3.2.10^{-2}$	

* Air cooling started before complete melt back was expected, and then abruptly stopped.



X 240 ETCH: 10s in 2% NITAL
10 mins. in 'SELENIC ETCH'

MICROSTRUCTURE OF 1.4% STEEL PARTIALLY BONDED TO STAINLESS STEEL.

Fig. 54

Although this incident suggested that carbon steel/ stainless steel bonds could not be produced using a solid stainless steel probe and a carbon steel bath, it did demonstrate the effectiveness of the safety screens. No molten steel passed through the metal gauze and no extensive damage was done. Some of the chill layer bonded during the earlier melt back experiment was prepared and the photomicrograph is fig. (54). Cracks in the chill layer are clearly seen at the interface (zone Z).

7. DISCUSSION

7.1 Introduction

The overall aim and scope of the investigation was to study the heat transfer conditions that enabled a bond to be made between a substrate and a layer of solidified metal. The steps involved in the successful production of a bond were :-

Growth of a chill layer.
Subsequent melt back of the chill layer.
Dissolution or melting of the substrate surface.
Growth of the bonded layer.

These four steps have been studied more or less completely, from experimental and theoretical aspects, for a range of ferrous alloys solidified onto stainless steel and for the tin-lead eutectic alloy solidified onto a lead substrate. The experiments with stainless steel as the substrate involved both double sided ingot cladding and static or rotating stainless steel probes dipped into melts of ferrous metals.

7.2 Double Sided Ingot Cladding

Under any circumstances bonding needs to overcome surface barriers so that intimate contact between the two components may be established. With these experiments it was not possible to separate the different steps of chill layer growth, melt back and dissolution.

Scratch brushing surfaces was known to have a beneficial effect provided they are used quickly, before significant oxide thickness reforms. Preheating the plates in situ for several hours negated any improvement. The small scale of operation meant that even with the high casting temperatures, the steel remained liquid for a very short time. This limited time is insufficient to allow oxide barriers to diffuse away

and bonding must therefore be created by melting the stainless surface. The later work showed that contacting liquid metal with solid stainless at temperatures above its liquidus of 1420°C is almost certain to melt the stainless completely.

The uneven distribution of heat from the liquid suddenly decanted into the mould meant that in extreme cases the plate outer surfaces showed concentric regions of melted, bonded and non bonded areas. The centre where the plates were melted coincided with the hot spots on the outer faces of the ingot moulds. The use of higher preheat and liquid temperatures appeared, inconsistently, to increase the melted area.

The results presented in Table (1) show no trend of more bonding with increasing temperatures. This was undoubtably due to difficulties in controlling transference, trajectory and turbulence of the liquid metal during casting, as well as inconsistency in resultant temperature distributions. 'Splash tubes' were ineffective in improving control as they did not affect the heat distribution.

Immediately after casting there was the danger of the solidified metal contracting away from the stainless steel, breaking any tentative bond. The use of cylinders of stainless steel in later work meant that contraction forces assisted bond formation, rather than aggravating failure.

7.3 Cylindrical Probe Experiments.

7.3.1 Chill Layer Growth

The theoretical-experimental correlation for zero superheat experiments is good. Figure (35) representing this correlation for the lead experiments shows the effect of doubling the interface heat transfer coefficient; the rate of rise of thickness initially is larger but the final limit is the same. The lower value (H_I = 1,500 W/m^2°C)

produces a curve which lies in between the measured values.

The spread of the three results from each individual experiment is about twice the calculated mean standard deviation, roughly equivalent with a 95% confidence limit. If this spread is superimposed upon the predicted curve for H_I = 1500 W/m^2 °C, it encompasses nearly 80% of the values. In the experiment with 120 s static exposure the effect of heat losses appeared and the metal thickness measured on the insert is greater than predicted, implying a total heat loss of about 15%.

The similar curves for eutectic cast iron are for low exposure times, long before the plateau is reached. The three separate experiments without rotation, fig. (24) cover a wide range of thickness with a spread larger than expected from the mean standard deviation figures. In view of the uncertainty between replicate experiments the interface heat transfer coefficient of 2500 W/m^2 °C is the best estimate between outside limits of 1500 and 3500 W/m^2 °C. The thickness of the metal that solidified on a probe rotating at 200 r.p.m. is far below that without rotation, an expected 12 mm is reduced to 5 mm, fig. (47), (24). A curve at 500 W/m^2 °C falls between the data.

A speed of rotation increase from zero to 200 r.p.m. appears to cause a reduction from 2500 W/m^2 °C to 500 W/m^2 °C for the interface heat transfer coefficient with eutectic cast iron. On the contrary the zero superheat experiments with tin lead solidifying onto stainless, fig. (37), show that an increase in rotation speed does not affect the results at low times and small thicknesses. A thickness of about 7 mm is not affected, however at longer exposure that of 12 mm is reduced to 10 mm. All these results could be made to match a theoretical prediction more closely if the interface coefficient varied during each experiment. An initially high value gradually decreasing as the chill layer thickness increases could produce a curve closer to the experimental points. Such an adjustment to the curve for tin-lead on lead fig. (35) would make the already good correlation

virtually perfect. The large scatter of the ferrous results makes such a varying coefficient less important for fitting experiments but can explain the lower thickness at higher speeds if the rate of fall of H_I is large. These adjustments to the shape of the curve produced by the theory are in reality an attempt to compensate for the errors produced by the assumption of directional heat flow. Neither these errors nor these adjustments can explain the effect of rotation speed upon metal thickness at zero superheat. The existance of a 'constraint' effect could explain the experimental results.

The rotating probes were not in an infinite medium, but in one bounded by an outer cylinder. The growth of the chill layer restricted the space for turbulent fluid flow, and increased the liquid velocity ahead of the solidifying front. A chill layer thickness of 12 mm occupied 21% of the annular space. Solid growth into liquid metal which is increasingly accelerated is affected by increasingly disturbed conditions ahead of the interface. The undercooling needed for continued growth could be destroyed and the growth rate checked. This constraint effect would be greater for the ferrous experiments, since the furnace lining did not form a smooth, uniform, outer cylinder and locally the annular space would be further restricted.

7.3.2 Chill Layer Melt Back

7.3.2.1 No Rotation

The cast iron thickness measured after partial melt back exhibits considerable scatter but excepting a single high value the experiments at 90°C and 50°C of superheat were roughly the same. In both cases the thickness fall far below these predicted (Fig. 26, 28), for equivalent melt back times.

The zero superheat experiments showed that within 10 and 16 seconds the most likely interface heat transfer coefficient

was 2,500 $W/m^2\ ^oC$. If the interface heat transfer coefficient is the same with and without superheat, or if the value falls after 16s exposure it will not affect the initial shape of the melt back curve. There is no reason to expect superheat to affect the coefficient, but the value may depend upon other factors, such as contact pressure. The constraint effect will not operate without rotation and consequently cannot explain the discrepancy between theory and experiment. Radial heat flow causes only a small difference from the assumed unidirectional heat flow at the measured thickness values, ($<$ 2 mm).

Despite lack of rotation the liquid cast iron was not static. In addition to the disturbance caused by the initial displacement of the liquid, convection currents existed from the interaction of the power input and the cold probe. It is possible that the combination of liquid movements could disturb the undercooling necessary for continued solidification, once the chill layer has formed. That is, the mechanism supplying heat during melt back could operate to reduce the maximum thickness attained.

7.3.2.2 With Rotation

Rotation of the probes during melt back of cast iron at 90°C of superheat caused the measured thickness (fig. 49) to be about half that without rotation (fig. 28). Forced convection was superimposed upon natural convection and the initial disturbance, and it seems this exaggerated the disturbance of the undercooling ahead of the solidification front. On the contrary the theorectical melt back curves for tin-lead on lead fell below the measured thickness, at least for H_I = 1500 $W/m^2\ ^oC$. Surprisingly the predictions for H_I = 3000 $W/m^2\ ^oC$ straddle most of the results (fig.39). As there is no justification for using a different value to that used earlier this must be considered fortuitous. (Fig.44) shows that the measured liquid temperature adjacent to the probe cools progressively from the start of the experiments, yet the bulk liquid temperature

stays virtually constant for 15s. A full minute passes before these two temperatures coincide. That is the liquid is not thermally mixed and a cold layer initially exists ahead of the interface.

The thermal conditions are further complicated as a finite time is taken before turbulent flow is fully established in the annular space. The temperature gradient in the liquid metal is a balance between the heat flux creating the gradient and the turbulent mixing trying to destroy it. Consequently as the experiment proceeds and the turbulence exerts itself the cold layer disappears. This is entirely consistent with the situation in cast irons in view of the Prandtl numbers of the liquids:

$$(P_r \text{ tin-lead} = .018)$$
$$(P_r \text{ cast iron} = .35)$$

It is simply illustrated by assuming laminar fluid flow when the Prandtl number is the ratio of thermal to eddy diffusivities. Thus for constant hydrodynamic conditions the thermal diffusivities in liquid cast iron are twenty times that of liquid tin-lead. Consequently bulk mixing is so efficient that a cold layer cannot exist in liquid cast iron for any appreciable length of time. The situation in turbulent flow is more complicated but very similar.

The experiments with tin-lead solidifying onto a stainless steel probe highlight discrepancies within the theoretical calculations. Using the most likely interface heat transfer coefficient (2,000 $W/m^2\ ^oC$) the theory predicts melt back will not occur at 30^oC of superheat; directly contrary to the experiment, (Fig. 43). The failure of the theory is because the properties of stainless steel, particularly the low thermal diffusivity, are very different from that of tin-lead. These differences exaggerate errors caused by the assumptions such as quadratic temperature profile, temperature independent thermal properties. The growth rate of the solid is directly related to the balance between heat removed by the wall, and the heat supplied from the liquid. This balance is crucial since in predicting the experimental results with tin-lead in contact with stainless steel it can change three

times in under ten seconds (see fig.43).

There is no justification for a separate mechanism to explain discrepancies for each group of experiments, the similarity of the systems means a consistent argument must be followed throughout. A varying interface heat transfer coefficient cannot be discarded, but it does not account for all the effects observed unless it varies periodically in a random manner. A coefficient that is an inverse function of time would cause the solid removal rate to increase continuously. In fact the rate of change of solid formation decreases, at least in the final stages of each experiment. A coefficient that is an inverse function of chill layer thickness could reduce the thickness as for cast iron, but the converse is needed to explain the experiments. The difference in the liquid Prandtl numbers is consistent with the idea of a 'constraint effect' used as an explanation of the reduction in chill layer thickness with increasing rotation speed at zero superheat.

7.3.2.3 Liquid Metal Heat Transfer

The time to melt back depends upon the rate of heat transfer from the liquid. Theoretically this is expressed in terms of the liquid heat transfer coefficient as defined by equation (28) which has the inherent assumption of a uniform bulk liquid temperature.

The heat flow within the superheated liquid metal is complicated by the increase of the inner cylinder diameter with chill layer growth. This increases the Reynolds number at constant rotation speed. The change in annular size is likely to be unimportant as Eisenberg et al [42] say that in aqueous mass transfer turbulent flow causes the effect of the annular gap to disappear. In addition, for the special case of liquid metal heat transfer, the temperature gradients can depend upon the heat flux, despite turbulent flow. Turbulence may be effective in creating a uniform bulk concentration but not necessarily a uniform

bulk temperature. Thus the equation used to express the heat flow from the liquid does not truly model the circumstances.

As long as there is sufficient heat, as superheat, in the liquid to raise the mould temperature above that at which the liquid solidifies melt back will be complete. Under these conditions the solidifying and remelting layer is only a relatively small interference in the flow of heat into the mould. The time for complete melt back to occur theoretically is insensitive to interface heat transfer coefficient at low liquid heat transfer coefficients, see fig. (55).

The best experimental time for comparison with the theory is, in view of heat losses, the time for a completely clear ring of substrate to appear. Where this was not measured experimentally an estimate has been made, and this time used to deduce the liquid heat transfer coefficient, (table 18) Figures (55), (56) make the deduction simpler, by assuming the theory predicts accurate melt back times, and plotting these times for the different liquid, and interface heat transfer coefficients obtained. This procedure focuses attention on melt back time and removes emphasis from the thickness data.

The liquid heat transfer coefficients obtained in this way are nearly independent of superheat, as would be expected. Closer inspection shows that an increase in superheat (table 18) slightly reduces the values obtained. This is reasonable since the maximum chill layer thickness is smaller with higher superheat, and the average Reynolds number (at a fixed rotation speed) would thus be lower.

The agreement with the empirical relationship developed in Appendix (7) is reasonable for the tin-lead system but falls down badly when applied to cast iron. The difference without rotation, a factor larger than 10, can be explained to some extent. Experimentally heat transfer does not correspond to pure conduction, because of forced convection induced by furnace power. Estimation of natural convection effects from Eckerts[64] equation give a liquid heat transfer

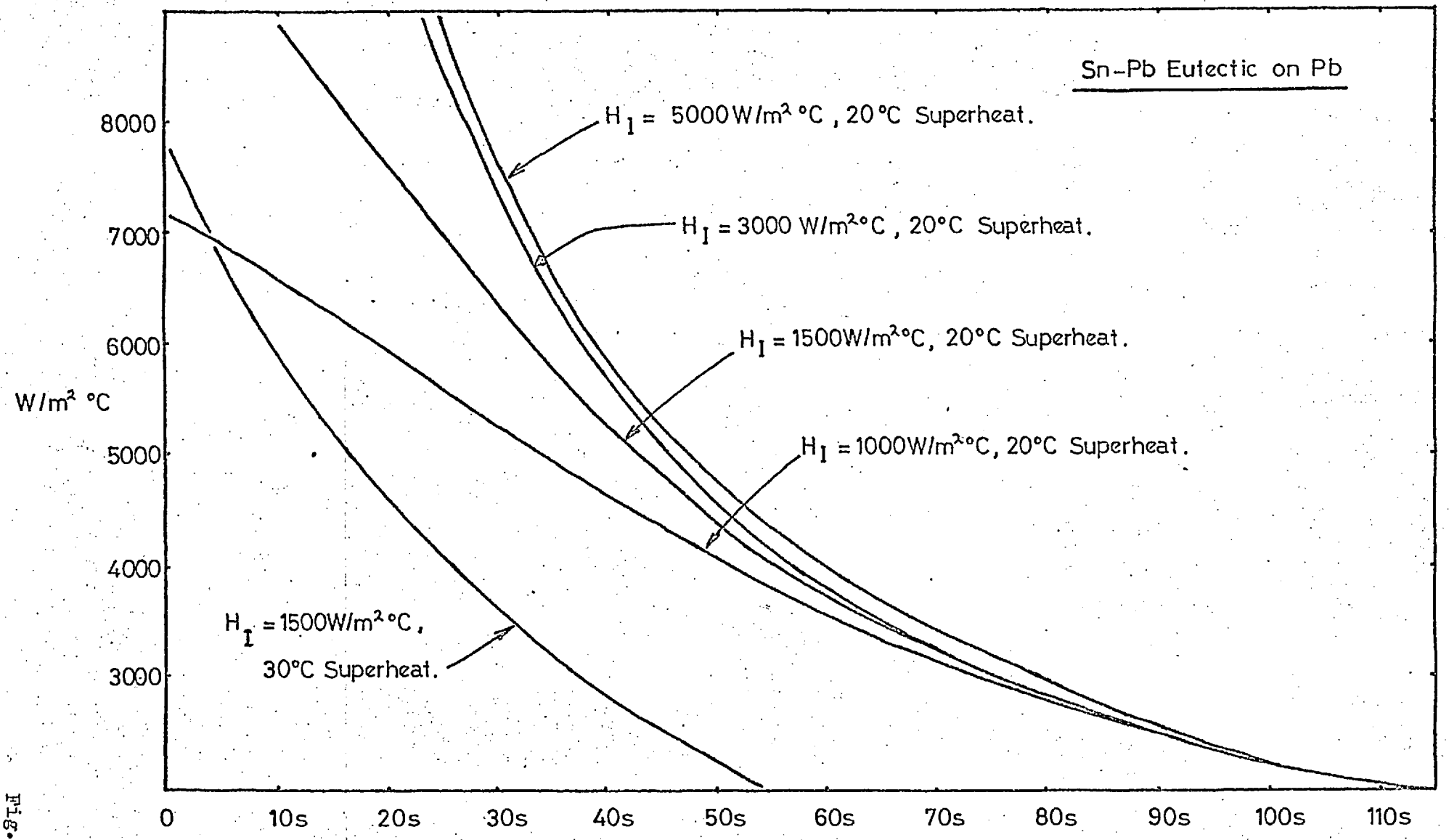


Fig. 55

Theorectical Time to Melt Back vs. Liquid Heat Transfer Coefficients.

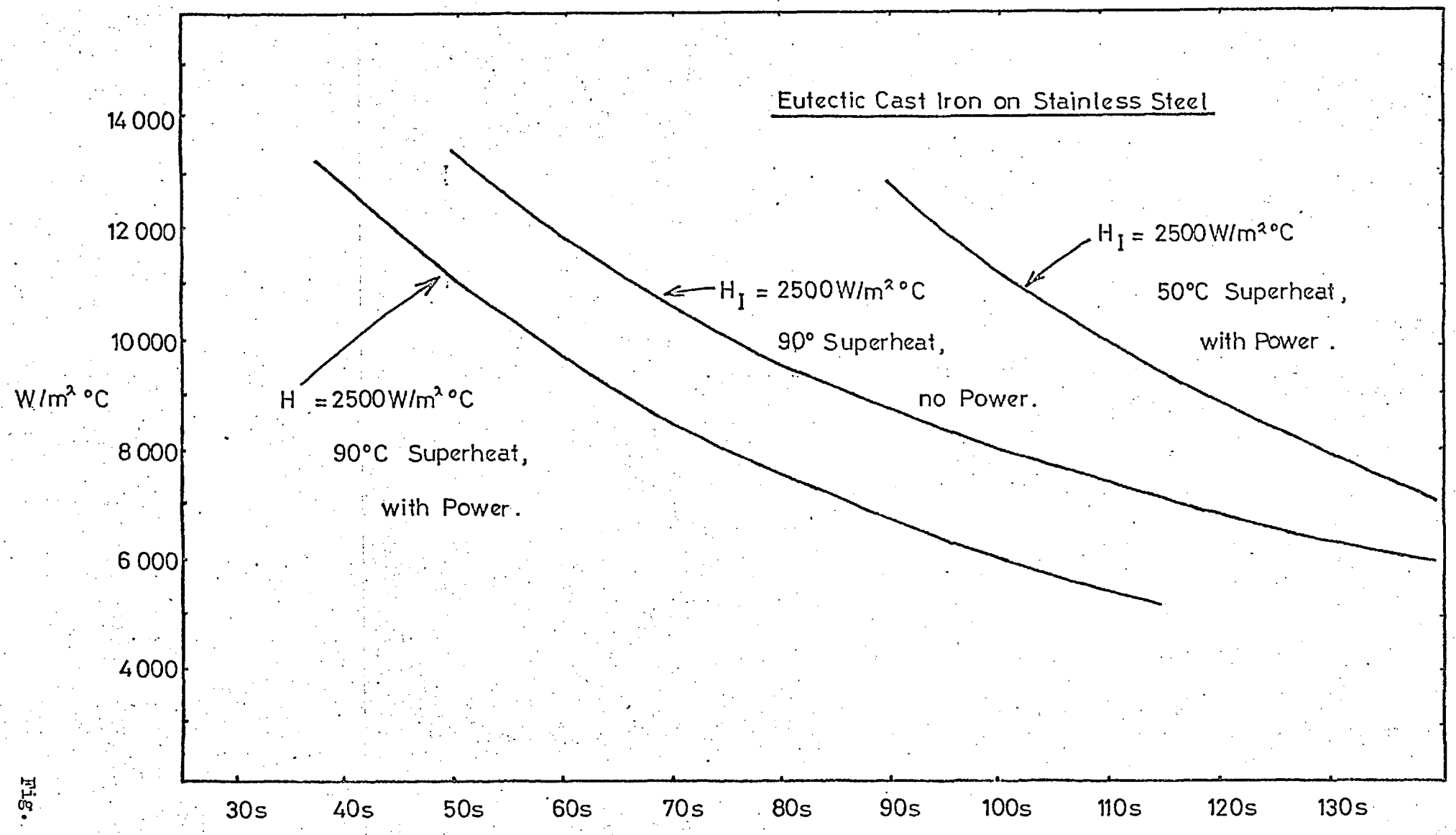


Fig. 56

Theorectical Time to Melt Back vs. Liquid Heat Transfer Coefficients.

T A B L E (18)

EXPERIMENTAL MELT BACK CONDITIONS AND LIQUID METAL HEAT TRANSFER COEFFICIENTS

System	Experimental Conditions		Melt Back Time		Liquid Heat Transfer Coefficient.	
			On all substrate	A clear ring	Fig.(55 56)	Appendix (7)
	^{o}C	r.p.m.	s	s	$W/m^2\ ^{o}C$	$W/m^2\ ^{o}C$
Sn - Pb	20	68	60	40	5300	3340
eutectic	20	200	25	(20)	7500	6420
on Pb	30	68	22	17	5100	3340
insert	30	200	10	(5)	6800	6420
Cast Iron	50	0	115	(130)	8000	730
eutectic	90	0	95	(80)	7500	730
on stainless	90	200	45	35	14000	6430
Sn - Pb	30	68	45	-	-	3340
eutectic on stainless	30	200	30	-	-	6420

coefficient of about half that due to conduction alone, and was discarded. With rotation the difference is a factor of about two, but again there is insufficient data for a complete test of the empirical equation.

The development of equation (47)$_{\text{p170}}$ used the work of Dwyer and Tu[52] as it is closely related to the present situation. They assumed constant surface heat flux, but for a solidifying surface the boundary condition is constant surface temperature. Data presented by Coombs et al for liquid metal in pipes, show the constant heat flux boundary conditions to give Nusselt numbers 20% above the uniform wall temperature conditions, but the difference decreases with increasing Peclet number.

Excepting the inherent difficulties of experimenting with cast iron, and the indirect approach to liquid heat transfer coefficients there is no apparent cause for the discrepancies obtained.

7.3.3 Dissolution or Melting of Substrate Surfaces.

Bonding produced by the experimental techniques used here relies on dissolution of the probe to prepare a clean surface. If such dissolution occurs there is no limit to the different alloys, or even possibly non metallics that can be bonded.

In the case of lead dissolving in tin-lead eutectic the controlling step is the reaction at the solid surface. The process is very similar to etching, with preferential attacks at grains presenting favourable crystal orientation. Prolonged dissolution of the lead inserts demonstrated this, as illustrated in figure (42). Lommel and Chalmers[49] have shown similar orientation effects. They also pointed out that in a static liquid, diffusion of lead in the liquid becomes the rate controlling step.

In ferrous systems the higher temperatures encouraged surface reactions so they are more rapid than the liquid diffusion, which has become the rate controlling step. The diffusion of carbon in molten ferrous alloys is known to be

the rate controlling step during dissolution of rotating carbon and steel cylinders. Consequently the dissolution rate is dependent upon forced convection and at low rotation speeds natural convection can dominate the process. Although no direct experimental evidence was produced here it is likely that the stainless cylinders dissolved in molten cast iron under liquid diffusion control.

The mechanism is possibly the reduction of the melting point of the stainless surface because of the increase in carbon content, as well as diffusion of iron, chromium and nickel into the liquid.

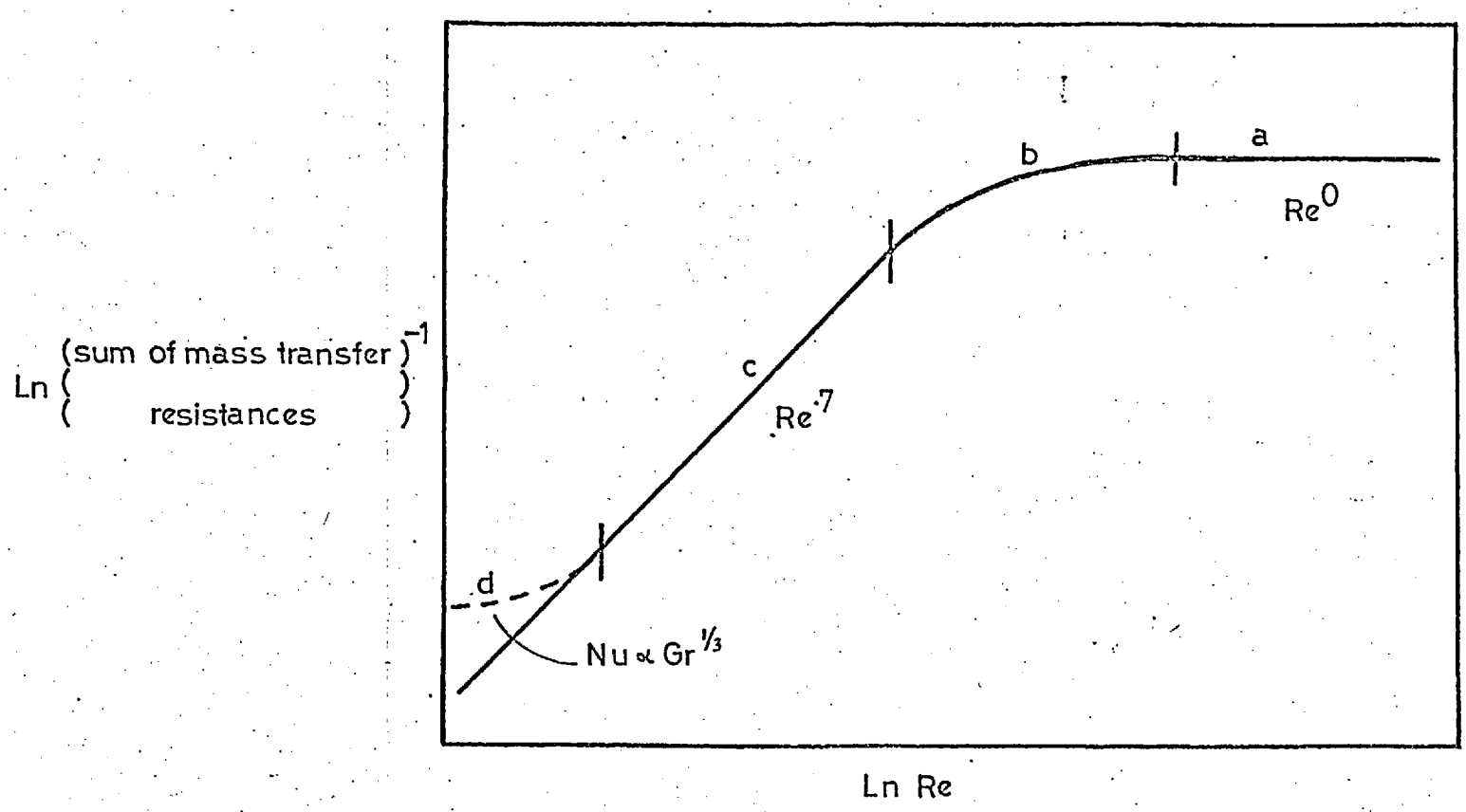
The experiments with 1.4% steel were at temperatures such that the stainless steel melted and heat transfer became the rate controlling step. The process analytically being very similar to melt back. Melting of the stainless steel, when exposed to the molten steel, was rapid, apparently more rapid than remelting of the solidified layer. This is probably associated with the smaller difference between liquidus and solidus temperatures, and the ease with which the alloyed nickel and chromium dispersed in the liquid.

The general shape of a mass transfer (and heat transfer) curve for rotating cylinders is as shown in figure (57). Various workers have operated at different positions on the curve. As the Reynolds number is purely an expression of forced convection the curve may be disturbed at the low end if natural convection becomes important.

7.3.4 Growth of Bonded Layers

Bonding experiments with both lead and cast iron clearly demonstrated that a period for dissolution was needed before successful growth of bonded layers. This dissolution created conditions needed for good bonding by removing oxide films and any other barriers and allowing the contaminants to disperse in the bulk of the liquid.

The amount of heat removed by the cooling air was comparatively small, and solidification did not occur



a. Surface Reaction Control
ref 49

b. Duplex Control
ref. 47

c. Liquid Diffusion Control
ref. 42,44

d. Natural Convection Control
(heat transfer)
ref. 35

General Curve for Rotating Cylinder Mass Transfer.

Fig. 57

immediately. Heat was gradually removed from the liquid until the amounts conducted through the wall exceeded that supplied from the liquid.

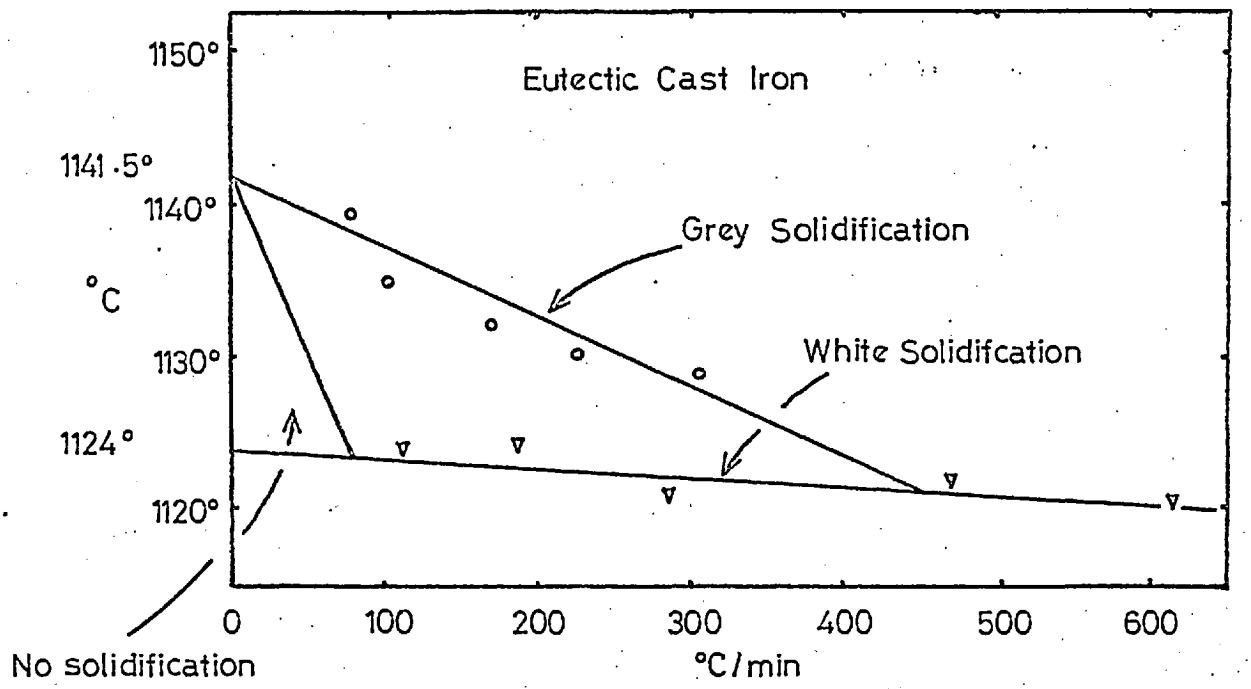
The solid growth rate was small, in comparison with chill growth, despite the bonded layer being in perfect thermal contact with the substrate. This was because the solid growth rate is directly related to the rate of heat removal.

7.3.4.1 Eutectic Cast Iron

The analysis results confirmed the composition determined by the liquidus measurement, using a carbon equivalent of $(C + \frac{Si}{3})$ on the phase diagram from Angus [14]

The eutectic arrest measured in the melts was not that given on the normal iron/carbon equilibrium diagram for the solidification of graphite (1153°C). In view of Oldfields comment [62] "It is a well known fact however, that under practical conditions the eutectic arrest is mostly found at lower temperatures than that given by the equilibrium diagram." this is not surprising. The diagram in Angus shows the graphite eutectic point at 1135°, the temperature at which the alloys solidified finally, both in and out of the furnace. Reference to Fig. (58) suggests these irons cooled at 150° C/Min.

Nearly all the early results, with large fluctuations of eutectic cast iron shell thickness, invariably associated thick areas with white iron. Hillert [15] says that the rate of solidification is low as long as it is grey, but it suddenly increases if white solidification starts. White solidification when nucleated spreads very fast and swamps grey solidification. Close inspection of shell sections showed that some of the iron had started solidifying white yet a grey structure was formed at intervals. In every case the last metal solidifying was grey. It appears that an area of more intense heat transfer induced white solidification, but the solid grew into a positive temperature gradient which caused a temporary reversion to



Maximum Eutectic Arrest Temperature vs. Cooling Rate. after Oldfield.[62]

Fig. 58

grey iron, before white solidification again proceeded. This is contrary to Hillerts' 'swamping' effect, but as mass transfer in Fe/C systems is normally controlled by carbon diffusion, the solid growth must be a balance of both mass transfer and the imposed temperature gradient. Hillert also mentions that if the carbon content is above 3.8% the molar volume of graphite is considerably higher than the partial molar volume of carbon in the liquid solution, and the grey iron expands on solidification. This expansion initially opposes any tenuous bonds that may be formed, by movement of the eutectic away from the stainless. When the solidified shell is thicker it may stress the bond still further. Cooling of the composite at the end of an experiment allowed differential expansion to reverse the stresses. Unbonded shells cracked soon after removal from the melt. The 3% cast irons behaved similarly except that they invariably solidified white. The composition did not encourage graphite formation and was not innoculated.

7.3.4.2 Eutectic Tin Lead

Hunt and Jackson[63] say that at normal growth rates of tin-lead eutectic structure, there will be no primary tin dendrites, even if the tin composition drifted a few per cent from the exact eutectic composition. They present an equation, obtained from Hunt and Chilton graphically comparing growth rate to undercooling.

The growth rate of the eutectic solidifying on a lead insert, given by the slope of the theoretical prediction (zero superheat, $H_I = 1500$), is .51 mm/s initially and .26 mm/s after 10s. These growth rates imply an undercooling of about 3° and 2° respectively ahead of the interface.

The metal that had solidified was always smooth, with the exception of an occasional 'pimple', however if vigorous stirring was ommitted the surface deteriorated and became completely uneven apparently with tin dendrites

growing ahead of the interface. The large density difference between the two components meant that the bottom became lead rich at the expense of the bulk of the material.

7.4 The Structure of the Bonds

7.4.1 Ferrous

The preparation of the electron probe analysis results in the absence of prepared standards, assumed the count rates to be proportional to concentration. This ignores interactions such as absorption and secondary emission, which probably produced the high counts at low concentrations and caused the apparent 'false' zeros. No correction was made for counter dead time. It was possible to detect carbon but the results were of no value as the accuracy was of the same order as the detection level.

The small areas that bonded during double sided ingot cladding consistently showed an interface about 30 μm wide. Bonded stainless steel, previously nickel plated, hardly diffused into the base steel at all. The nickel plating was about 250 μm thick, but it was not detected by the electron probe. The sudden influx of metal into the mould appears to have dispersed the nickel layer, but its effect was still strong in inhibiting diffusion.

Bastiens[54] results, after roll bonding nickel plated stainless, illustrate the presence of the nickel layer originally only 16 μm wide, Fig. (59). Preheating for long periods prior to rolling overcame the inhibiting effect by allowing nickel to diffuse into the base steel.

The structures of stainless steel bonded to cast iron exhibited several zones caused by the interdiffusion of chromium, nickel and carbon. In figures 33 and 52 zone 'S' is the cast iron. Zone 'T', with a lower carbon but increased chromium and nickel content, is the matrix surrounding the needle like 'dendrites' (Table 7).

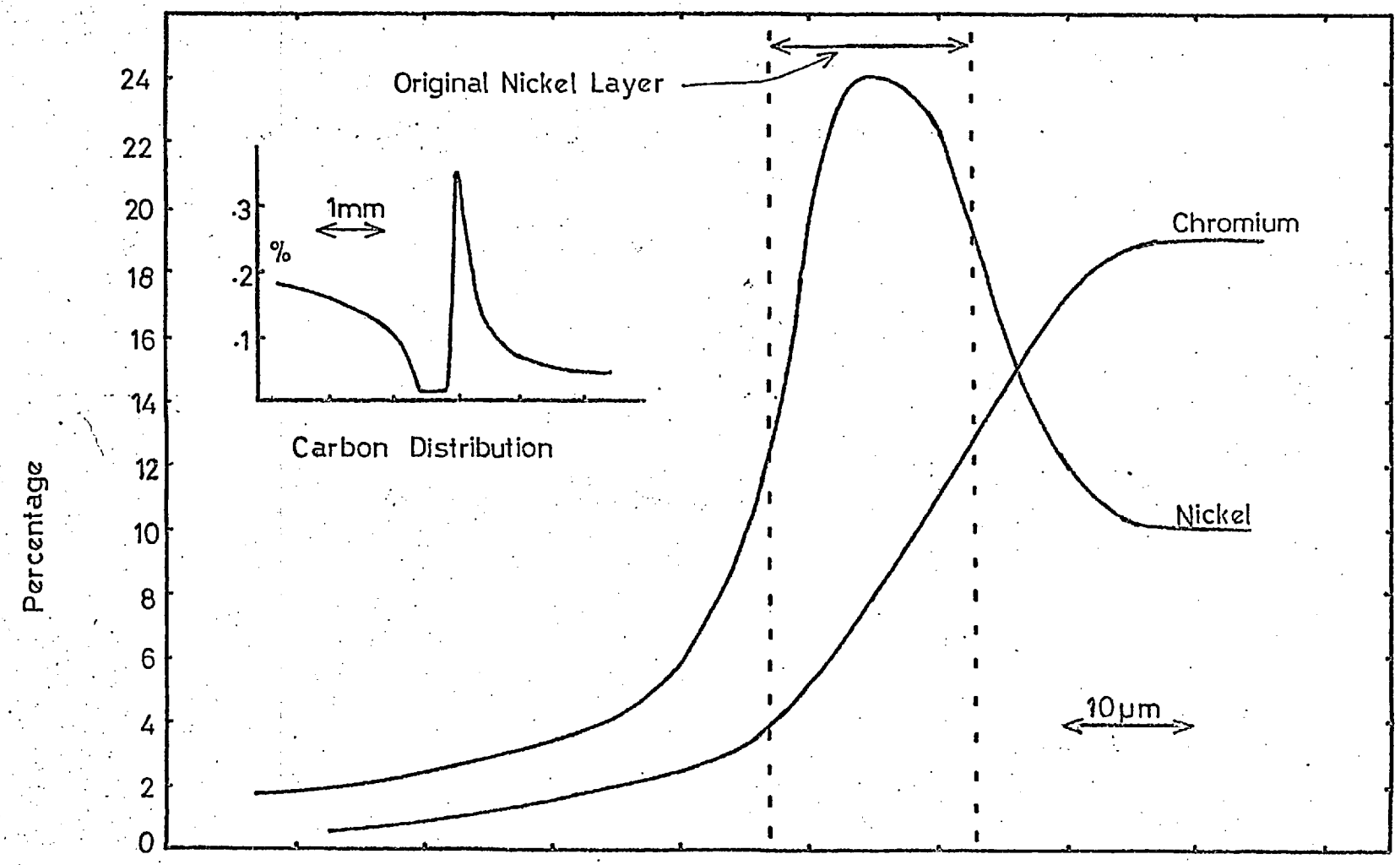


Fig. 59

Chromium and Nickel Diffusion. Ni plated stainless, roll bonded. after Bastien.

The far boundary of the adjacent zone 'U' is probably the original cast iron-stainless steel boundary, and zone 'V' is probably the limit of carbon diffusion into the stainless steel. 'W' is the disturbed zone and 'X' the homogeneous stainless steel.

The diffusion of carbon into the stainless steel had a profound effect upon the appearance of the interface. With cast iron the graphite flakes gradually disappear as the stainless steel is approached. With steel the higher temperatures caused deeper carbon penetration, and the consequent precipitation of carbides at grain boundaries is clearly visible (zone 'Y', Fig. 54). This visual inspection suggests the carbon diffusion created a disturbed layer of about 1.2 mm (this compares to .28 mm for chromium and nickel).

The formation of the boundary was by diffusion of chromium and nickel from the stainless steel and by counter diffusion of iron, carbon and to some extent silicon from the cast iron. The strong dependence of the carbon diffusion coefficient upon solute atom concentration will have caused a reversion in carbon concentration at the boundary of the stainless steel similar to that reported by Bastien.

At about 1000°C the stainless precipitates carbides above .2% carbon and soluble graphite is stable in austenite below 1.8%+ carbon. So the structure changes from austenite, to austenite plus carbides, then to austenite, and then to austenite plus graphite as one moves across the interface into the cast iron. The carbon diffusion is very rapid (Bastien's carbon disturbance region was about 6 mm wide), accordingly these four regions spread over a large area. Cooling this duplex structure from 1000°C transformed the cast iron austenite to pearlite, encouraged more carbide precipitation in the stainless, and transformed some of the lower alloy stainless to a ferritic or even martensitic structure. Bastien presents a diagram which shows that at .1% carbon the structure will change from austenite to martensite, and then to ferrite plus pearlite, as the alloy content decreases.

+ carbon equivalent.

7.4.2 Tin - Lead

The interface is only 8 μm wide, as little solid state diffusion had occurred because of the comparitively low temperatures. Calculations by Lommel and Chalmers[49] suggest tin will diffuse into lead to a depth of 3.10^{-10} m.

The interlamellar spacing of the tin-lead eutectic cannot be judged from fig. (46) as the trace was at right angles to the interface, and parallel to growth direction . The sum of the tin and lead concentrations is one hundred to within ten weight per cent. The uneven trace of the pure lead is topographical in origin, as polishing was again a problem.

7.5 Accuracy of Comparison between Theory and Experiment

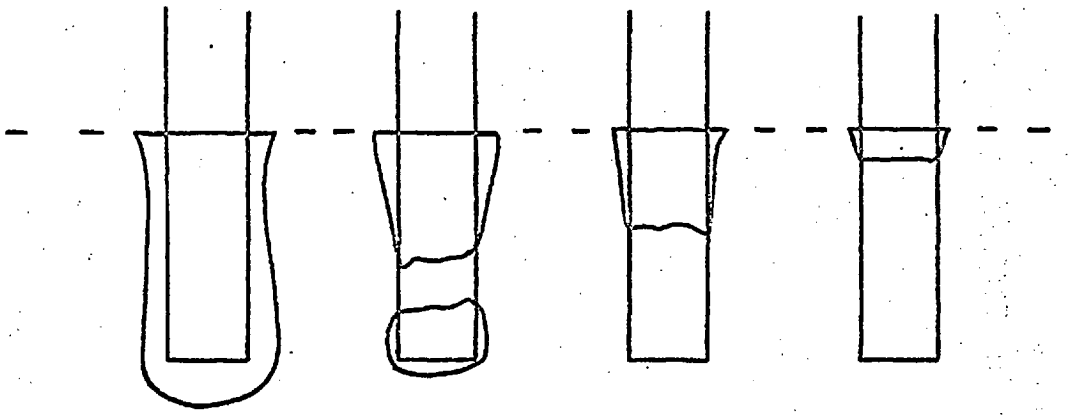
7.5.1 Ferrous Heat Losses

7.5.1.1 Conduction in Stainless Probe

A considerable amount of heat was conducted longitudinally along the cylinder to the portion not immersed, and to the heavy plug screwed in the lower end. The heat sink of this plug outweighed the ample heat supply, causing the end to be a cold region. During the melt back the area just above the plug (No. 2, fig. (60)) was the first to clear, followed by that of the plug itself, and finally all was clear except a small ring at the liquid surface. This (No. 4, fig. (60)) was the criterion normally required experimentally for complete melt back. The low thermal diffusivity of austenitic stainless steel (the theoretical heat front takes 2.18s to travel 12.7 mm) and its high specific heat meant that the affect of the heat sinks are slow but strong, almost unnoticeable during short experiments, nearly dominant during long immersions.

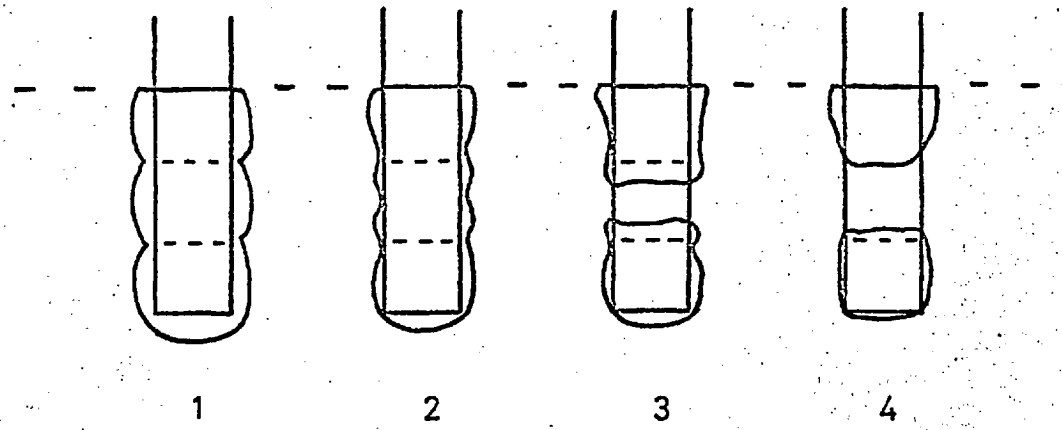
7.5.1.2 From Melting Furnace.

16 kW were needed to hold a steady temperature to make



Cast Iron on Stainless Probes.

Not to Scale.



Sn-Pb Eutectic on Lead Inserts.

Diagrams showing the Progress of Melt Back.

Fig. 60

up for conduction losses into the cooling water through the lining, and radiation from the top surface into the surrounding atmosphere. This radiation caused a cold layer to exist on the surface of the liquid, which could only be completely destroyed by vigorous stirring. With no stirring a dip thermocouple just below the surface indicated a temperature 50°C or more below that of the bulk liquid. 50 mm beneath the surface gave a representative reading at any position. Zero superheat experiments started a fraction above the expected solidification temperature to ensure no solid metal was present in the melt. This additional heat (less than .5% or 17 kJ) was probably less than that due to inhomogenity in liquid temperature after stirring. The effect of lost heat is to increase the amount of solid metal formed.

In melt back experiments 30 kW was selected before the probe was immersed, which was 14 kW in excess of that required to hold temperature. At the start of the experiment the liquid level rose and increased the effective surface seen by the high frequency coil. This in turn changed the transfer of energy; the indicated kilowatts increased but the phase angle moved to about 12° lag., the real power imput was then probably about 29 kW.

None of this heat was dissipated directly in the stainless probe, it all being concentrated in the surface of the liquid close to the coil. The effect of additional heat is very large. 3.0 MJ is stored in the liquid metal at 90° superheat; the energy required to heat the stainless probe to 1135°C is 1.6 MJ; the energy input from furnace power is 45s as .6 MJ.

The biggest factor in favour of small heat losses is the short duration of the experiments, as all heat losses depend upon time. During bonding experiments the effect of the heat dissipation becomes increasingly important.

7.5.2 Lead Heat Losses

7.5.2.1 Conduction in Probe

The stainless cage supporting the lead insert did not dramatically upset the heat flow. The heat needed by the cage was 5 times greater than that needed by the lead it replaced, but it was still less than 4% of the total heat capacity of the insert. The effect of the junction between the lead and the surrounding probe was much more significant, the heat capacity of the joint itself was lower than the material on either side. Fig. (60) illustrates the typical shape of an initial chill layer with the surface depressions over the joints. In addition the insert was too small to be unaffected by vertical heat flow. The good contact with the machined lead insert surface and the stainless probe allowed heat to be conducted from the insert. This loss caused the two edges of the insert to be the last parts to clear during melt back.

7.5.2.2 From Melting Furnace.

Exploratory experiments showed that surface heat losses caused a similar cold layer to exist. It began to grow within 15s of the halt of stirring but was never greater than 2° and did not extend more than 4 cm below the surface. (This was measured with a thermocouple tip bent at right angles so that it lay on isothermals and minimised conduction from the tip).

The zero superheat experiments purposely started at 184°, to prevent any solid forming, adding only 4.9 KJ to the total heat before the experiment.

7.5.3 The accuracy of the theory

The error between successive integrations at half step length is preset before the computation, and as the entire method relies on an original heat balance applied to each section in turn the largest uncertainty is in the

physical data. The zero superheat calculations reflect this in the heat balance calculated at different times during the chill layer growth. At all times the difference between the heat given out by the solidified metal and that absorbed by the wall is less than .01%. The heat balance of course relies upon the temperature profile as estimated by the quadratic function. The final temperatures with tin-lead, after prolonged exposure, were just .07% above that expected (183°C) which is a direct effect of the small heat balance error.

During theoretical melt back the heat balance is not as good; there were intervals early in the computation when the error was as much as 15% but this dropped below 2% by the time melt back was complete. The theory predicts the occurance of melt back under ideal conditions without any heat loss. The nearest approach to this ideality were the conditions that caused the first region of each probe to clear. In practice the small clear patches grew until they joined and a complete ring had cleared. The time that this occurred is the best comparisons between predicted and actual melt back.

The use of effective densities for the calculation ensures that the ultimate heat balance is correct and consequently that the ultimate chill layer thickness is correct. It cannot compensate for the radial heat flow at every stage of the solidification.

The accuracy of the determination of liquid heat transfer coefficients is not very high. For the tin-lead system $\pm$ 10% is reasonable but results for eutectic cast iron may have up to twice this level of error. The difference is basically due to the uncertainty of precise values in the cast iron data and the inherent experimental errors.

7.6 Errors of Measurement

7.6.1 Temperature

The inherent difficulty in measuring surface temperatures was minimised with the spot-welded thermo-

couples, the conduction along component wires, or convection into the air stream were small compared to the direct conduction through the weld. Radiation losses obviously became more important at higher temperatures, particularly when the bead 'saw' the cooler inner stainless tube. The contact of thermocouples with lead was less positive, conduction losses caused them to read low at moderately low temperatures. There were no convection losses at the tips as they were covered by 'araldite'. Both forms of thermocouples gave measurements which fell below those predicted when they approached the limiting values.

The outer surface thermocouple, despite being recessed in the lead insert and covered, locally formed a part of the interface, and distorted isothermals. It appeared to measure a temperature between that of the two surfaces. The slip rings, which conducted the e.m.f. from the inside wall thermocouples, gave no error when rotating cold. Over eutectic at about 200° the thermocouples junctions warmed slightly after about 30 minutes introducing a small error, less than 1°. Over irons at about 1500°C the junctions warmed faster, introducing an error of 12° in 60s, an error less than that inherent in the thermocouples, (1%).

7.6.2 Rotation Speed

The speed of the rotating probe dropped slightly with the additional drag at the start of the experiment. An immediate correction to the voltage of the drive motor brought the timing marks back into line with the stroboscope flashes. Occasionally this resulted in a slight drop in speed for an insignificant period.

7.6.3. Thickness

Each individual micrometer measurement was in error

by less than .03 mm, this is reduced to negligible proportions by averaging. The error produced by reading the graphs is much greater. The overall experimental error was more important. The lowest mean standard deviation based on the limiting thickness value was, for tin-lead, .24mm. For cast iron this standard deviation was .75 mm with rotation based on 8 mm limiting thickness, and .70 mm without rotation based on 4 mm. This large deviation was probably caused by uneven heat transfer conditions, except in the case of rotation when any slight eccentricity could cause a large deviation.

7.6.4 T i m e

The static exposure time, measured by stop watch, had an uncertainty of .2s, always less than 2% of the total exposure time. The error in estimating position, about 5 mm, introduced a .1s uncertainty, so in total an estimated error of .22s is expected in exposure time. The difficulty in measuring melt-back time is mostly a matter of judgement. The only way available of assessing melt back is from several experiments, after removing the probe from the liquid. Before proceeding with bonding experiments the criterion was complete melt back (as No. 4, fig. (60), that is the active section of the probe completely clear of solid metal. The real exposure time is given by the sum of the static time and the two way travelling times. Bonding experiments followed after only one travelling time and so melt back occurs fractionally later than expected from static time measurements. On average this difference was 1.1s for lead and 2.5s for irons, but as an interval for dissolution followed it was relatively insignificant.

In general all these errors, except those attributed to thermocouples, are much smaller than the experimental variations found during the experiments.

8. CONCLUSIONS

It is possible to bond dissimilar metals by allowing surface dissolution under controlled conditions, prior to solidifying the metal.

If dissolution becomes melting, because of increased liquid temperature, the experimental control needs to be more precise.

The theory satisfactorily described solidification of a unique melting point alloy, in imperfect contact with a finite mould wall, of different physical properties.

The theory did not exactly describe solidification with superheat largely because of the assumption of a uniform bulk liquid temperature.

For heat transfer with liquid metal thermal bulk mixing is not assured, despite turbulent fluid flow.

Concentric rotating cylinders with a fluid in the annular space, are very useful systems for investigating heat and particularly mass transfer mechanisms.

- - - - - - -

9. FUTURE WORK

Theoretically it is possible to increase the superheat of the liquid so that no chill layer is formed (presolidification) upon exposure to a cold surface. If enough heat can be removed from the remote surface excessive melting before solidification could be prevented. By this method it may be possible experimentally to avoid catastrophic melting encountered during the exposure of stainless steel to molten carbon (or other) steel, (Appendix 5). Alternatively, the maximum melt substrate melting point difference could be determined by a series of experiments. Each successive experiment would progress further up the iron carbon, or even lead tin, liquidus slope.

An investigation of different systems would determine the compatability of metals of widely differing melting points, such as steel and lead, which could be bonded.

The theory can be applied directly to the solidification of thin wide slabs, in ingot moulds but it would be more immediately acceptable if a satisfactory description of freezing range could be added to the theory.

It is possible to rewrite the theory in terms of cylindrical co-ordinates, or even spherical co-ordinates to describe specialised multi directional phase changes.

There are several developments of this work with industrial applications. With casting inserts, a knowledge of heat transfer coefficients would help prediction of conditions for satisfactory bonding. Hot dip processes, in particular sheet or coils, would benefit in a similar way. A modified casting process could produce double sided clad ingots. The success of this will depend upon the yield which will almost certainly depend directly upon the scale of operation.

A modification to the theoretical model by introducing a separate layer, just ahead of the solidifying interface may improve agreement with experiments. The choice of the layer thickness will probably be very important if a better model for liquid metal heat flow is to be realised.

The theory can also be applied to non metallics such as plastics as well as metals.

- - - - - -

APPENDIX (1)

An attempt at measuring heat transfer coefficients directly.

1) Interface heat transfer coefficient

The heat flux within a chill layer in contact with a lead insert was estimated from temperature gradients under steady state. The chill layer of tin lead eutectic was solidified onto the insert which had two thermocouples set in the wall. Another thermocouple was fixed within the chill layer, and the whole probe assembly was immersed rotating into boiling water. Air cooling removed heat internally.

Equations describing the cylindrical steady state heat flux were used to calculate the interface heat transfer coefficient.

Despite averageing readings, taking care to reach steady state, and taking care to avoid cold junction errors from the condensation of steam, the results had a very wide scatter. The reason being inherent difficulties in measuring small temperature differences. Even using calibrated thermocouples and a high heat flux the accuracy of the method is limited.

2) Liquid Heat Transfer Coefficient

A lead insert, without any chill metal, was immersed rotating in liquid tin lead. The outer furnace heater was set to 183^{o}, to reduce heat losses, and the inner heater set to deliver about 1 kW. Air cooling removed heat from the remote surface whose temperature was monitored with the liquid temperature.

Air cooling at $1.4.10^{-2} m^3/s$ produced in steady state -

$$\Theta_L = 197°C \quad \Theta_R = 175°C \quad \text{at } 200 rpm$$

The heat removed by the air was calculated from data in McAdams giving $H_R = 190$ $W/m^2\ °C$.

Now ignoring cylindrical heat flow

$$Q = H_L(\Theta_L - \Theta_W) = \frac{k}{R}(\Theta_W - \Theta_R) = H_R(\Theta_R - \text{Room Temp})$$

thus $Q = 190\ (175 - 20) = 2.95.10^4\ W/m^2$
which compares to a heat supply of $3.2.10^4\ W/m^2$.
(8.5% error). Hence $H_L = 2900\ W/m^2\ °C$, which compares favourably with the liquid heat transfer coefficients estimated earlier.

Considering that the overall heat flow is the sum of unequal parts in both lead and the surrounding stainless cylinder the result is only an estimate.

This approach is much more promising as a technique for measuring a heat transfer coefficient.

- - - -

APPENDIX (2)

The effect of air cooling in the stainless steel probe.

Fig.(61) shows a portion of the probe divided into two control volumes containing gas at temperatures θ_1, θ_2 respectively and flow rate $\dot{G}$.

There is no accumulation in either volume, and if gas temperatures are uniform in each control volume

$$\dot{q}_2 + \dot{G}c(\theta_2 - \delta\theta_2) = \dot{q}_1 + \dot{G}c\theta_2$$

$$\dot{q}_1 + \dot{G}c\,\theta_1 = \dot{G}c(\theta_1 + \delta\theta_1)$$

$$\dot{q}_2 = \frac{\theta_0 - \theta_2}{\sigma_1 + \sigma_2}, \quad \dot{q}_1 = \frac{\theta_2 - \theta_1}{\sigma_3 + \sigma_4} \qquad \ldots\ldots (39)$$

where σ is the thermal resistance in the outer wall, and the three surfaces, respectively.
thus -

$$\frac{d\theta_2}{dx} = \frac{1}{\dot{G}c}\left\{\frac{\theta_2 - \theta_1}{\sigma_3 + \sigma_4} - \frac{\theta_0 - \theta_2}{\sigma_1 + \sigma_2}\right\}$$

$$\frac{d\theta_1}{dx} = \frac{1}{\dot{G}c}\left\{\frac{\theta_2 - \theta_1}{\sigma_3 + \sigma_4}\right\} \qquad \ldots\ldots (40)$$

these lead to the following equations expressed as dimensionless temperatures.

$$\frac{d^2\theta_2^*}{dx^2} + A\frac{d\theta_2^*}{dx^2} - AB\theta_2^* = 0$$

$$\frac{d^2\theta_1^*}{dx^2} + A\frac{d\theta_1}{dx} - AB\theta_1 = 0$$

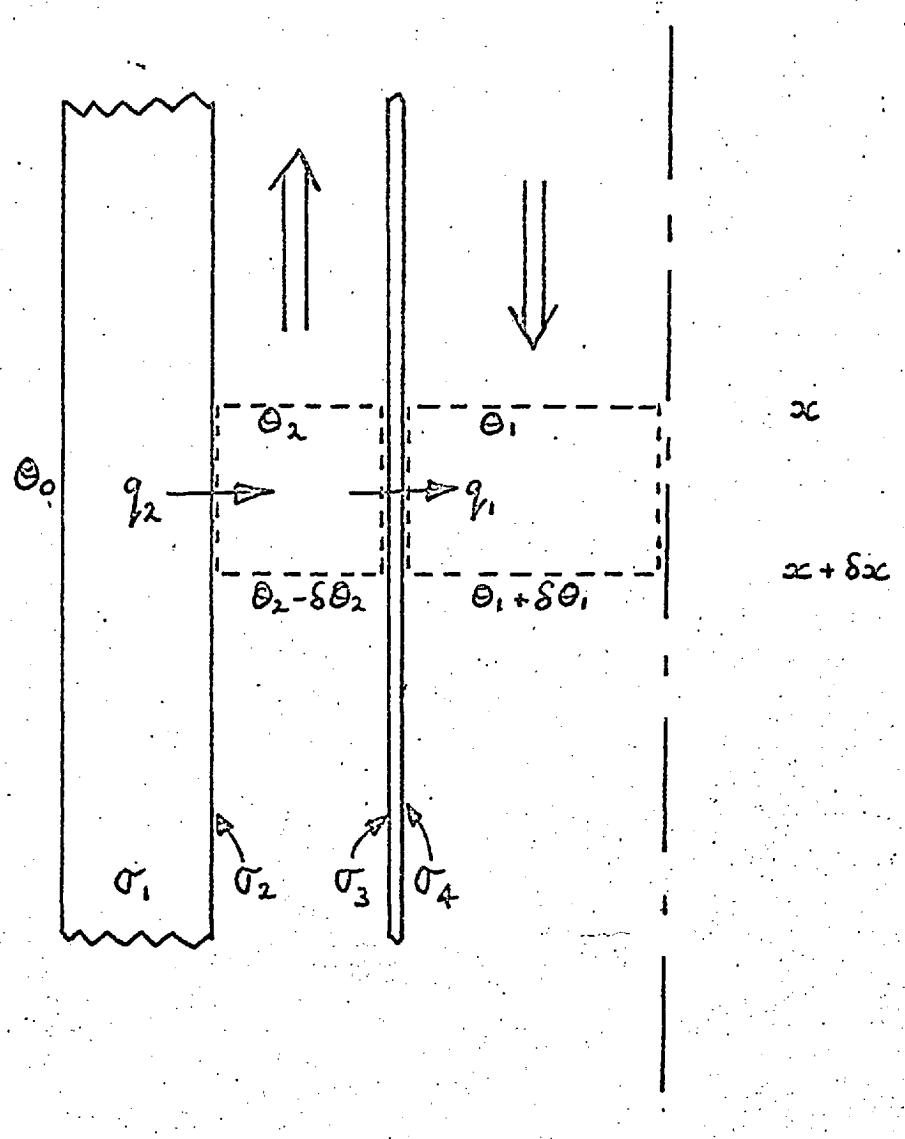
where

$$\theta^* = \frac{\theta_0 - \theta}{\theta_0 - [\theta_1]_0}, \quad A = \frac{1}{\dot{G}c(\sigma_1 + \sigma_2)}, \quad B = \frac{1}{\dot{G}c(\sigma_3 + \sigma_4)}$$

the solutions are of the form -

$$\theta_1 = K_1 e^{\lambda_1 x} + K_2 e^{\lambda_2 x}$$

$$\lambda_1, \lambda_2 = -\frac{A \pm \sqrt{A^2 + 4AB}}{2} \qquad \ldots\ldots (41)$$



Air Cooling inside Probe,

divided into two control volumes

Fig. 61

The heat transfer coefficients required for this calculation were found using empirical data from McAdams.

These are for common gases for turbulent flow inside tubes with natural convection being unimportant.

$$h = \cdot 01444 \frac{C (\dot{G})^{\cdot 8}}{D^{\cdot 2}}$$

and for flow in an annulus.

$$\frac{h}{C\dot{G}} \left(\frac{C D \rho}{k}\right)^{2/3} \left(\frac{\nu \rho_w}{\nu \rho_b}\right)^{\cdot 14} = \frac{\cdot 023}{\left(\frac{D G}{\nu \rho_b}\right)^{\cdot 2}}$$

N.B $\left(\frac{\nu \rho_w}{\nu \rho_b}\right)^{\cdot 14} \simeq 1$

and the convection for a short length of pipe where

$$\frac{L}{D} < 60 \quad \text{is} \quad h = h' \left\{1 + \left(\frac{D}{L}\right)^{\cdot 7}\right\}$$

These equations allowed the optimum dimensions for the probe assembly to be determined. The computerized calculations indicated that an air flow rate of would remove about 1.5 kW. with outlet temperature of 150°C, and an inside wall temperature of about 800°C when the probe is immersed in metal at 1400°C.

- - - -

APPENDIX (3)

Correction for Probe Residence time with liquid metal displacement.

Now the velocity of probe is 34.5 mm/s (measured) and if the probe depth is x

it displaces $\pi R_1^2 x$

$\therefore$ liquid level rises $\frac{\pi R_1^2}{\pi R_2^2} x$

i.e. increase in depth is $\frac{R_1^2}{R_2^2} x$

thus the relative velocity of probe to liquid surface is

$$\left[\frac{R_1^2}{R_2^2} + 1\right] 34{\cdot}5 \quad mm/s$$

if depth of dip is x at any instant and the time to reach this is τ

$$\tau = \frac{x}{\left[\frac{R_1^2}{R_2^2} + 1\right] 34{\cdot}5} \text{ s.} \qquad \ldots\ldots (42)$$

and if ϕ is the time the probe is stationary a position x from the bottom of the probe has been exposed for

$$\phi + 2\tau \text{ s.}$$

This enabled a graph to be prepared estimating the time to be added to the static exposure time for different depths.

APPENDIX (4)

ANALYSIS OF MATERIALS AND SPECIFICATION OF MATERIALS USED

			%
L E A D	Commercial Purity.	Pb	99.97
		Bi	.02
		Sb	.01
S T A I N L E S S S T E E L		C	.07
		Si	.50
		Mn	.90
		Cr	17.
		Ni	8.5
T I N	Commercial Purity	Sn	99.85
		Pb	.03
		Cu	.03
		As	.03
		Fe	.01
		Sb	.01
I R O N	Melting stock	C	.076
		Si	.01
		S	.04
		P	.026
		Mn	.36
		Al	.001
		Ti	.01
		V	.01
		O	.012
		N	.003
C A S T I R O N.	Melting Stock	C	4.3
		Si	1.1
		Mn	1.11
		P	.019
		S	.15

APPENDIX (5)

Prevention of Catastrophic Melting During Melt Back.

If cooling of the remote mould wall surface is to eliminate melting of the mould when exposed to liquid with a high degree of superheat, the heat removed from the exposed surface must exceed that supplied from the liquid -

$$\text{i.e.} \quad -k\left(\frac{\partial\theta}{\partial x}\right)_o \geqslant h_L\left(\theta_L - \theta_M\right) \qquad \ldots\ldots (43)$$

where θm is the melting point of the mould material.

Assuming steady state heat conduction -

$$\dot{q}''_R = h_R\,\theta_R = \frac{k_w}{R}\left(\theta_m - \theta_R\right) = -k_w\left(\frac{\partial\theta}{\partial x}\right)_o \qquad \ldots\ldots (44)$$

This is certainly not the case for a cold mould suddenly exposed but it is a fair approximation for a hot mould wall with continuous remote surface cooling.

From equation (44) $\quad \theta_R = \dfrac{k_w\,\theta_m}{R\,h_R + k_w}$

hence the inequality becomes -

$$h_R\left(\frac{k_w\,\theta_m}{R\,h_R + k_w}\right) \geqslant h_L\left(\theta_L - \theta_m\right) \qquad \ldots\ldots (45)$$

Calculations from the condition for presolidification using $H = 2500$, $H = 8000$ W/m^{2o}C, the most probable values determined earlier, for mild steel ($\theta_S = 1500^{\circ}$C) show that a liquid temperature in excess of 1962°C will not solidify. Similarly for 1.4% steel ($\theta_S = 1420^{\circ}$) the corresponding liquid temperature is 1850°C.

Now for stainless steel (θ_m = 1420) exposed to

Heat removed from mould wall under steady rate	Heat supplied to mould from liquid
	mild steel
$1.36.10^5$ W/m^{2}s (h_R = 100 W/m^2 °C)	$4.64.10^6$ W/m^{2}s (θ_L = 2000°C)
	1.4% steel
$2.1.10^6$ W/m^{2}s) (h_R = 4000 W/m^2 °C)	$1.84.10^6$ W/m^{2}s (θ_L = 1850°C)

That is air cooling ($h_R \sim$ 100 W/m^2 °C) is totally insufficient but liquid metal cooling may just be enough to prevent melting of stainless in contact with liquid steel at 1850°C. under transient rather than steady state conditions

APPENDIX (6)

Lead Polishing.

A most important part of Clarke's[60] work was developing the polishing technique detailed here :-

Initial surface preparation by rubbing on a file held in a vice.

Silicon carbide papers embedded particles in the lead, this was minimised by using 0,00,000 alumina papers.

Strips of this paper 110 mm x 270 mm were rubbed with perspex to fill in the spaces, and a thick layer of thinned paraffin wax covered the particles.

Specimen were polished with a warm concentrated solution of paraffin wax in paraffin poured on for additional lubrication.

Approximately two samples could be polished on each strip before it became plugged with lead and required complete cleaning with paraffin. The use of 0000 paper only embedded more particles.

The best polish was given by a Syntron vibratory polishing machine using a selvyt polishing cloth and a slurry of .1 μ alumina in foaming shaving cream and distilled water. Up to one hour was needed with a clean cloth but longer was needed with a clogged cloth for acceptable results. There was some water staining.

A reasonable result could be obtained with a manual polish. Two fully napped cloths impregnated with 4 - 8 μ and 0 - 1 μ diamond paste respectively, were used with paraffin as lubricant. Some diamond particles became embedded and some rounding occurred.

- - - - -

APPENDIX (7)

An Empirical Estimation of Nusselt Numbers.

The calculations of Sparrow Munroe & Jackson show that for inner cylinder only rotating ($\mu = 0$) the critical Taylor number (Ta^*) for $\eta = .35$, the geometry used here is $9.4.10^4$. Below this value laminar flow exists but above it Taylor vortices impose themselves upon the flow. The value $Ta^* = 9.4.10^4$ is equivalent to .0234 rad/s for lead, and .0534 rad/s for iron.

The values of the Taylor numbers of the experimental conditions used here are :-

		68 r.p.m.	200 r.p.m.
Ta^*	Lead	$8.76.10^9$	$7.18.10^{10}$
	Iron	$1.68.10^9$	$1.37.10^{10}$
Ta	Lead	$4.06.10^5$	$11.95.10^5$
	Iron	$1.78.10^5$	$5.22.10^5$

These are all so high that they suggest turbulent flow. Kay and Elgar's paper suggests, by extrapolating the results above their experimental range, fig. (62), that above Ta 1000, with no axial flow, the fluid movement is turbulent flow plus vortices. The equivalent Ta values for the present case are well above this second transition. For the purpose of the subsequent discussion the fluid flow is assumed to be completely turbulent. A similar argument with an identical conclusion was followed by Sherwood and Ryan (44).

The geometry of the lead-tin and ferrous systems is similar enough to use just one equation to describe the number. For the inner wall of an annulus with axial, turbulent, liquid metal flow and constant heat flux, it is, as given by Dwyer (53),

$$Nu = 6.78 + .0222 (\overline{\Psi}\ Pe)^{.8} \qquad \text{eqn. (46)}$$

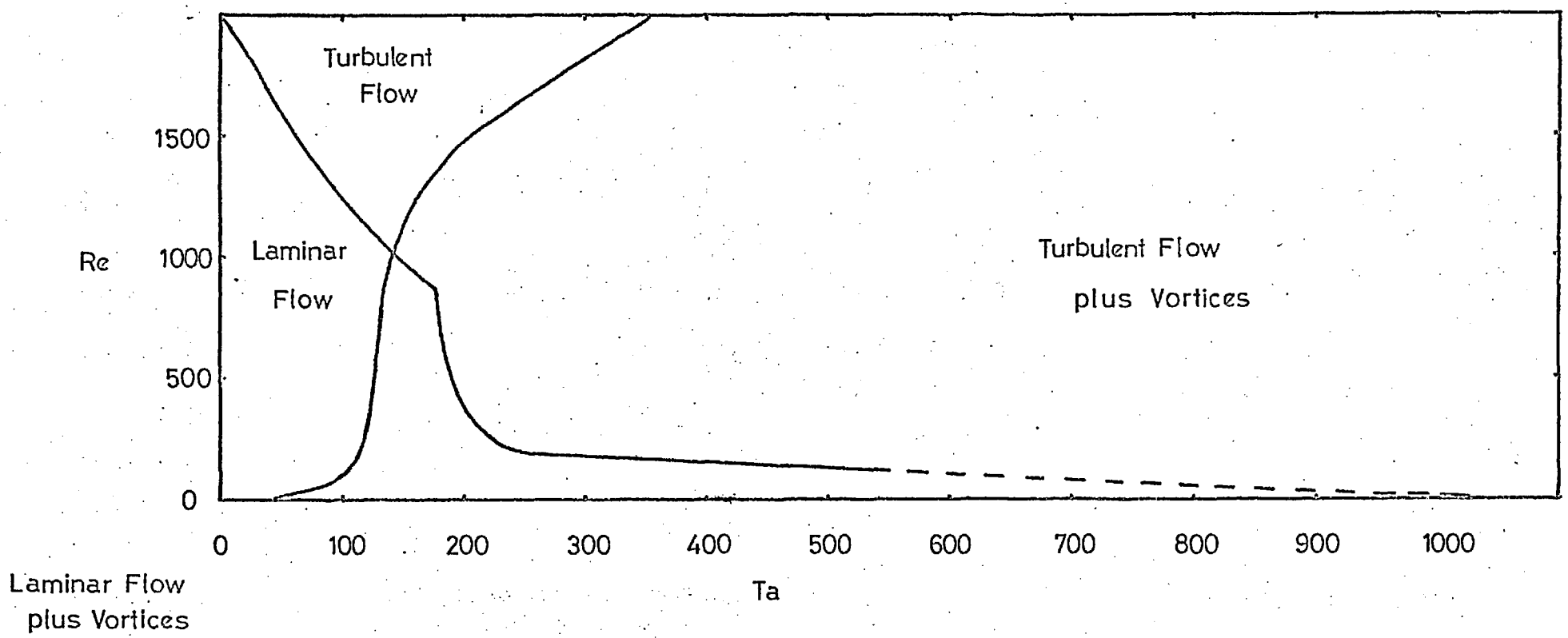


Fig. 62

Four Modes of Fluid Flow for a Rotating Cylinder with Cross Flow.

from Kay and Elgar [29]

His value for molecular conduction only is Nu = 6.85. (For the present geometry). The difference between this and the constant term in eqn. (46) is only 1% and so it is fair to say the equation approximately describes the Nusselt number for all values of $(\overline{\Psi}\ Pe)$.

An expression for heat transfer to an inner rotating cylinder is similar. The limiting value for pure conduction will be the same, the exponent of the Reynolds number will be .7 as for the rotating cylinder heat, mass, and friction data. The values for the other constants β, γ are more difficult to determine; if we assume Dwyers and Tu's equation for estimating Ψ are valid for rotating cylinders we obtain $\overline{\Psi} = 1.0$ for all the experimental conditions $(3.5.10^3 < Pe < 7.2.10^4)$. In the absence of other data we assume $\beta = .022$ (the values in McAdams (51) are .0175, .020) which is the value for axial flow in annuli. Thus after converting for a change in characteristic length to the inner cylinder diameter, we obtain

$$Nu = 3.70 + .0183\ (Pe)^{.7} \qquad \ldots\ldots (47)$$

For the experimental conditions used here this gives :-

		Pe	Nu	H_L (W/m^2 ^oC)
Lead	67 r.p.m.	$1.75.10^3$	7.3	3340
	200 r.p.m.	$1.22.10^4$	14.1	6420
Iron		0.0	3.70	730
	200 r.p.m.	$3.60.10^4$	32.6	6430

APPENDIX (8)

Data used in Computation.

Eutectic tin-lead data.

H	37,000	J/kg	Liquid Properties.
θ_s	183	°C	
C_L	217.9	J/kg°C	
k_L	28.57	W/m°C	
p_L	8010	kg/m^3	
M	21.9	kg	
A	.029	m^3	Solid Properties.
C_s	216.9	J/kg°C	
k_s	51.4	W/m°C	
p_s	8300	kg/m^3	
Lead			
Cw	136.1	J/kg°C	Mould Wall Properties.
kw	31.0	W/m°C	
pw	11,150	kg/m^3	
Stainless			
Cw	523	J/kg°C	Mould Wall Properties.
kw	17.28	W/m°C	
pw	7900	kg/m^3	

Most of this data is as collected by Malhotra [5] but that for stainless is by interpolation from (20)

Eutectic Cast Iron

Uncertainty surrounds much of the data but the best estimates available have been used.

Cast Iron			
H	272,000	J/kg	Liquid Properties.
θ_s	1135	°C	
C_L	775	J/kg°C	
k_L	12.5	W/m°C	
p_L	6900	kg/m^3	
M	44	kg	
A	.030	m^3	Solid Properties.
C_s	636	J/kg°C	
k_s	37.7	W/m°C	
p_s	6800	kg/m^3	
Stainless Steel			
Cw	600	J/kg°C	Mould Wall Properties.
kw	30	W/m°C	
pw	7700	kg/m^3	

Values used are selected or estimated for 1135°C.

- - - - - - -

N O M E N C L A T U R E

Variable	Description	Dimensions	Dimensionless Equivalent
b	gap between rotating cylinders	m	-
c	specific heat	$J/kg\,°C$	$c^* = c/c_s$
f'_z	see equation 6	-	-
f'_θ	See equation 6	-	-
h	heat transfer coefficient	$W/m^2\,°C$	$h^* = \frac{h}{h_I} = \frac{-h\theta_s}{[\dot{q}''_o]_o}$
k	thermal conductivity	$W/m\,°C$	$k^* = \frac{k}{k_s}$
$\dot{q}''$	heat flux	$W/m^2\,\Delta$	$q^* = \frac{\dot{q}''}{[\dot{q}''_o]_o}$
$[\dot{q}''_o]_o$	initial heat flux $(= -h_I\theta_s)$	$W/m^2\Delta$	-
t	solidified metal thickness	m	$t^* = \frac{-[\dot{q}''_o]_o\, t}{\theta_s k_s}$
v	velocity	m/Δ	
x	linear distance	m	
A	constant or area	- (m^2)	
B	constant	-	
D	characteristic dimension (diameter)	m	
$\dot{G}$	flow rate	m^3/Δ	
H	latent heat	J/kg	$H^* = \frac{H}{c_s\theta_s}$

Contd./

Variable	Description	Dimensions	Dimensionless Equivalent
K	constant	-	
L	length	m	
m''	mass of liquid per unit surface area	kg/m^2	$m^* = \frac{[\dot{q}''_0]_0 \, m''}{k_s \Theta_s \rho_L}$
Pe	Peclet number	-	
P_r	Prandtl number	-	
Q	heat added by furnace power	W	$Q^* = \frac{Q}{A[\dot{q}''_0]_0}$
R	radius	m	
R	(without subscript) wall thickness	m	$R^* = \frac{-[\dot{q}''_0]_0 R}{k_s \Theta_s}$
Re	Reynolds number	-	
Nu	Nusselt number	-	
Ta	Taylor number	-	$Ta = \frac{R_m^{1/2} L^{3/2} \omega_1}{\nu}$
T^*	modified Taylor number	-	$T^* = \frac{\omega_1^2 R_2^4}{\nu^2}$
Y	$= \Theta_w^{*2}$	-	
α	equation p 26	-	
β	equation p 26	-	
γ	equation p 26	-	
δ	penetration depth	m	$\delta^* = \frac{-[\dot{q}''_0]_0 \delta}{k_s \Theta_s}$
η	ratio R_1/R_2	-	
Θ	temperature	$^\circ C$	$\Theta^* = \Theta/\Theta_s$

Variable	Description	Dimensions	Dimensionless Equivalent
λ	constant	-	
ρ	ratio $\frac{\omega_2}{\omega_1}$	-	
ν	kinematic viscosity	m^2/s	
ξ	dimensionless time	-	
ρ	density	kg/m^3	$\rho^* = \rho/\rho_s$
σ	thermal resistance per unit surface area	$^oC/W$	
τ	time	s	$\xi = \frac{[q''_o]^2_o \tau}{\Theta_s^2 \rho_s c_s k_s}$
ϕ	time	s	
$\overline{\psi}$	constant p26 ratio of thermal eddy diffusivity to momentum eddy diffusivity	-	
ω	angular velocity	rad/s	
Γ	see equation 4	-	
Λ	see equation 5	-	
Υ	ratio $\left(\frac{k_s \rho_s c_s}{k_\omega \rho_\omega c_\omega}\right)$	-	
δ_b	see equation 3	-	
SUBSCRIPTS			
1.	inner		
2.	outer		
b	bulk		

Subscripts	contd./
o	surface of chill layer in contact ith probe wall.
m	mean
s	solidified metal.
τ	interface between solidified and liquid metal.
ω	mould wall
I	metal mould interface
R	remote surface
L	liquid metal
W	surface of wall in contact with chill layer.

LIST OF REFERENCES

1) T. SHEPPARD & M. G. BROOKS.	Metallurgia Oct. '69, p. 145.
2) J. F. HOWALICK & D. R. HAY	Met. Trans. '71, 2 p. 1953
3) G. R. GOWAN, O. R. BERGMANN and A. H. HOLTZMAN.	Met. Trans. '71 2 p. 3145
4) C. M. ADAMS	Liquid Metals and Solidification P. 187, A.S.M. Cleveland '58.
5) S. L. MALHOTRA	Ph.D. Thesis London University '70.
6) S. H. CHO and J. E. SUNDERLAND	Jnl. Heat Transf. Aug. '69, P. 421.
7) A. W. D. HILLS	T.M.S. A.I.M.E. '69 245 p. 1471
8) L. HOGAN	Jnl. Aust. Inst. Met. '61 6 p. 279
9) G. CHADWICK	Progress in Mtl. Sci. '63 12 (2) p. 169.
10) M. A. GLINKOV, Y. F. NICKDEAV and Y. P. FILIMONOV	Izvest Vuz Chem Met. '69 12 (1) p. 164
11) H. R. THRESH, A. F. CRAWLEY and D. W. G. WHITE.	T.M.S. A.I.M.E. '68 242 p. 819.
12) H. R. THRESH and A. F. CRAWLEY	Met. Trans. '70 1 p. 1531
13) K. HAMAGUCHI and G. W. HEALY	T.M.S. A.I.M.E. '66 236 p. 944
14) ANGUS	Cast Iron BCIRA '60
15) M. HILLERT	Recent Research on Cast Iron p.101 Conf. '68
16) R. HULTGREN, R. L. ORR, P. D. ANDERSON & K. K. KELLY	Selected values of Thermodynamic Properties of Metals and Alloys J. Wiley & Son, London '63

contd./

17)	L. S. DARKEN and R. P. SMITH	J. Am.Chem.Soc. '46 68 p. 1172.
18)	ROSSINI	Circular No. 500 '49
19)	R. W. RUDDLE	The Solidification of Castings Inst.Met. London '57.
20)		The Properties of EN. Steels B.I.S.R.A.
21)	V. PASHKIS	Trans. Am. Fndy. Soc. '53 61 p. 142
22)	R. J. SARGANT and M. R. SLACK	J.I.S.I. '54 177 p. 428
23)	F. D. RICHARDSON	Trans. Faraday Soc. '53 49 p. 171
24)	E. A. WELZER	Jnl. of Metals Aug. '67 p.50
25)	D. E. KRAUSE	Foundry May '62 p. 210
26)	D. PONTONE	Fonderie Aug. '67 p. 311
27)	L. A. DORFMAN	Hydrodynamic Resistance and Heat Loss of Rotating Solids. Oliver and Boyd.
28)	G. I. TAYLOR	Phil. Trans. Roy. Soc. A. '23 223 p. 289
29)	J. KAYE and E. C. ELGAR	Trans. A.S.M.E. April '58 80 p. 753
30)	I. S. Bjorklund & W. M. KAYS	Jnl. Ht. Transf. Aug. '59 p.175.
31)	E. M. SPARROW, W. O. MUNROE and V. K. JONSSON	Jnl. Fluid Mech. '64 20 (pt.1) p.35.
32)	D. MESKYN	New Methods in Laminar Boundary Layer Theory. Pergamon London '61.

33)	G. A. ETMUND	Trans. A.S.M.E. '55 77 p.1283
34)	D. DROPKIN & A. CARNI	Trans. A.S.M.E. £57 79 p.741
35)	J. T. ANDERSON and O. A. SAUNDERS	Proc. Rpy. Soc. A. 217 p.555
36)	W. M. KAYS & I. S. BJORKLUND	Trans. A.S.M.E. '58 80 p.70
37)	KING	Jnl. A.M. Chem. Soc. '35 57 p.1212
38)	A. C. MACKRIDES and N. HACKERMAN.	Jnl. Electro.Chem.Soc. '58 105 (3) p.156
39)	A. G. WARD & J. W. TAYLOR	J.I.M. '57, 85 p.35
40)	J. K. JACKSON and R. E. GRACE.	Phys.Chem.Proc.Met. Symp. Pittsburgh, April '59 (pt.1) p.633.
41)	B. ROALD and W. BECK.	Jnl. Electrochem.Soc. '51 98 p.277
42)	M. EISENBERG, C.W. TOBIAS and C. R. WILKE.	Chem.Eng.Prog.Symp. '55 51 (14) p.1
43)	T. THEODORSON & A. REGIER	Natl.Adv.Comm. Aeronaut rep. 793.
44)	T. K. SHERWOOD & J. M. RYAN	Chem.Eng.Sci. '59 11 (2) p.81
45)	T. L. SRI KRISHNA, M. A. DAYONADA and R. E. GRACE.	Met. Trans. '71 2 p.3355
46)	R. G. OLSSEN, V. KOUMP and T. F. PERZAK	T.M.S. A.I.M.F. '66 236 p.426
47)	H. SCHENK, A. GERBER and E. STEINMETZ.	Archiv. Eisenhuttenwesen '67 40 (12) p.850
48)	R. D. PEHLKE, P. D. GOODALL and R. W. DUNLAP.	T.M.S. A.I.M.E. '65 233 14 p.1420
49)	LOMMEL and CHALMERS	T.M.S. A.I.M.E. '59 215 p.499
50)	J. S. COOMBES, W.M. GIBBON and S. O. PROBART.	Chem. & Proc.Eng. March '58 p.96
51)	W. H. McADAMS	Heat Transmission 3rd Ed. McGraw Hill, London p.215

52) O. E. DWYER & P. S. TU	Nuclr. Sci. Eng. '62 15 p.58
53) O. E. DWYER	Nuclr. Sci. Eng. '63 17 p.336
54) P. BASTIEN	Revue de Metallurgie '61 58 p. 1039
55) R. DREWETT	Corrosion Sci. '69 9 p.823
56) D. D. VAN HORN	Trans. A.S.M. '59 51 p.185
57) J. S. KIRKALDY	Can. J. Phys. '58 36 p.917
58) L. S. CASTLEMAN	Nudr. Sci. & Eng. '58 (4) p.209
59) E. BERAHA	Praktishe Metallographic '68 5 (9) P.501
60) I. S. R. CLARKE	Ph.D. Thesis University New South Wales '69.
61) W. H. McADAMS	Heat Transmission 3rd Ed. McGraw Hill, London.
62) W. OLDFIELD	Recent Research on Cast Iron. Conf. '68 P. 281
63) HUNT and JACKSON	T.M.S. A.I.M.E. '66 236 p. 843
64) W. H. McADAMS.	Heat Transmission, 34d Ed. McGraw Hill, London, p.171

A C K N O W L E D G E M E N T S

I wish to acknowledge the help of all the John Percy Group members and staff for their interest, guidance and assistance; in particular, Dr. R. J. Tait and Mr. A. J. Haynes. The continuing encouragement and support of Dr. A. W. D. Hills during his supervision has been invaluable.

A large part of the work was financed by Richard Thomas and Baldwins Limited, to whom thanks are due.

More recently, the encouragement of my wife over a long period, and the typing of Mrs. L. Mason, have been a great help.

- - - - -